Search for Supersymmetric Particles in e^+e^- Annihilation at TRISTAN

トリスタン電子陽電子衝突型加速器による

超対称性粒子の探索

Doctoral thesis

December 1988

Tohru Takahashi

Department of Physics Nagoya University

名古屋大学理学部物理学教室

高橋 徹

報告番号	甲 第 2151 号

主論文

Search for Supersymmetric Particles in e^+e^- Annihilation at TRISTAN

Tohru Takahashi

Department of Physics, Nagoya University, Nagoya, 464

December 1988

Abstract

The results of a search for supersymmetric particles are presented using $11pb^{-1}$ data accumulated by the TOPAZ detector at the TRISTAN e^+e^-collider in the energy range $\sqrt{s} = 52 \sim 57$ GeV. Assuming the photino to be massless, we place limits on the chargino of $m_{\tilde{\chi}} > 25.5$ GeV, on the scalar muon, tau, and quark of $m_{\tilde{\mu}} > 24.5$ GeV, $m_{\tilde{\tau}} > 21.7$ GeV, and $m_{\tilde{q}} > 26.3$ GeV respectively. The scalar electron can be excluded up to a mass of ~ 28 GeV. These mass limits are used to constrain the parameters of the N=1 minimal supergravity models.

Acknowledgement

The author would like to thank to all members of the TOPAZ collaboration for their help and fruitful discussions. Particularly, he is deeply indebted to Dr. R. Itoh, Dr. K. Fujii, and Dr. T. Tsukamoto. If it were not for their help, this work would not be completed. Dr. S. Uno is greatly appreciated for his contribution to constructing the End Cap Calorimeter. He also wish to thank to all members of High Energy Physics Laboratory of Nagoya university for their help and useful discussions. In particular, he thanks to Prof. R. Kajikawa for his continuous help and encouragement.

Table of Contents

1. Introduction

Physics below the energy scale of $\sim$ 100 GeV has been successfully described by the standard model. This model is based on the gauge group $SU(3) \otimes SU(2)_L \otimes U(1)_Y$ where the $SU(3)$ describes strong interaction (QCD)[1] and $SU(2)_L \otimes U(1)_Y$ represents electromagnetic and weak interaction[2] . The discovery of $W^{\pm}$ and Z^0 bosons[3] , which are the carriers of the weak force, provided one of the strongest support to the standard model. Up to now, no evidence is reported inconsistent with the model.

In spite of the apparent success, many physicists do not regard the standard models as the ultimate theory of the elementary particles. It should be an effective theory at energy below $O(100GeV)$, since, first, the model has too many parameters to be input by hand, and second, it does not truly unify the fundamental interactions, i.e, there are three independent coupling constants corresponding to the three groups, $SU(3)$, $SU(2)_L$ and $U(1)_Y$, and the gravity is left ununified. If we believe the unification of the interactions at an energy scale Λ, the Higgs boson mass, as long as it is elementary, gets a radiative correction proportional to Λ. In order to keep the Higgs mass in the same order of the magnitude as the weak mass scale, we have to assume amazingly fine tuning of the parameters. This is known as the naturalness problem.

The supersymmetry (SUSY)[6] , the symmetry between bosons and fermions, resolves this problem, since the supersymmetric partner of a conventional particle contributes to the correction with the opposite sign and therefore cancels out the Λ^2 divergence of the Higgs mass term. The supersymmetry, if it is the realistic solution, must be a broken symmetry since there are no SUSY partners found mass-degenerate with the conventional particles. The SUSY models predict, however, the SUSY partners should have a mass below $O(1\ TeV)$ in order to solve the naturalness problem. These SUSY particles have been searched for extensively both at $p\overline{p}$ and e^+e^-colliders[10] .

This paper reports on the search for supersymmetric particles predicted by the minimal N=1 supergravity models[7,8,9] by the TOPAZ detector operating at the TRISTAN e^+e^- collider. The data used in the analysis were taken from May 1987 to August 1988 in the energy range $\sqrt{s} = 52 \sim 57$ GeV corresponding to the integrated luminosity of $11pb^{-1}$.

The organization of this paper is as follows: in chapter 2, particles predicted by the SUSY is introduced: signature of the SUSY in the e^+e^- collision are discussed in

chapter 3: chapter 4 describes the TRISTAN and the TOPAZ detector: the flow of the raw data reconstruction is described in chapter 5: data are analysed and the results of the SUSY search are presented in chapter 6; we examine the results and derive the constraints on the parameters of the SUSY model in chapter 7: and finally the paper is concluded in the chapter 8.

2. Phenomenology of the SUSY

In recent studies, models based on the global SUSY were found to have difficulty in reproducing low energy phenomenology[8] . In addition, the unification scale of the SUSY GUT is $\sim 10^{16}$ GeV while the Plank mass is $m_{PL} = (8\pi G)^{-1/2} \sim 10^{19}$ GeV where G is Newton's gravitational constant. It is not reasonable to neglect gravity there. Recent SUSY models are based on the local supersymmetry, i.e, supergravity (SUGRA). Our analysis described in this paper is, therefore, based on the minimal N=1 supergravity.

In most SUGRA models, the supersymmetry is broken by a soft supersymmetry breaking term via gravity (soft means soft enough to keep protection effect for the naturalness problem) which trigger the breaking of the $SU(2)_L \otimes U(1)_Y$. This mechanism is an analogy of the Higgs mechanism in the standard model and called superhiggs mechanism where the gravitino (spin 3/2 partner of the graviton) gets a mass combined with the Goldstone fermion (the goldstino). The minimal set of particles required for the model is listed in table.1. In the matter multiplet, the superpartner must be exist for each of the left- and right-handed fermions, because the number of degree of freedom for the fermions and scalars must be equal in each supermultiplet. In the gauge boson sector, there exist superpartners of the gluon, $W^{\pm}$, Z^0, and γ called gluino ($\tilde{g}$), wino ($\tilde{W}^{\pm}$), zino ($\tilde{Z}^0$), and photino ($\tilde{\gamma}$), respectively. Since SUSY does not allow the term with H^* in the Lagrangian in contrast to the standard model , we need at least two Higgs $SU(2)$ doublets to give the masses to both 'up' and 'down' type quarks. Then there exist three neutral and two charged Higgs particles and their superpartners (the higgsinos) in the minimal (two higgs doublet) model after the weak gauge bosons become massive.

When the SUSY is broken, the masses of the conventional particles and their superpartner split and the mixing between superpartners occurs which are shown in table. 1 as the mass eigen states. After the mixing the left and the right handed scalar fermions are mixed and form mass eigen states. The gauginos and the higgsinos are also mixed and their mass eigen states are charginos and neutralinos for charged and neutral states respectively. These mixings yield model dependence though the gauge interactions are completely fixed by the symmetry and the matter multiplet structure. Hence in the SUSY particles search, we must account for the model dependence particularly for their decay branching ratios. In addition, most of the SUSY models respect

R parity conservation where R is defined as;

$$R = (-1)^{2J+3B+L} = \begin{cases} +1 & \text{for conventional particles} \\ -1 & \text{for supersymmetric particles} \end{cases}$$

where J, B, L indicate spin, baryon number and lepton number respectively. R parity conservation means that SUSY particles should be pair produced and the lightest SUSY particle (LSP) must be stable. If R parity is not conserved, protons decay through the diagram shown in the fig.1 which causes rapid proton decay. By cosmological arguments, the LSP is suggested to be colorless and chargeless. Thus the candidates of the LSP are the photino, the neutral higgsino, the zino and the scalar neutrino. In this analysis, we assume the LSP is photino (superpartner of photon) which is most popular choice.

The model dependence of the masses of the superparticles are described in chapter 7 and appendix B.

3. Signatures of the SUSY in the e^+e^-interactions

The Feynman diagrams of the SUSY production in e^+e^-interactions are shown in fig.2. In the e^+e^-interaction, detection of the SUSY particle is definitely easier comparing with the $p\bar{p}$ interaction. Since the electrons and positrons are themselves elementary particles, the initial state is uniquely determined and the events are clean. On the other hand, protons are composite of the three quarks and the gluons, therefore in the $p\bar{p}$ interactions, initial states are not determined uniquely and the final states are very complicated. In particular, SUSY searches are the search for the events with missing energy and momentum, the e^+e^-collision is advantageous then the $p\bar{p}$ experiments.

If the beam energy is enough, the SUSY particles can be pair produced by the e^+e^-colliders as shown in fig.2 (a), (b), (e), (f), or can be produced associated with the lighter SUSY particles (fig.2 (c), (d), (g), (h)). While the searchable mass is limited up to the beam energy in the pair production, the associated production allow us to probe up to the center of the mass ($\sqrt{s}$) energy. However the search for the associated production needs relatively higher integrated luminosity than the pair production case, our analysis concentrated on the pair production. Further, we neglected the contribution from the Z^0 since it was small in the energy region of this analysis and made positive contribution to the cross section. In this sense our results are conservative. On the other hand, the cross section was calculated including the initial state photon radiation[17] , except for scalar electrons, which reduce the cross section near the threshold.

3.1 Scalar fermions

The weak eigen states of scalar leptons are $\tilde{l}_L$ and $\tilde{l}_R$ which are the partners of the left and right handed leptons. In site of possible mixing the left- and the right-handed partners are usually approximately mass eigen states. Therefore we assume they are mass eigen states and examine the two extreme cases: $m_L >> m_R$ and $m_L = m_R$. Under these assumptions, the production cross-section for $\tilde{\mu}$, $\tilde{\tau}$, and $\tilde{q}$ is given by;

$$\frac{d\sigma}{d\Omega} = \frac{\alpha^2 Q^2}{8s} C\beta^3 sin^2\theta \tag{3.1}$$

where $s = 4E^2_{beam}$, β and Q are velocity and electric charge of the produced particle,

respectively. The factor C is the color factor which is 1 for scalar leptons and is 3 for scalar quarks. When $\tilde{m}_L = \tilde{m}_R$, both particles can be pair produced and the cross-section is doubles.

The cross section for the scalar electron is more complicated since the t-channel contribution of the photino exchange is added as shown in fig.2 (b)[18] ;

$$\frac{d\sigma}{d\Omega} = \frac{\alpha^2}{16s}\beta^3 sin^2\theta \times \{1 + [1 - \frac{4}{1 - 2\beta cos\theta + \beta^2 + \mu^2}]^2\} \tag{3.2}$$

for $\tilde{m}_L >> \tilde{m}_R$ and

$$\frac{d\sigma}{d\Omega} = \frac{\alpha^2}{8s}[\beta^3 sin^2\theta \times \{1 + [1 - \frac{4}{1 - 2\beta cos\theta + \beta^2 + \mu^2}]^2\} + \frac{16\mu^2\beta}{1 - 2\beta cos\theta + \beta^2 + \mu^2}] \tag{3.3}$$

for $\tilde{m}_L = \tilde{m}_R$, where $\mu = m_{\tilde{\gamma}}/E_{beam}$ and β is a velocity of the electron. Total cross-sections at $\sqrt{s} = 55GeV$ are shown in fig.3.

The decay of the scalar lepton, $\tilde{l}$, is simple. It promptly decays into $l + \tilde{\gamma}$ and $\tilde{\gamma}$ leaves from the detector like a neutrino because of the R parity conservation. On the other hand, the scalar quark decay is more complicated since it has color charge which causes hadronization. In the hadronization, the scalar quarks couple with the conventional quarks and forms an R hadron. We treated the subsequent decay of the leading R-hadron containing the scalar quark by the spectator model with the LUND string fragmentation[19] .

3.2 Chargino

In general, charginos ($\tilde{\chi}^{\pm}$), are two mass eigen states resulting from the mixing of the wino (the SUSY partner of the W) and the charged higgsino (the SUSY partner of the charged Higgs). The target of our search is the lighter of the two chargino states. The pair production of the chargino takes place through the s-channel one γ/Z^0 annihilation or through the t-channel scalar neutrino exchange as shown in fig.2 (f).

We ignore the t-channel contribution, assuming the scalar neutrino mass is heavy. Hence the production cross section is given by

$$\frac{d\sigma}{d\Omega} = \frac{\alpha^2}{4s}\{(1+cos^2\theta) + (1-\beta^2)sin^2\theta\}$$

The chargino decays into conventional fermions and a photino when the LSP is the photino;

$$\tilde{\chi} \longrightarrow f\bar{f}\nu\,\tilde{\gamma}$$

where f is e, or μ, or τ, or q.
Their decay depends strongly on the mixing. This model dependence enters in two ways: the first is from the $W\,\tilde{\chi}\tilde{\gamma}$ vertex and the second from the $f\,\tilde{f}\tilde{\chi}$ vertex, as shown in figs.4(a) and (b), respectively. In the first diagram, the model dependence lies only in the $W\,\tilde{\chi}\tilde{\gamma}$ vertex. In the second diagram (fig.4 (b)), the mass and the width of the scalar leptons or quarks introduce another model dependence. The contribution of this second diagram to the branching fraction depends rather strongly on the mixing, since higgsinos have a coupling strength proportional to the fermion mass involved. Thus chargino can decay into following four modes when the LSP is a photino: (i) $e\bar{\nu}\,\tilde{\gamma}$; (ii) $\mu\bar{\nu}\,\tilde{\gamma}$; (iii) $\tau\bar{\nu}\,\tilde{\gamma}$; and (iv) $q\bar{q}\,\tilde{\gamma}$.

3.3 Previous SUSY search

The SUSY particles search were made in many experiments, both in the e^+e^- colliders at PEP, PETRA and in the $p\bar{p}$ collider at CERN[10] . The groups at PETRA studied the scalar fermions, the charginos and the neutralinos by a similar method to us at energy up to $\sqrt{s} = 46.8GeV$. The ASP group at PEP studied the reaction

$$e^+e^- \longrightarrow \gamma\,\tilde{\gamma}\tilde{\gamma}$$
$$e^+e^- \longrightarrow \gamma\,\tilde{\nu}\tilde{\nu}$$

by tagging the γ from the initial state photon radiation and obtained the mass limit for scalar electron, $\tilde{\gamma}$ and wino (pure state of the partner of the W)[11] . The UA2 group at CERN obtained the mass limit for the wino by studying the decay of the Z^0 and the W bosons when the winos decay only into a scalar neutrino and a lepton[12] . The UA1 group reported the lower mass limit for the scalar quarks and leptons. This limit was obtained in the cases $m_{\tilde{q}_R} = m_{\tilde{q}_L}$ and $m_{\tilde{u}} = m_{\tilde{d}} = m_{\tilde{c}} = m_{\tilde{s}} = m_{\tilde{b}}$[13] . The results of the previous searches are summarized in table.2.

4. Experimental Apparatus

4.1 The TRISTAN accelerator

The TRISTAN is a e^+e^-colliding accelerator at National Laboratory for High Energy Physics (KEK). The accelerator complex is shown in fig.5. It consists of a 400 m linear accelerator (LINAC), an accumulator ring (AR) and a main ring (MR) of about 3 km circumference. First, electrons and positrons are accelerated by the LINAC up to 2.5 GeV and injected to the AR. They are accumulated in the AR and are accelerated to 8 GeV and injected to the MR. After repeated injections, when the intensity of the beam become sufficient for the experiment, they are finally accelerated to the highest energy and collide. The running beam energy was 25 GeV at May 1987 and had been raised up to 28.5 GeV in the experimental cycle of summer 1988. The luminosity in the latest experiment (July 1988) was 100 $\sim$ 300 nb^{-1}/day.

4.2 The TOPAZ detector

The TOPAZ detector[20] is a general purpose detector located at the north west (Tsukuba) experimental hall in the TRISTAN main ring. It adopts time projection chamber as the main tracking device and has a good capability of three dimensional tracking and particle identification by the dE/dx measurement. The bird's eye and the cross sectional views of the detector are shown in fig.6 a and b, respectively. Notice that the contribution of the author to the detector as a member of the High Energy Physics Laboratory of Nagoya university was constructions of the end cap calorimeter and the end cap drift chamber[21] . The TOPAZ started physics data run on May 1987 at the energy of $\sqrt{s} = 50$ GeV and has accumulated an integrated luminosity of 11 pb^{-1} up to the energy of $\sqrt{s} = 57$ GeV by summer 1988.

The detail of the detector is described in the following sections putting emphasis on the time projection chamber(TPC), the barrel calorimeter(BCL), and the end cap calorimeter(ECL) which were mainly used in this analysis.

The coordinate system of the TOPAZ detector used throughout in this paper is defined in fig.7.

The time projection chamber

The Time Projection Chamber (TPC)[22] is a multi wire drift chamber which has a large drift region (fig.8). It features precise measurements of charged tracks in 3-dimensional coordinates together with ionization energy loss of each track used for particle identification. The charged tracks, passing through in the sense volume filled with the gas mixture of $Ar : CH_4 = 90 : 10$ at 3.5 atm, liberalized electrons of the gas molecules. These electrons drifted toward the end plane along the electric field of 353 V/cm applied parallel to the beam axis. Since the gas was pressurized and the electric field was parallel to the magnetic filed of 1 Tesla, the diffusion of the electron clusters was suppressed and these electron clusters preserved a precise information of the trajectory of the charged tracks. The electrons clusters were detected by the 8 multi-wire proportional counters (sectors) at each end of the drift region shown in fig.9. A sector had 175 sense wires and 10 pad rows on the cathode plane. The signal from each wire or pad was amplified and shaped by an analog electronics and then sampled and stored in a charge coupled devise (CCD) at a rate of 10 MHz.
We should mention the wire plane called the gating grid. Without the gating grid, positive ions generated around the sense wires would built up in the sense volume and caused the distortion of the electric field. The effect could result in a distortion of reconstructed tracks as large as a few cm. To avoid such effect the gating grid was employed as shown in fig.10. The gating grid was usually closed so that positive ions could not flow into the sensitive volume and only opened by the request from the other detectors. The scheme to open the gating grid is described in the later section. The gains of the wires were calibrated by the X ray from the F_e^{55} sources which were important to achieve good dE/dx resolution. The gain differences of the electronicses were calibrated by the test pulse input to the shielding grid.

The performance of the TPC is described in next chapter since it is deeply related with the track reconstruction.

Barrel Calorimeter

The Barrel Calorimeter (BCL)[23] was an electromagnetic calorimeter consist of 4300 lead-glass (SF6W) Čherenkov counters with a length of $18X_0$. As illustrated in fig.11 , the BCL had a cylindrical shape with an axial length of 5.6 m and an inner radius of 1.76 m. It was located outside superconducting solenoid and covers 85% of

the full solid angle corresponding to $32° < \theta < 148°$. The BCL was segmented into 45 blocks in z-direction and 96 blocks in ϕ direction. The signal from the Čherenkov counters were amplified by photomultipliers and sent to ADCs though $40m$ long coaxial cables. The signal of the BCL was also used for the trigger as described later. The gain of each counter had been calibrated by an electron beam before installation and was monitored with an accuracy of 1.2% by a Xenon flush lamp which was distributed to each counter through optical fiber cables. Fig.12 shows the energy distribution for Bhabha events at $\sqrt{s} = 52$ GeV and obtained the energy resolution of 4.5 % for the events. The energy resolution of the BCL was $\sigma_E/E = \sqrt{(8/\sqrt{E})^2 + 4.2^2}\%$, where E in GeV, and the angular resolution was 0.38°

End Cap Calorimeter

The End Cap Calorimeter (ECL)[24] was located in the end cap region of the TOPAZ and covers 10% of the full solid angle corresponding to $0.82 < |cos\theta| < 0.98$. The ECL was a lead proportional-counter sandwich type electromagnetic calorimeter with a length of $18X_0$. A schematic view of the detector is shown in fig.13. Proportional counters were made of conductive plastic tubes filled with the gas mixture of $Ar : CH_4 = 95 : 5$. The signal from the ECL was read by cathode pads etched on the a G-10 board which were a arranged to form tower structure toward the beam interaction points. Each tower was sub-divided into three modules along the z-direction. The total readout channels was amount to 960 for each end cap. The signals of the cathode pads, directly drove 40 m long twisted pair cables, were received by the differential amplifiers to suppress common mode noise induced on the cables, and were finally digitized by ADCs. As with the BCL, the signal from the ECL was used for the trigger. Variation of the gas gain was calibrated by continuous monitoring of the pressure and the temperature of the counter gas. The absolute gain was determined by Bhabha events in beam runs. Fig.14 shows the energy distribution for Bhabha events at $\sqrt{s} = 52$ GeV and obtained the energy resolution of 6.7 % for the events. The angular resolution was 0.7°. Notice that the integrated luminosity used in the normalization of all the data taken by the TOPAZ was calculated from the number of Bhabha events detected by the ECL. A typical systematic error of the integrated luminosity was estimated to be 4.0 %. The detail of the ECL is described in appendix C.

Inner Drift Chamber

The Inner Drift Chamber (IDC)[25] was the innermost detector in the TOPAZ. It was used for tracking of charged tracks to assist the TPC tracking, for identifying photons which were sometimes converted at the inner pressure vessel of the TPC, and for generating a charged track trigger information. The IDC is a 10-layer cylindrical drift chamber with cathode delay lines to measure position in z-direction. Its spatial resolutions were $(\sigma_{r\phi}) = 220\mu m$ and $\sigma_Z = 1cm$ respectively.

End Cap Drift Chamber

The End Cap Drift Chamber (EDC)[26] was located in front of the ECL. It was made of conductive plastic tubes filled with the gas mixture of $Ar : C_2H_6 = 20 : 80$ and was operated in the limited streamer mode. The aim of the chamber was to improve momentum resolution in the end cap region where the TPC less its acceptance.

Time of Flight Counter

Outside of the superconducting solenoid, the time of flight counter[27] (TOF), which consisted of 64 scintillation counters, was placed. The time resolution of the counter was 220 ps. The TOF was used for particle identification by time of flight measurement and plays an essential role for cosmic ray rejection. It was also used for the charged track trigger together with IDC.

Barrel Muon Counter

The outermost detector of the TOPAZ was the barrel muon counter (BMU), consisting of three layers of drift chamber array interleaved with ion filters. The BMU identified muons which pass through the ion filters while hadrons were absorbed by the filters.

Luminosity Monitor

The luminosity monitor (LUM)[28] was a lead-scintillator sandwich type calorimeter with a scintillation counter in front of them to define acceptance. It was placed at 2.4 m from the interaction point and detected small angle Bhabha scattering events. The LUM provided a real time luminosity which was fed back to tune accelerator condition.

Superconducting Solenoid Magnet

A thin superconducting solenoid magnet[29] was located outside the TPC. It provided uniform magnetic field of 1 Tesla parallel to the beam axis. In order not to degrade energy resolution of the calorimeter outside the magnet, its thickness must be as thin as possible. Great effort was made for this purpose resulting in a thickness of $0.7X_0$.

4.3 Trigger system

The data size of the TOPAZ detector was about 100 kB for a multi-hadron event and was about 20 kB for a two prong event such as μ pair production which was quit large due to the TPC data size. In order to keep dead time less than 10 %, trigger rate should be smaller than 3 Hz. However, beam gas, spent electron, and cosmic ray events were huge back ground sources of high trigger rate, while the rate of physical events we need was at most 10^{-2} Hz even for Bhabha scattering which has one of the highest cross section in concern. In data analysis, it was important to understand trigger efficiency for each physics channel, because its efficiency acted as an implicit cut on our data. Here we describe the trigger in detail.

To achieve the rate requirements, the TOPAZ trigger used r-z information of the TPC. Since it took $24\mu sec$ (i.e, drift time of electrons in the TPC) to make trigger decision and since the frequency of gating pulse should be kept as low as possible to avoid the distortion effect, the trigger system consisted of multiple steps. Whole scheme of the trigger system is shown in fig. 15. The first step was called the pre-trigger and was done between two successive beam cross signal (BC/O) which was $5\mu sec$ apart in two bunch operation. The second step was done by the TPC and was called the TPC trigger. The pre-trigger consisted of two parts, one was the energy trigger using the calorimetric information and called the forced pre-trigger which did not require any decision by the TPC, the other was the track pre-trigger which was generated by the combination of the IDC and the TOF. For the track pre-trigger, further decision by the TPC was required. These pre-triggers were also used to open the gating grid of the TPC after synchronized with BC/O. If the pre-trigger was not generated, all ADCs and TDCs were cleared and waited for next BC/O. When the track pre-trigger was issued, the TPC decides whether triggered or not and when not

triggered, sent reset/abort (R/A) to the online system. Timing sequence of the trigger is shown in fig. 18.

Energy Trigger

The energy deposit of the BCL was grouped into three segments along the beam axis (called the partial sums) and the sum of the three formed the total energy sum. The energy trigger was generated by the AND of two of the three partial sums or solely by the total sum. The threshold level was set at 1 GeV for partial sums and 4 GeV for the total sum, respectively.

The ECL was divided into outer and inner cylinders. The energy deposit in each cylinder was called the partial sum. Two partial sums of each end-cap were ORed and the ORed partial sums of both end-caps were ANDed to generate the partial energy trigger. All the partial sums were summed to make the total energy trigger. The schematic diagram of the energy trigger is shown in fig.16. The thresholds of the partial sums and the total sum were set at 4 GeV and 10 GeV respectively.

In addition to these energy triggers, the AND of a partial sum of the BCL and a partial sum of the ECL was used as the combination trigger.

Track Pre-Trigger

The track pre-trigger was composed of the IDC track finder and the TOF.
Fig. 17 illustrates the principle of the trigger schematically. In the IDC, anode wire was grouped into 64 subsectors in $r - \phi$ plane and track finding was performed each the subsector. The hit pattern to define a track candidate was chosen according to the beam condition and was down loaded before the operation. It was currently set to recognize tracks of Pt greater then about 600 MeV. When used in the trigger, outputs of the successive two track finders were ORed.

Track candidates in the IDC were checked if associated with TOF hits which was also ORed into 32 informations. This requirement actually selected tracks with a transverse momentum greater than about 800 MeV. The signals from 32 outputs were processed by a topology decision module which required two or more tracks with their opening angle greater than 45°.

TPC Trigger

The TPC trigger consists of the ripple trigger and the vertex finder. The TPC trigger used inner 88 of 176 sense wires of each sector. In the ripple trigger, 88 wires were grouped into 11 successive subgroups as shown in fig.19 a. The ripple trigger required all hits of 11 groups for a track candidate as shown in fig. 19 b. Tracks recognized by the ripple trigger were processed by the vertex finder. It extrapolated the tracks to the interaction region using the two points given by the ripple trigger. The accuracy of the vertex pointing was about 10 *cm*. Fig. 19 c shows the scheme of the vertex finder.

A TPC trigger was issued when the +Z and -Z detector halves both contain at least one track(Phase-I trigger). The TPC track requirement was relaxed for the higher energy run and 2/3 of the 55 GeV run to accept events containing two or more tracks with an opening angle greater than 45°(Phase-II trigger).

4.4 Data Acquisition System

The data acquisition system (DAS) of the TOPAZ was based on the FASTBAS which is a modular high speed data acquisition control system[31] . The topology of the system is shown in fig. 20. Since the TPC had larger data size than the other detectors, the DAS was separated into the TPC and the non-TPC parts. The data acquisition sequence, which was controlled by the interrupt control system (ICS) was complicated in order to reduce dead time in spite of the large data size of the TPC. In fig. 21, the time sequence of the data acquisition system is shown. When a trigger was issued by the trigger system, the ICS waited for the data ready of the non-TPC part and, when the date are ready, interrupted the main data taking computer VAX11/780 to read the data, while the TPC datas were being digitized. When the TPC datas were ready, the ICS interrupted the VAX to request the readout of the TPC data.

The data taken by the VAX was sent to the main computer, FACOM M780, through an optical fiber link by the VAX-FACOM interface called DACU. The tasks running on the VAX are shown in fig. 22.

A typical data taking cycle took 25 *ms* and overall dead time was less than 10 % in the actual operation.

5. Raw Data Processing

5.1 Flow of data processing

Fig.23 shows the flow of the data processing. The data sent from the VAX were first written on temporary disks of the FACOM M780 which was our main frame computer for the analysis. These data were copied to magnetic tapes and formatted in the data format of the Tristan Bank System (TBS) which was our data handling system. These formatted data were stored as raw data. The contents of raw data were outputs of each detector, i.e;

◇ ADC counts of the BCL and the ECL;

◇ TDC counts of the EDC, the BMU, and the IDC;

◇ TDC and ADC counts of the TOF;

◇ digitizer outputs of the TPC.

From the raw data, physical observable we need, which are essentially two four vectors, p^μ and x^μ, for each track, were calculated. It was done by two step called reduction and production.
In the reduction step, the raw data were corrected by the hardware dependent calibration constants such as channel by channel gain variation and were filtered to reduce jank events which were beam gas or spent electron events. The criteria of the filtering was the same as those of the trigger and consists of;

◇ the BCL total energy and the partial energy combination check

◇ the ECL total energy and the partial energy combination check

◇ the ECL-BCL partial energy combination check

◇ the TPC trigger condition check

The events passed the filter if it satisfied at least one condition.

The data pass through the reduction were processed by the production. In the production step the informations of the each detector were converted to the physical information, i.e,

♡ momentum and vertex position of each charged track

♡ particle ID information

♡ energy cluster of the calorimeters

In next section the detail of the track reconstruction by the TPC and the energy cluster reconstruction by the BCL and the ECL is described.

5.2 Track reconstruction and parametrization

As the TPC provides three dimensional space points, track finding and fitting made full use of this advantage. The detail of the TPC tracking is described in ref. 32. The architecture of the TPC analysis in show in fig. 24. First, space points were made from pad information of the sectors and tracks were found in the $\phi - Z(R_{ref})$ plane, where ϕ was azimuthal angle and $Z(R_{ref})$ was defined as

$$Z(R_{ref}) = \frac{ZR}{R_{ref}}$$

where R_{ref} was a constant.
In the $\phi - Z(R_{ref})$ pane, space points of a single track from origin clustered around a single point.

Tracks found were fitted to a helix parameterized as follows,

$$\begin{aligned} x &= x_0 + d_\rho \cos\phi_0 + \frac{1}{\kappa}\left(\cos\phi_0 - \cos\left(\phi + \phi_0\right)\right) \\ y &= y_0 + d_\rho \sin\phi_0 + \frac{1}{\kappa}\left(\sin\phi_0 - \sin\left(\phi + \phi_0\right)\right) \\ z &= z_0 + d_z + \frac{\beta}{\kappa}\phi. \end{aligned}$$

where fit parameters were

$$\alpha = \begin{pmatrix} d_\rho \\ \phi_0 \\ \kappa \\ d_z \\ \beta \end{pmatrix} = \begin{pmatrix} d_\rho \\ \phi_0 \\ \frac{1}{\rho} \\ d_z \\ \tan\lambda \end{pmatrix}.$$

The meaning of these parameters are illustrated in fig. 25.

Although the gating grid suppress the distortion of the electric field in the TPC, a small amount of the distortion remained. This distortion was corrected by comparing two cosmic ray data when the beam was on and off. The alignment of the position of the sectors was done by comparing a cosmic ray track reconstructed in the two sectors. The momentum resolution of the TPC was studied by cosmic ray events. Fig.26 shows the distribution of the curvature difference of a cosmic ray track reconstructed by two sectors. The momentum resolution as a function of momentum is shown in fig.27 and obtained $\delta p_t/p_t = \sqrt{(1.5\% p_t)^2 + 1.5^2\%}$, where p_t is a transverse momentum in GeV.

5.3 Reconstruction of energy clusters

From the data, which were correction of energy deposit in each counter, we must reconstruct energy clusters corresponding to the energy deposit of each particle. The methods of the clustering were slightly different between the BCL and the ECL due to the difference in their structures.

The BCL clustering procedure was done as follows;

1. search the counter which had the largest energy E1;
2. pick up neighbouring counters of 1, which had the energy E2, and included them to the cluster 1;
3. pick up neighbouring counters of 2, which had the energy E3, and appended them to the cluster if

$$E2 > C1E1$$

$$or \quad E3 < C2E1 \text{ and } \mathrm{E3} < \mathrm{C3E2}$$

where C1,C2,C3 were constants to be tuned and were set to 0.65, 0.08, and 1.20, respectively.
This procedure was repeated until all the counters with an energy greater than 45 MeV were used.

For the clusters recognized in this procedure, their positions were calculated as the averaged counter positions weighted by their energies;

$$\mathrm{X} = \frac{\sum_i \mathrm{X_i} \cdot \mathrm{E_i^p}}{\sum_i \mathrm{E_i^p}}$$

where p was an empirical constant and was set to 0.26 for z and 0.34 for ϕ directions.

The clustering method for the ECL was simpler than that for the BCL. First, search the tower which has the largest energy, then towers within an angle of 0.16 radian around the highest tower were grouped into a cluster. This procedure was repeated until all the towers having the energy greater than 50 MeV were used. The cluster positions were determined similarly to the BCL case except that the directions were θ and ϕ and the parameter p was set to 1 for both directions.

5.4 Integrated luminosity

The number of events expected is given by;

$$N_{exp} = \epsilon \sigma L$$

where N_{exp}, ϵ, σ, and L are the number of events expected, the detection efficiency, the cross section, and the integrated luminosity. In this analysis, the integrated luminosity was obtained from the number of Bhabha events detected by the ECL. The Bhabha events were selected by requiring; (i) more than or equal two clusters with the energy greater the $1/3E_{beam}$, (ii) acollinearity angle between the clusters are least the 10°, and (iii) $0.89 < |cos\theta_{z+cluster}| < 0.96$. The error was the quadratic summation of the statistical and the systematic error. The systematic error was estimated by the dependence of the luminosity on the ϕ of the ECL resulting in the typical error of 4 %.

6. Analysis

6.1 Overall strategy

Before describing the search for charged supersymmetric particles, ($\tilde{e}$, $\tilde{\mu}$, $\tilde{\tau}$), scalar quarks ($\tilde{q}$), and charginos ($\tilde{\chi}$), overall strategy of the search is described since, although details of the analysis may depend on each channel, the underlying concept of the search is common. The flow diagram of the analysis is shown in fig.28.

Event signature

Throughout this paper we assume the lightest supersymmetric particle is the photino ($\tilde{\gamma}$). Because of the R-parity conservation, the photino is stable and escapes our detector without leaving any signal. Therefore the event signature of the SUSY particle is characterized by the lepton pair production or the multihadton production with a missing energy and momentum. The main backgrounds contribute to the SUSY signal are the two photon processes and the ordinary fermion pair production through one photon annihilation with an initial state photon radiation. The two photon processes are;

$$e^+e^- \longrightarrow e^+e^- f\bar{f}$$

and the ordinary fermion pair production are; (including an initial state photon radiation)

$$e^+e^- \longrightarrow f\bar{f}\gamma.$$

The electrons and the positrons in the two photon processes and the photons in the fermion pair productions usually escape into the beam pipe and fake a missing energy momentum as shown in fig.29 (a). However by imposing a cut on the acoplanarity angle, which is defined to be the angle between observed leptons or jets projected on the $x-y$ plane, these backgrounds are efficiently removed. Fig.29 (b) and (d) show the acoplanarity angle for the background processes and the signals, respectively. Both the backgrounds and the signals are acollinear (fig.29 (a) and (c)) but the backgrounds have a coplanar shape while the signals form acoplanar events (fig.29 (b) and (d)).

6.2 Event Simulation

To estimate the acceptance of the detector for the SUSY signals, the Monte Calro simulation was used. The simulation consists of two part, i.e, the event generation and the detector simulation. In the event generation, four momentum of the generated particles were calculated according to their production mechanism and decay if it was necessary. The detector simulator emulated response of the detectors and generated the signals of them. These simulated signals were processed by the same reconstruction and analysis programs as the real data.

Event Generation

First, the event generator made four momentum of the charginos or the scalar fermions according to their production mechanisms which are shown in fig.2. In the cases without the scalar electrons, we took into account the initial state photon radiative correction by the Berends Kleiss method[17] which reduces the total cross sections near threshold. The Feynman diagrams took into account for the correction are shown in fig.30. The cross section for the one photon radiation is given by the form;

$$\begin{aligned} \frac{d^2\sigma}{dx} &= \frac{\alpha}{\pi}\left(ln\frac{s}{m_e^2}\right)\frac{1+(1-x)^2}{x}\sigma_X(s') \\ x &= E_\gamma/E_{beam} \\ y &= cos\theta_\gamma \\ s' &= (1-x)s \end{aligned} \tag{6.1}$$

where $\sigma_X(s')$ is the total cross section of the lowest order diagram at the reduced CMS energy ($\sqrt{s'}$). Since e.q.(6.1) is singular at $x = 0$ and $x = 1$, the integration of e.q.(6.1) must be cut at some appropriate value x_{min} and x_{max}. The x_{min} represent that the photons which have energy below $x_{min}E_{beam}$ are not recognized as the photons by the detectors, and is set at 0.1. The x_{max} is set at 0.99. Because the kinematically allowed energy of the photons less than $E_{beam}-m$, where m is the mass of the generated particles, the x_{max} does not affect the result as long as $x_{max}E_{beam} > E_{beam} - m$. In the scalar electron production, since the t-channel contribution in the diagram prevent us to use the Berends Kleiss method, we did not take into account the initial state photon radiation.

In the chargino decay, its decay strongly depends on the mixing. This model dependence enters the coupling in the $W\ \tilde{\chi}\tilde{\gamma}$ vertex of fig.4 (a) and the lepton mass at the $f\ \tilde{f}\tilde{\chi}$ vertex of fig.4 (b). In the first diagram, the coupling at the $W\ \tilde{\chi}\tilde{\gamma}$ is expressed as

$$\frac{ie}{2}\gamma^{\mu}[U(1+\gamma_5)+V(1-\gamma_5)]$$

where U, V are parameters depending on the mixing of the charginos. We tried four cases for the coupling, i.e,

$$(U,V)=\begin{cases}(0,1), & \text{V-A}\\ (1,0), & \text{V+A}\\ (1,1), & \text{V}\\ (1,-1), & \text{A}\end{cases}$$

It turned out that the detection efficiencies depend only slightly on the coupling. We chose the case which had the poorest efficiency yielding the most conservative result. In the second diagram, the mass and the width of the scalar leptons or quarks were assumed to be 90 GeV and 1 GeV respectively. Our final limits dependence on these parameters was small unless these masses are made much lighter.

Detector Simulation

The particles generated by the event generator were processed by the detector simulator. In the simulator, the particles were traced along their pass in the detector volume suffering from the interaction between particles and materials in the detector, i.e, the ionization energy loss, the multiple scattering, and the nuclear interactions. The electromagnetic shower in the dense materials was treated by the EGS[33] code. The nuclear interactions were treated by the GHEISHA[34] Monte Calro. When a particle was in the sense volume of a detector the detector simulator converted its position and energy loss to the outputs of the detector. In the TPC, each wire signal was generated from the energy loss of the track. A pad signal was calculated by the induced signal on a pad by nearest 5 wires. In the BCL, the electromagnetic shower was simulated by the Bootstrap method[35] since the full simulation by the EGS takes much CPU time. The Bootstrap method simulated the shower by the EGS until the energy of the particle reduced to the half of the incident energy and the development of the low energy shower was chosen from pre-simulated shower (the frozen shower)

table. The frozen showers were prepared using the EGS with the cut off energy of 1 MeV for various energies. In the ECL, the shower energy was calculated by the shower curve which was experimentally determined.

6.3 Search for charginos

As mentioned in the previous section , charginos ($\tilde{\chi}$) are mixtures of winos and charged higgsinos. Their production cross-section and decay was described in chapter 3. Taking account for the model dependence of the chargino decay, we looked for production of chargino pairs both decaying by the same mode in the following four final states; acoplanar $e\bar{e}$ pair, acoplanar $\mu\bar{\mu}$ pair, acoplanar $\tau\bar{\tau}$ pair, and acoplanar jets.

Acoplanar $e\bar{e}$ pairs

The selection criteria for acoplanar $e\bar{e}$ pairs was as follows:

1. No ECL energy cluster with E > 2 GeV.
2. Two energy clusters in the BCL with E > 2.5 GeV and acollinearity angle > 20°.
3. At least one of these energy clusters had to be associated with a charged track, and both of them with matched IDC hits.
4. The rest of the energy deposits in the BCL < 1.5 GeV.
5. The missing energy vector could not point toward the calorimetric holes nor gaps.
6. The missing E_t has to be greater than 5 GeV.
7. The acoplanarity angle of the event, θ_A, must be greater than 30° where θ_A = 180° − the angle between the momenta of the two clusters projected on the plane perpendicular to the beam axis.

Bhabha and two photon events were removed by cuts (7) and (8). Cuts (1) and (6) removed radiative Bhabha events. Since the required energy deposit in the BCL was greater than 5 GeV, the trigger efficiency for events survived the cuts was 100 %. The plot before the missing energy and the acoplanarity cuts is shown in fig.31 together with the simulation. With these cuts, the efficiency to detect chargino pairs decaying into $e\bar{\nu}\,\tilde{\gamma}$ was 0.35

when $(m_{\tilde{\chi}}, m_{\tilde{\gamma}})$ = (25,0) GeV. No events were observed after applying all the cuts. The expected backgrounds from Bhabha, $(e\bar{e})e\bar{e}$, and $\tau\bar{\tau}$ processes were 0.01 in the search region.

Acoplanar $\mu\bar{\mu}$ pairs

The selection criteria for acoplanar $\mu\bar{\mu}$ pairs was less complicated:

1. No energy cluster was allowed in the BCL nor the ECL with E > 1 GeV.
2. At least two, but no more than three charged tracks from the interaction point were allowed (the highest two momentum tracks are the candidate μ tracks).
3. Zero net charge of the μ track candidates.
4. The lower momentum candidate had to have a momentum greater than 4 GeV.
5. The acoplanarity angle of the candidates had to satisfy $\theta_A > 30°$.

The dominant background source of this mode was $(e\bar{e})\mu\bar{\mu}$, which was efficiently removed by cut (4). For this channel the trigger condition described in the previous chapter affects significantly the detection efficiency and was simulated by the trigger simulation of the TOPAZ. The plot before the momentum and the acoplanarity cuts is shown in fig.32 together with the simulation. The simulation well reproduced the real data. With these cuts, the efficiency to detect chargino pairs decaying into $\mu\bar{\nu}\,\tilde{\gamma}$ was 0.13 for the phase-I TPC trigger and 0.22 for the phase-II TPC trigger when $(m_{\tilde{\chi}}, m_{\tilde{\gamma}})$ = (25,0) GeV. The total expected background was 1.6 events in the search region. We found no candidate events.

Acoplanar $\tau\bar{\tau}$ pairs

Since the 86% of the τ's decay into one charged track states, acoplanar τ pair events were searched for in the 1-1 and 1-n prong configurations. 1-1 means the both τ's decay in the one-prong mode and 1-n means one decays in one-prong and the other in n prong mode. The notation indicate the number of tracks in opposing directions. The selection criteria for the 1-1 mode were:

1. Two charged tracks with momentum greater than 1 GeV, which pointed to the interaction point.
2. E_{BCL} < 18.5 GeV.

3. $E_{ECL} < 1$ GeV.

4. $E_{vis} < 35.5$ GeV.

5. $|\Sigma p_z|/E_{vis} < 0.38$.

6. $|\cos\theta_{missing\ p}| < 0.75$.

7. Missing $p_t > 5$ GeV.

8. Acoplanarity angle of the two tracks, $25° < \theta_A < 160°$.

Bhabha events were removed by cut (2), radiative lepton pair production was rejected by cuts (3) and (6). $(e\bar{e})e\bar{e}$ and $(e\bar{e})\mu\bar{\mu}$, which give dominant background contribution, were removed by cut (7). The cut (8) removed $\tau\bar{\tau}$ process. In fig.33, the plot before the missing momentum and the acoplanarity cuts is shown.

The selection criteria for the 1-n mode were more complicated, necessary in order to suppress backgrounds from multi-hadron events:

1. At least three but no more than six charged tracks from the interaction point.

2. $E_{BCL} < 16.5$ GeV.

3. $E_{ECL} < 1$ GeV.

4. 7.5 GeV $< E_{vis} < 49.0$ GeV.

5. $|\Sigma p_z|/E_{vis} < 0.67$.

6. $|\cos\theta_{missing\ p}| < 0.75$.

7. Invariant mass of 1-prong side < 2.4 GeV and invariant mass of n-prong side < 6.7 GeV.

8. The largest isolation angle $> 10°$.

9. The largest opening angle of charged particles on the n-prong side satisfying $\delta_{max} < 50°$.

10. Acoplanarity angle, $\theta_A > 40°$, where $\theta_A = 180° -$ the angle between the vectorial sums of the transverse momenta of the 1-prong side (the track and the clusters, if any, contained in the cone about the track with an opening angle less than the half of the largest isolation angle) and of the n-prong side (the rest).

Cuts (2),(7), and (9) removed multi-hadron events and cut (10) suppressed $\tau\bar{\tau}$ events. In the fig.34, the plot before the acoplanarity cuts is shown. With these cuts,

the efficiency to detect chargino pairs decaying into $\tau\overline{\nu}\,\tilde{\gamma}$ was 0.10 when $(m_{\tilde{\chi}}, m_{\tilde{\gamma}}) =$ (25,0) GeV. Possible background sources included $(e\overline{e})\mu\overline{\mu}$, $(e\overline{e})\tau\overline{\tau}$, $\tau\overline{\tau}$, Bhabha, multi-hadron, and $(e\overline{e})q\overline{q}$. The background expected in the search region were 0.2 and 0.7 events for the 1-1 and 1-n mode respectively. One event survived the cuts but consistent with the background expectation. We kept the event as a candidate in the limit calculation.

Acoplanar jets

The selection criteria for acoplanar jets consisted of the following requirements:

1. Total energy deposit in the calorimeter > 4 GeV.
2. More than four tracks each with $p_t > 0.15$ GeV and $|\cos\theta| < 0.83$ originating from the interaction point.
3. The larger of the invariant masses in the two hemispheres > 4 GeV.
4. $|\cos\theta_{thrust\ axis}| < 0.7$.
5. $0.3 < \mathrm{E_{vis}}/\sqrt{\mathrm{s}} < 1.0$; $|\Sigma \mathrm{p_z}|/\mathrm{E_{vis}} < 0.5$;
6. Acoplanarity angle of the vectorial sums of the transverse momenta of the particles belonging to each hemisphere, $\theta_A > 45°$.

Dominant backgrounds in this channel were from multi-hadron and $(e\overline{e})q\overline{q}$ processes and were removed by cuts (4) and (5). The real data and simulated background by the LUND Monte Calro were shown in the fig.35 before the visible energy and the acoplanarity angle cut. It showed a good agreement between the data and simulation. With these cuts, the efficiency to detect chargino pairs decaying into $q\overline{q}\,\tilde{\gamma}$ was 0.24 when $(m_{\tilde{\chi}}, m_{\tilde{\gamma}}) = (25,0)$ GeV. We expected 1.3 events from these backgrounds in the search region. One event survived in the search region which was kept as a candidate.

6.4 Chargino mass limit

In the analysis described above, we observed two events after the cuts, i.e, one acoplanar tau pair and one acoplanar jet candidate. Because the estimated backgrounds for all modes amount to 3.7 events, the fact that two events survived agrees with the background estimation. When we calculate the lower mass limit for the chargino, we kept these two events as candidates.

Detection Efficiency

The efficiencies for the chargino decay are summarized in table.3 in the case of $m_{\tilde{\gamma}} = 0$ and $m_{\tilde{\chi}} = 25\ GeV$. The error of the efficiencies were estimated by the statistical error of the simulation which are shown in table.3. Typical error of the efficiency were about 1 %. The efficiency depends on the mass of the chargino. It growth higher when the chargino mass becomes heavy since the the chargino decay was more acoplanar for the higher mass. Hence, in order to give the conservative results, we fixed the efficiency at the $m_{\tilde{\chi}} = 25GeV$ and estimated the number of events expected for the higher mass.

Limit calculation

Because the branching fractions into the four modes studied are model-dependent, we show the mass limit as a function of leptonic branching ratio in two cases: equal branching ratio to each leptonic mode; and leptonic branching ratios that minimize overall acceptance ϵ_{tot} as follows.

$$\epsilon_{tot}(B_L) = Min\Big(\sum_l \epsilon_{l\bar{l}} B_l^2\Big) + \epsilon_{jets}\Big(1 - B_L\Big)^2$$

with the constraint of

$$\sum_l B_l = B_L$$

where $\epsilon_{l\bar{l}}$ are the individual acceptance.
Then total acceptance is expressed as;

$$\epsilon_{tot}(B_L) = \epsilon_L B_L^2 + \epsilon_{jets}\Big(1 - B_L\Big)^2$$

where

$$\epsilon_L = \frac{1}{\sum_l \frac{1}{\epsilon_l}}$$

The mass limit was derived as the following;

$$\sum_{exp}[\sigma(E_{beam})\epsilon_{tot}(B_L)] = N_{95\%CL}(N'_{obs})$$

where summation runs over experimental conditions differing in the beam energy or the trigger condition.

The right hand side of the equation means 95% confidence level (CL) upper limit corresponding to observed N'_{obs} events. The integrated luminosity was obtained by the ECL as mentioned in chapter 5 and summarized in table.3. In the limit calculation, the errors of the integrated luminosity and of the efficiencies were not taken into accounts since their contribution to the limit calculation was negligible small. In our case $N_{95\%CL}$ was 6.3, since we observed 2 events. Figs.36(a) and (b) summarize the result as functions of B_L together with previous limits from the experimental groups at PETRA[37 ,38] for $m_{\tilde{\gamma}} = 0$ and $m_{\tilde{\gamma}} = 10$ GeV, respectively. Notice that the region below the chargino mass of 20 GeV is not shown in the figures, since our data did not improve the previous upper limits for the mass of light charginos. For $m_{\tilde{\gamma}} = 0$, charginos with $m_{\tilde{\chi}} = 25.5$ GeV or less were excluded at the 95 % CL regardless of their leptonic branching ratios. The mass limit was most stringent if the leptonic branching fraction: $B_L = 0$. In this case $m_{\tilde{\chi}} > 27.8$ GeV.

6.5 Search for charged scalar leptons

Charged scalar leptons can be pair-produced when their mass is below the energy threshold. Since they decay into a photino and a corresponding charged lepton, their signature is similar to that of charginos. The Production cross-section was estimated in chapter 3. Therefore the results found while searching for acoplanar lepton pairs from the decay of charginos can be used to set mass limits to the charged scalar leptons.

Scalar electrons

If the LSP is the photino , pair-produced scalar electrons promptly decay in to electrons and photinos. In this case the results of acoplanar electron pair search in the chargino case can be used. The only difference from the chargino case lies in their production cross section described in chapter 3. We therefore estimated the cross-section by e.qs. (3.2) and (3.3). The presence of the t-channel diagram prevented us from using Berends-Kleiss prescription for initial state radiative correction. The scalar electron limit we show below is optimistic in this respect. The scalar electron, if not the LSP, decays into $e\,\tilde{\gamma}$ and leaves a similar signature to the $e\bar{\nu}\,\tilde{\gamma}$ decay of the chargino. If the scalar electron itself is the LSP, it is stable and expected to behave as a heavily ionizing particle detectable by the TPC through dE/dx measurement[41] . Figs.37(a) and (b) show our 95% CL lower mass limits with the previous results from

PEP/PETRA[37,11] for $m_{\tilde{e}_R} = m_{\tilde{e}_L}$ and $m_{\tilde{e}_R} << m_{\tilde{e}_L}$, respectively. In the former case we have explored and excluded the high $m_{\tilde{e}}$ high $m_{\tilde{\gamma}}$ region up to a scalar electron mass of about 28. GeV. The stable scalar electron mass limit depends on the photino mass because of the t-channel diagram.

Scalar muons

If scalar muons are the LSP, they can be detected by dE/dx measurement as is the case of any charged LSP. If the LSP is the photino, they decay into $\mu\,\tilde{\gamma}$, resulting in acoplanar $\mu\bar{\mu}$ pairs. The signature is similar to the $\mu\bar{\nu}\,\tilde{\gamma}$ decay of the chargino. Thus we can derive the scalar muon mass limit from the search result we described above. The efficiency for this process was better than the chargino case mainly because $\tilde{\mu}$ decays into 2-body final states resulting in higher momentum muons, while $\tilde{\chi}$ decays into 3-body final states: the efficiency was $\epsilon = 0.30$ at 55 GeV (the phase-II TPC trigger) when $(m_{\tilde{\mu}}, m_{\tilde{\gamma}}) = (22,0)$ GeV. The efficiency started dropping quickly when the $\tilde{\mu}$-$\tilde{\gamma}$ mass difference approached 6 GeV. The 95 % CL limit obtained from this search is shown in figs.38(a) for $m_{\tilde{\mu}_R} = m_{\tilde{\mu}_L}$ and (b) for $m_{\tilde{\mu}_R} << m_{\tilde{\mu}_L}$, together with the previous limit by PETRA experiments[37,39] . The lower mass limit to $\tilde{\mu}$ for $m_{\tilde{\gamma}} = 0$ GeV was 24.5 GeV in the first case.

Scalar taus

The mass limit found for stable scalar muons can be applied directly to the case of stable scalar taus, since their production cross-sections are the same as long as their masses are the same. If the LSP is the photino, the scalar taus decay into a photino and a tau and their pair production can be detected as acoplanar $\tau\bar{\tau}$ pairs similar in event topology to the pair-produced charginos decaying into $\tau\bar{\nu}\,\tilde{\gamma}$. Therefore the mass limit can be obtained from the results of the charginos decay into an acoplanar τ-pair. The candidate event observed in that search was again included here as a scalar tau pair candidate in setting the mass limit. As with the acoplanar muon search, the efficiency to detect scalar taus was better than that of the chargino case: $\epsilon = 0.14$ at 55 GeV when $(m_{\tilde{\tau}}, m_{\tilde{\gamma}}) = (20,0)$ GeV which dropped rapidly when the $\tilde{\mu}$ - $\tilde{\gamma}$ mass difference approached 6 GeV. Fig.39 shows the 95 % CL limit obtained from this search together with the previous limit by PETRA experiments[37] . The lower mass limit to $\tilde{\tau}$ for $m_{\tilde{\gamma}} = 0$ GeV was 21.7 GeV when $m_{\tilde{\tau}_R} = m_{\tilde{\tau}_L}$.

6.6 Search for scalar quarks

For scalar quark pair production, we assumed a threshold behavior governed by the $\beta^3/4$ factor, without considering resonance structures. Because of our limited statistics, we concentrated on the scalar quarks with a charge of 2/3 in units of the proton charge (Q=2/3). The scalar quarks decay through the following mode: $\tilde{q} \rightarrow q\,\tilde{\gamma}$ when the LSP is the photino. An event resulting from this decay is characterized by two jets with a large acoplanarity angle. We searched for events with such signatures by requiring each event to pass the following cuts:

1. More than four tracks with $p_t > 0.15$ GeV and $|\cos\theta| < 0.83$ originating from the interaction point.
2. Total visible energy > 10 GeV.
3. $|\cos\theta_{sphericity\ axis}| < 0.8$.
4. Two jets defined by the JADE cluster algorithm[40] with $y_{cut} = 0.04$.
5. Acoplanarity angle of the two jets, $\theta_A > 50°$.

The detection efficiency for the $\tilde{q}$-pair production was more than 0.4 for a scalar quark mass > 23 GeV and a photino mass < 10 GeV but rapidly decreased to zero as the $m_{\tilde{q}}$-$m_{\tilde{\gamma}}$ mass difference becomes less than 8 GeV. In the Monte Carlo simulation, hadronization was assumed to precede the scalar quark decay. The subsequent decay of the leading R-hadron containing the scalar quark was treated using the spectator model with the LUND string fragmentation. Possible background sources include multi-hadrons, $(e\bar{e})q\bar{q}$, $(e\bar{e})\tau\bar{\tau}$, and $\tau\bar{\tau}$. The total background contamination from these channels amounts to 0.93 events in the search region. No events were observed in the search region. The lower limits to the scalar quark mass are calculated as a function of the photino mass and tabulated in table 4. The lower mass limit to $Q = 2/3$ scalar quarks was 26.3 GeV, when $m_{\tilde{q}_R} = m_{\tilde{q}_L}$. As for light squarks, our data did not improve the previous upper mass limits from PETRA experiments[37,38].

6.7 Summary of the Search

In this experiment, we did not observe the production of the charged SUSY particles, then extended their lower mass limits as follows.

When $m_{\tilde{\gamma}} = 0$;

$$m_{\tilde{\chi}} > \begin{cases} 25.9 & \text{GeV } Br_{lepton} = 1 \\ 27.8 & \text{GeV } Br_{lepton} = 0 \end{cases}$$

$$m_{\tilde{e}} > \begin{cases} 27.4 & \text{GeV } m_R = m_L \\ 26.9 & \text{GeV } m_R << m_L \end{cases}$$

$$m_{\tilde{\mu}} > \begin{cases} 24.5 & \text{GeV } m_R = m_L \\ 22.7 & \text{GeV } m_R << m_L \end{cases}$$

$$m_{\tilde{\tau}} > \{ 21.7 \quad \text{GeV } m_R = m_L$$

$$m_{\tilde{q}} > \begin{cases} 26.3 & \text{GeV } m_R = m_L \quad \text{Q=2/3} \\ 24.4 & \text{GeV } m_R << m_L \quad \text{Q=2/3} \end{cases}$$

or when $m_{\tilde{\gamma}} = 10$ GeV;

$$m_{\tilde{\chi}} > \begin{cases} 25.8 & \text{GeV } Br_{lepton} = 1 \\ 27.8 & \text{GeV } Br_{lepton} = 0 \end{cases} \quad \begin{matrix} \text{(assume equal branching} \\ \text{ratio for three leptons)} \end{matrix}$$

$$m_{\tilde{e}} > \begin{cases} 28.2 & \text{GeV } m_R = m_L \\ 26.2 & \text{GeV } m_R << m_L \end{cases}$$

$$m_{\tilde{\mu}} > \begin{cases} 24.4 & \text{GeV } m_R = m_L \\ 22.7 & \text{GeV } m_R << m_L \end{cases}$$

$$m_{\tilde{\tau}} > \{ 20.6 \quad \text{GeV } m_R = m_L$$

$$m_{\tilde{q}} > \begin{cases} 26.2 & \text{GeV } m_R = m_L \quad \text{Q=2/3} \\ 24.2 & \text{GeV } m_R << m_L \quad \text{Q=2/3} \end{cases}$$

where all limits are given at the 95 % CL.

7. Constraint on the SUSY parameters

In this chapter, we derive constraints on the SUSY parameters form the mass limit of $\tilde{\chi}$ and $\tilde{f}$'s with in the frame work of the minimal N=1 supergravity(SUGRA) GUT. In this model the masses of the particles can be written in term of the four parameters; m_0, M_2, μ, and v_1/v_2.
m_0 is the common scalar mass at the SUSY mass scale, M_2 the SU(2) gaugino mass, μ the higgsino mixing term, and v_1/v_2 the ratio of the vacuum expectation value of the two higgs doublets, respectively. The mean of these parameters are described in appendix B.

7.1 Gaugino mass

The charginos are the mixed states of the wino and the charged higgsino obtained by diagonalizing the term[9] ;

$$(\overline{\lambda}_- \quad \overline{\chi}_-)\begin{pmatrix} M_2 & gv_2 \\ gv_1 & 2\mu \end{pmatrix} P_L \begin{pmatrix} \lambda_- \\ \chi_- \end{pmatrix} \tag{7.1}$$

where

$$\lambda_- \equiv \frac{1}{\sqrt{2}}(\lambda_1 + i\lambda_2), \quad \chi_- \equiv P_L h_2 - P_R h1$$

h_i : charged higgsino field
λ_i : charged gaugino field.

The neutral sector is more complicated since the neutralino are the mixed states of two neutral higgsinos h_1^0 and h_2^0, and two neutral gauginos λ_3 and λ_0. The mass term to be diagonalized is;

$$\frac{1}{2}(\overline{h}_1^0 \quad \overline{h}_2^0 \quad \overline{\lambda}_3 \quad \overline{\lambda}_0)\begin{pmatrix} 0 & -2\mu & \frac{1}{\sqrt{2}}gv_1 & -\frac{1}{\sqrt{2}}g'v_1 \\ -2\mu & 0 & \frac{1}{\sqrt{2}}gv_2 & -\frac{1}{\sqrt{2}}g'v_2 \\ \frac{1}{\sqrt{2}}gv_1 & -\frac{1}{\sqrt{2}}gv_2 & M_2 & 0 \\ \frac{1}{\sqrt{2}}g'v_1 & -\frac{1}{\sqrt{2}}g'v_2 & 0 & M_1 \end{pmatrix}\begin{pmatrix} h_1^0 \\ h_2^0 \\ \lambda_3 \\ \lambda_0 \end{pmatrix} \tag{7.2}$$

In eqs.(7.1) and (7.2), μ is the higgsino mixing, M_1 and M_2 are the soft-SUSY breaking $SU(2)_L$ and $U(1)_Y$ gaugino masses and v_1 and v_2 are the vacuum expectation values of the higgs doublets.

The masses of charged and neutral gauginos are obtained by diagonalization of the mass matrices. For the charged sector, two mass eigen states are obtained from eq.(7.1)as follows;

$$\begin{aligned} m_{\tilde{\chi}_\pm} =& \frac{1}{2}[M_2^2 + 4\mu^2 + 2m_w^2 \\ & \pm \sqrt{(M_2^2 - 4\mu^2)^2 + 4m_w^2 cos^2\theta_v + 4m_w^2(M_2^2 + 4\mu^2 + 4M_2\mu sin^2 2\theta_v)}] \end{aligned} \tag{7.3}$$

where $tan\theta = v_1/v_2$. Notice that one of the charginos has the mass below m_w.

The neutral sector is difficult to diagonalize in general case. If $M_1 = M_2 = 0$, the matrix is simplified and a massless photino is obtained. The other states are two zinos and higgsinos. The masses of the gauginos are;

$$\mu_\pm = \sqrt{\mu^2 + m_z^2} \pm \mu.$$

If the parameter M_i's are not zero but small, they can be treated as perturbation. Then the photino can be massive and the gaugino mass is differ from $\mu_\pm$. The masses of the photino and the two gauginos are expressed as;

$$\begin{aligned} m_{\tilde{\gamma}} &= |M_2 sin^2\theta_w + M_1 cos^2\theta_w| \\ m_{\tilde{Z}_-} &= \mu_- + \frac{\mu_+}{\mu_+ + \mu_-}|M_2 cos^2\theta_w + M_1 sin^2\theta_w| \\ m_{\tilde{Z}_+} &= \mu_+ - \frac{\mu_-}{\mu_+ + \mu_-}|M_2 cos^2\theta_w + M_1 sin^2\theta_w| \end{aligned} \tag{7.4}$$

We use this formula for the photino mass since our analysis assumes $m_{\tilde{\gamma}} < 10$ GeV. At the GUT scale the gaugino masses of SU(3),SU(2) and U(1) (and coupling constants) are equal and ;

$$\frac{\alpha_3}{M_3} = \frac{\alpha_2}{M_2} = \frac{\alpha_1}{M_1} \tag{7.5}$$

is valid at any energy scale. Therefore

$$\frac{M_1}{M_2}(m_w) = \frac{\alpha_1}{\alpha_2}(m_w) = \frac{5g'^2}{3g_2^2} = \frac{5}{3}tan^2\theta_w. \tag{7.6}$$

With this assumption the gaugino mass formula can be simplified and the gaugino mass is expressed as a function of the three parameters; M_2, μ and v_1/v_2.

7.2 Scalar mass

The scalar masses are derived by evolving them from unification scale to $\sim 100GeV$ by the renormalization group equation (RGE). Assuming common scalar mass, m_0, at the unification scale and three generations, the scalar masses are given by[42] ;

$$
\begin{aligned}
m^2(\tilde{d}_L) &= m_0^2 + 30.2m_{\tilde{\gamma}}^2 + 0.43rm_z^2 \\
m^2(\tilde{d}_R) &= m_0^2 + 28.4m_{\tilde{\gamma}}^2 + 0.07rm_z^2 \\
m^2(\tilde{u}_L) &= m_0^2 + 30.2m_{\tilde{\gamma}}^2 - 0.36rm_z^2 \\
m^2(\tilde{u}_R) &= m_0^2 + 28.4m_{\tilde{\gamma}}^2 + 0.14rm_z^2 \\
m^2(\tilde{e}_L) &= m_0^2 + 2.2m_{\tilde{\gamma}}^2 + 0.28rm_z^2 \\
m^2(\tilde{e}_R) &= m_0^2 + 0.6m_{\tilde{\gamma}}^2 + 0.22rm_z^2 \\
m^2(\tilde{\nu}) &= m_0^2 + 2.2m_{\tilde{\gamma}}^2 - 0.50rm_z^2
\end{aligned}
\tag{7.7}
$$

where r = $cos2\theta_v$.

Actually, the scalar leptons are the mixed states of the left- and the right-handed superpartners and resulting the diagonalization of the following mass term;

$$
(\tilde{l}_L \quad \tilde{l}_R)\begin{pmatrix} L^2m_0^2 + m_l^2 & Am_0m_l \\ Am_0m_l & R^2m_0^2 + m_l^2 \end{pmatrix}\begin{pmatrix} \tilde{l}_L \\ \tilde{l}_R \end{pmatrix} \tag{7.8}
$$

where m_0 is common scalar mass, L, A, and R are dimensionless constants depending on the soft SUSY breaking term, and m_l is the mass of the corresponding ordinary particle. Although the mixing is model dependent in general, when $m_l << m_0$, unless L=R to a high degree of precision, the left-handed and the right-handed partners are approximately mass eigen states. Therefore in this analysis we treated the left- and right-handed partners as the mass eigen states.

7.3 Results

From the results of the last section, the masses of the gaugino and the scalar

expressed in term of the four parameter of the SUSY, i,e,

$$
\begin{aligned}
m_{\tilde{\chi}^{\pm}} &= F(\mu, M_2, v_1/v_2) \\
m_{\tilde{e}} &= F'(m_0, m_{\tilde{\gamma}}, v_1/v_2) \\
m_{\tilde{Z}_{\pm}} &= G'(M_2, \mu) \\
m_{\tilde{\gamma}} &= G''(M_2)
\end{aligned}
$$

The constraints used for this analysis are the lower mass limits obtained in chapter 6 together with the previous experiments;

$$
\begin{aligned}
& m_{\tilde{\chi}} > 25.5 GeV \\
& m_{\tilde{e}} > \begin{cases} > 47. & \text{GeV for } m_{\tilde{\gamma}} = 0 \text{ (from ASP)} \\ > 26.5 & \text{GeV for } m_{\tilde{\gamma}} = 10 \text{ (from our data)} \end{cases} \\
& m_{\tilde{f}} < 1000. GeV
\end{aligned}
$$

The last condition was the requirement to resolve the naturalness problem.

Since our mass limits are functions of the photino mass, we consider, as representative case, the constraints on the parameter space in the case $m_{\tilde{\gamma}} = 0$ and 10 GeV (corresponding to M_2 is 0 and 16.8 GeV, respectively). For simplicity we further assume $m_L >> m_R$ for the scalar partners.
Fig.40 shows the allowed region in the v_1/v_2 and μ plane for $m_{\tilde{\gamma}}$ is 0 (a) and 10 GeV (b) respectively. The allowed region is summarized as;

$$
\begin{cases} 0.3 < v_1/v_2 < 4 & m_{\tilde{\gamma}} = 0 \\ 0.3 < v_1/v_2 < 6 & m_{\tilde{\gamma}} = 10 \text{ GeV} \end{cases}
$$

$$
\begin{cases} -200 < \mu < 200 & m_{\tilde{\gamma}} = 0 \\ -50 < \mu < 750 & m_{\tilde{\gamma}} = 10 \text{ GeV} \end{cases}
$$

and the common scalar mass (m_0) was greater than 40 GeV.

From the constraints obtained for the SUSY parameters ,on the contrary, we can restrict possible masses of the SUSY particles. Since the constraints are more tight on the higgsino mixing term (μ) than on the common scalar mass (m_0), our result is more imformative for the gaugino sector, i.e, the neutral gauginos.

The neutral gaugino mass is plotted in figs.41 and 42 for Z^- and Z^+, respectively. As a result, the zions could exist in the mass range

$$20 \text{ GeV} < m_{\tilde{z}_-} < 200 \text{ GeV}$$
$$30 \text{ GeV} < m_{\tilde{z}_+} < 750 \text{ GeV}$$

if $m_{\tilde{\gamma}} < 10$ GeV.

8. Conclusion

We have made a extensive search for pair productions of supersymmetric particles in e^+e^- annihilation using the data at $\sqrt{s} = 52 \sim 57$ GeV by the TOPAZ detector at TRISTAN. Since we observed no evidence for the production of such particles, the mass limits obtained at PEP/PETRA are now extended as follows:

$$
\begin{aligned}
m_{\tilde{\chi}} &> \{ 25.9\ GeV \quad Br_{lepton} = 1 \\
m_{\tilde{e}} &> \begin{cases} 27.4\ GeV & m_R = m_L \\ 26.9\ GeV & m_R << m_L \end{cases} \\
m_{\tilde{\mu}} &> \begin{cases} 24.5\ GeV & m_R = m_L \\ 22.7\ GeV & m_R << m_L \end{cases} \\
m_{\tilde{\tau}} &> \{ 21.7\ GeV \quad m_R = m_L \\
m_{\tilde{q}} &> \{ 26.3\ GeV \quad m_R = m_L \ \mathrm{Q{=}2/3}
\end{aligned}
$$

where all limits are given at the 95 % CL and in the case of $m_{\tilde{\gamma}} = 0$.

Using the obtained limits together with those from the previous experiments, the parameters of the minimal N=1 supergravity GUT were restricted. The results are to be used in model building or selection.

APPENDIX A

Motivation of the SUSY

The standard model is a gauge theory based on the symmetry group $SU(3) \otimes SU(2)_L \otimes U(1)_Y$ where the $SU(2)_L \otimes U(1)_Y$ is spontaneously broken to $U(1)_{em}$ at the energy scale of $O(100GeV)$ by the non-zero vacuum expectation value of the Higgs field. The fundamental particles of the model are listed in table.5. There are three generations of left-handed ($SU(2)$ doublet) and right-handed ($SU(2)$ singlet) quarks/leptons, gauge vector bosons (g, $W^{\pm}$, Z^0, γ) as the carrier of the interacting force, a Higgs scalar which is a relic of the spontaneous symmetry breaking giving the mass to the $W^{\pm}$, Z^0, quarks, and leptons.

Although there are no experimental results conflicting with the model, it is not considered as the ultimate theory of elementary particles. There are many reasons for this and some are listed below.

1. There are three independent coupling constants, g_3 for $SU(3)$, g_2 for $SU(2)_L$, and g' for $U(1)_Y$, implying that the three kinds of interactions are not unified.
2. Gravity is not taken into account at all and left ununified.
3. The number of generations of the fundamental fermions is unexplained.
4. There is no builtin mechanism for electric charge quantization. In the $SU(2)_L \otimes U(1)_Y$ sector, the U(1) hypercharge and also electric charge can be any real number.
5. The masses of the fermions are determined by their Yukawa coupling to the Higgs field but the coupling constants are input parameters.

These problems strongly suggest that the standard model should be an effective theory to be derived from the underlying unified theory at high energy scale.
In general, the behaviour of the coupling constants is governed by the renormalization group equation (RGE)[4] . If the behaviours of the coupling constants are calculated by the RGE, one finds that three coupling constants merges almost a single value at the energy scale of $10^{14\sim17}$ GeV. This fact strongly suggests the unification of strong and electroweak force (GUT).

Once we assume the unification, the naturalness problem arise as explained below. The loop correction to the Higgs mass shown in fig.43 (a) contributes as;

$$\int_{\mu 1}^{\mu 2} \frac{dk^4}{k^2 - m} \simeq \mu_2^2 - \mu_1^2 \tag{A1}$$

where m is a mass of the particle in the loop. Therefore, the relation between Higgs mass at the the energy scale $\mu_1 = m_w$ and the unification scale μ_2 is expressed schematically in the form[14] ;

$$m_H^2(m_W) \simeq m_H^2(\mu_2) + Cg\mu_2^2 \tag{A2}$$

where g is a coupling constant and C is a dimensionless constant. The eq.(A 2) indicates that if we assume the μ_2 of $O(10^{15}\ GeV)$, the right hand of the eq.(A 2) must be canceled at the accuracy of 10^{-26} to keep the Higgs mass $m_H(m_W)$ at $O(10^2\ GeV)$. It is very unnatural and is called the naturalness problem.

There are two ways out from the naturalness problem. The first is to replace the elementary Higgs by composite field as in the technicolour theories[5] and cut off the integration at $\mu_2 \sim O(1TeV)$. The second is to introduce the supersymmetry (SUSY) which transforms fermions to bosons and vice versa. In the supersymmetric theory, contributions from supersymmetric partners are add to eq.(A 1) with opposite sign as illustrated in fig.43 (b) and exactly cancel the quadratic divergence, i.e, the SUSY guarantees the factor $C = 0$ in eq.(A 2).
The supersymmetry must be broken since we do not knew any particles which are mass degenerate with conventional particles but have a spin of 1/2 different. In this case we have;

$$m(m_w)^2 \simeq m(\mu_2)^2 + C'|m - \tilde{m}\ |^2.$$

where m and $\tilde{m}$ are masses of ordinary and its supersymmetric partners, respectively. If $|m - \tilde{m}\ | < O(1\ TeV)$, the theory is still natural. In other word, if the SUSY is the solution, superpartners must exist blow $O(1\ TeV)$.

The other motivation of the SUSY arises from the unification of gravity. Coleman and Mandula have shown[15] that in the Lorentz tensors, the generators of the Poincaré group, P^μ, $M^{\mu\nu}$, and the Lorentz invariant generators of the internal symmetry,Q_i,

are the only possible conserved numbers in a theory with nonzero S matrix in four-dimensions. The generators Q_i form Lie algebra as;

$$[Q_a, Q_b] = if_{abc}Q_c$$

and commute with Poincaré generators;

$$[P^\mu, Q_i] = [M^{\mu\nu}, Q_i] = 0$$

This means that external and internal symmetry cannot be unified. The way out from this no-go theorem is to give the fermionic charge to the Q_i and extends the Lie algebra to the graded Lie algebra which include both commutation and anticommutation relations. Now we denote Q_a as a left-handed Weyl spinor and $\overline{Q}_{\dot{b}}$ as a right-handed Weyl spinor. Since Q_is are conserved charges of spin 1/2, their anticommutator $\{Q_a, \overline{Q}_{\dot{b}}\}$ is also conserved and must be spin 1 vector. The Coleman Mandula theorem permit the conserved vector, i.e, P^μ. The supersymmetry is defined by the algebra;

$$[Q_a, P^\mu] = 0$$
$$\{Q_a, \overline{Q}_{\dot{b}}\} = 2\sigma^\mu_{a\dot{b}}P_\mu$$

It indicates that the SUSY transformation is related with space-time. Indeed the SUSY must include gravity if we make it a local symmetry. Haag, Lopuszanski, and Sohnius[16] have shown that the SUSY algebras are the only graded Lie algebra which are consistent with relativistic quantum field theory.

APPENDIX B

Parameters in the mass matrix

In the minimal N=1 supergravity model, the SUSY is broken by gauge singlet soft supersymmetry breaking terms via gravity. This mechanism is an analogy of the higgs mechanism in the electroweak theory and called the super higgs mechanism. In this case the massless gravitino (spin 3/2 superpartner of the graviton) becomes massive combined with the Goldstone fermion (goldstino). This gravitational sector (called hidden sector) communicates with the ordinary sector only via gravity and allows the scalar and the gaugino mass terms in the gauge invariant form; i.e, soft SUSY breaking terms. Since the superhiggs mechanism has model dependence and hence introduces parameters in the soft SUSY breaking term. The actual form of this term is;

$$M_4 ReA^2 + M_3 ImA^2 + c(A^3 + h.c) + M_a(\lambda^a\lambda^a + \overline{\lambda}^a\overline{\lambda}^a) \tag{B1}$$

where λ is the superpartner of the gauge boson(gaugino) and and A is the complex scalar field. M_is are the parameters; M_4 splits the mass of A and its partner, M_3 splits masses of two fields if A is expressed in terms of two real spinless fields, M_as $(a = 1, 2, 3)$ are the Majorana mass term of the gauginos corresponding to the gauge groups.

In order to obtain a low energy effective model, the $SU(2)_L \otimes U(1)_Y$ must be broken. It is done by the radiative correction to the scalar mass. The evolution of the scalar mass is determined by the RGE as;

$$\mu\frac{\partial m^2_{scalar}}{\partial \mu} = M_m m^2_{scalar}$$

where M_m is a matrix. The behavior of the Higgs and the scalar fermions is illustrated in the fig.44. All scalars have the same mass, m_0, at the unification scale but the only Higgs mass became negative and breaks $SU(2)_L \otimes U(1)_Y$ at the energy scale of $O(m_w)$. It is possible by assuming a large top quark mass since only the Higgs field has the

Yukawa coupling to the top quark. Its contribution is

$$\mu\frac{\partial m_H^2}{\mu} = + g_{Ht\bar{t}}^2 m_t - g_a^2 M_a$$

where $g_{Ht\bar{t}}^2$ is Yukawa coupling constant of the top and g_a^2s and M_as are couplings and masses of the gauginos. It is found that large $g_{Ht\bar{t}}^2$ drives the higgs mass to negative and breaks the $SU(2)_L \otimes U(1)_Y$.

The low energy minimal model containing the particle in table.1 is completed if a superpotential is given. The most general form is;

$$W = f_l H_1 \tilde{L}\tilde{R} + f_d H_1 \tilde{Q}\tilde{D} + f_u H_1 \tilde{Q}\tilde{U} + \mu H_1 H_2$$

where

$$\tilde{Q} = \begin{pmatrix} \tilde{u}_L \\ \tilde{d}_L \end{pmatrix}$$
$$\tilde{L} = \begin{pmatrix} \tilde{\nu}_L \\ \tilde{e}_L \end{pmatrix}$$
$$\tilde{U} = \tilde{u}_R^*$$
$$\tilde{D} = \tilde{d}_R^*$$
$$\tilde{R} = \tilde{e}_R^*$$

Corresponding to the existence of the two Higgs doublets, two vacuum expectation values (actually their ratio) and the mixing parameter μ is parameters of the model.

Now we can express the masses of the SUSY particles in terms of the parameter of the minimal N=1 SUGRA model as is presented in chapter 7. The possible charged gaugino mass terms are in the form;

$$\frac{ig}{\sqrt{(2)}}[v_1\lambda^+ h_1 + v_2\lambda - +h_2] + M_2\lambda^+\lambda^- - \mu h_1 h_2 + h.c$$

The terms in the bracket arise from the scalar-gaugino-higgsino interaction term, the second is a contribution from the soft SUSY breaking term and the last is from the superpotential and called the higgsino mixing term.

For the neutral sector, which are complicated since the photino, the zino, and the two neutral higgsinos can be mixed, we have;

$$\frac{1}{2}ig\lambda_3(v_1h_1^0 - v_2h_2^0) - \frac{1}{2}ig'\lambda_0(v_1h_1^0 - v_2h_2^0) + \frac{1}{2}M_2\lambda_3\lambda_3 + \frac{1}{2}M_1\lambda_0\lambda_0 + \mu h_1^0h_2^0 + h.c$$

Each term is similar to that of the charged sector but the gaugino and the higgsino fields are corresponding neutral ones. The form of the mass matrix is given in chapter 7. As a result the gaugino mass is expressed as a function of $(\mu, M_i, v_1/v_2)$. The more detailed description can be found in refs. 8 and 9.

APPENDIX C

The TOPAZ End Cap Calorimeter

The TOPAZ End Cap Calorimeter was a gas sampling electromagnetic calorimeter located in the end cap region of the TOPAZ detector as shown in fig.6. It was a sandwich of absorber plates and proportional counter arrays as shown in fig.45 and the number of sampling layers was 34. In each layer, a proportional tube array consisted of 196 tubes was glued on a printed circuit (PC) board, and the board was also glued to a lead plate of $2mm$ or $3mm$ thick backed by $1mm$ thick stainless steel (SUS) plates on both sides. The thickness of lead absorbers were $2mm$ for the first 20 layers and $3mm$ for the remaining 14 layers, respectively which were equivalent to 0.46 and 0.64 radiation length (X_0), including SUS backing, and the total depth of the detector was 18.2 X_0. Proportional tubes were made of conductive plastic[43] , and the dimension of cross section was $5mm$ wide, $10mm$ high and $1mm$ thick. The anode wire, gold plated tungsten of $50\mu m$ diameter, was strung with a tension of $200gw$. Positive high voltage was applied to the anode, while the plastic tube was grounded at an end by a copper tape.

The signal from the calorimeter was read by the cathode pads printed on the PC board. Thanks to the high resistance of the plastic tubes, the electric field of the proportional counter formed by the DC high voltage applied between the tube and the anode wire while the RF signals were induced on the cathode pad placed out side of the plastic tube as shown in fig.46. Cathode pads were ganged together to form a tower structure toward the interaction point and each tower was divided into three segments, corresponding to 8, 12 and 14 layers.

The signal from the calorimeter, converted to the differential pulse by a pulse transformer, directly drove the $40m$ long twisted pair cable and fed into a differential amplifier to suppress the common mode noise induced in the cable. The amplifier output two signals, one was sent to the analog-digital to converter(ADC) and recorded as the calorimetric information, the other is used for the trigger information.

For the trigger, 16 the signal was linearly summed by a analog summation module called basic sum, then, they are again summed by a similar module called general sum,

and finally information of partial energy sums and two total energy sum are created as mentioned in chapter 4.

Since the gain of the proportional counter depends on the pressure and the temperature of the counter gas, the correction of these variation is essential to obtain good resolution. These dependence was studied by the prototype and it was shown that the correction was very useful[21,24] . Fig.47-(a) shows the variation of the pulse height of the ECL for Bhabha events with the correction factor obtained from corresponding gas pressure and tempErature. The pulse height distribution before and after the correction is shown fig.47-(b) which shows the improvement of the resolution efficiently.

REFERENCES

1. G. D. Politzer, *Phys. Rev. Lett.* **30**(1973)1346; D. J. Gross and F. Wilczek, *Phys. Rev. Lett.* **30**(1973)123.

2. S. Weinberg,*Phys. Rev. Lett.* **19**(1967)1264; A.Salam, Proc. Eight Nobel Symp, ed. by N. Svartholm 1968; S. L Glashow, Nucl.Phys **22** (1961)579.

3. G. Arnoson *et al.*, *Phys. Lett.* **122B**(1983)103; G. Arnoson *et al.*, *Phys. Lett.* **126B**(1983)398; M. Banner *et al.*, *Phys. Lett.* **122B**(1983)476; M. Bagnaia *et al.*, *Phys. Lett.* **129B**(1983)130.

4. See for example, L.H. Ryder, Quantum Field Theory Cambridge University Press (1985).

5. S. Weinberg, *Phys. Rev.* **D13**(1976)974;
   S. Weinberg, *Phys. Rev.* **D19**(1979)1277;
   L. Susskind, *Phys. Rev.* **D20**(1979)2619;
   E. Farhi and L. Susskind Phys. Rep. **74**(1981)277.

6. P. Fayet and S. Ferrara, Phys. Rep. **32**(1977)249.

7. Arnowitt *et al.*, Applied N = 1 Supergravity, (World Scientific (1983))

8. H. P. Nilles, Phys. Rep. **110**(1984)1

9. H. E. Haber and G. L. Kane, Phys. Rep. **117**(1985)75.

10. A. Savoy-Navarro, Phys. Rep. **105**(1984)91; M. Davier, Proceedings of XXIII International Conference on High Energy Physics, Berkeley, edited by S. C. Loken, p.25; K. Hagiwara and S. Komamiya, KEK Preprint 86-95, January 1987; S. L. Wu, Proceedings of 1987 International Symposium on Lepton and Photon Interactions at High Energies, Humburg, edited by W. Bartel and R. Ruckl, p.39; J. Ellis and F. Pauss, CERN TH.4992/88,March 1988.

11. C. Hearty *et al.*,*Phys. Rev. Lett.* **58**(1987)1711.

12. R. Ansari *et al.*, *Phys. Lett.* **195B**(1987)613.

13. C. Albajar *et al.*, *Phys. Lett.* **198B**(1987)261.

14. C.H. Liewellyn Smith and G.G. Ross, *Phys. Lett.* **105B**(1981)38.

15. S. Coleman and J. Mandula, *Phys. Rev.* **159**(1967)1251.

16. R. Hagg, J. Lopuszanski and M. Sohnius, *Nucl. Phys.* **B88**(1975)257.

17. F.A.Berends and R.Kleiss, *Nucl. Phys.* **B178**(1981)141.

18. T. Kobayashi and M. Kuroda, *Phys. Lett.* **134B**(1984)271.

19. T. Sjöstrand and M. Bengtsson, Comput. Phys. Commun. 43,(1987),367.

20. R. Hayano *et al.*, TRISTAN-EXP-002 (1983)

21. T. Takahashi, master thesis, Dept. of Physics Nagoya univ. (1987); S. Uno, master thesis, Dept. of Physics Nagoya univ. (1984); S. Uno, doctoral thesis, Dept. of Physics Nagoya univ. (1987); T. Tsukamoto, master thesis, Dept. of Physics Nagoya univ. (1984); T. Tsukamoto, doctoral thesis, Dept. of Physics Nagoya univ. (1987); S. Ueda, master thesis, Dept. of Physics Nagoya univ. (1986); Y. Masatani, master thesis, Dept. of Physics Nagoya univ. (1985); H. Takamure, master thesis, Dept. of Physics Nagoya univ. (1988)

22. T. Kamae et al., Nucl. Instr. and Meth. A252 (1986) 423 ; A. Shirahashi et al., UT-HE-87/4, October 1987

23. S. Kawabata et al., Nucl. Instr. and Meth. A270 (1988) 11

24. K. Fujii et al., Nucl. Instr. and Meth. A236 (1985) 55 ; J. Fujimoto et al., Nucl. Instr. and Meth. A256 (1987) 449

25. A. Imanishi et al., Nucl. Instr. and Meth. A269 (1988) 513

26. K. Fujii et al., Nucl. Instr. and Meth. A225 (1984) 23

27. T. Kishida et al., Nucl. Instr. and Meth. A254 (1987) 367

28. S. Noguchi et al., Submitted to Nucl. Instr. and Meth.

29. A. Yamamoto et al., Jpn. J. Appl. Phys. Letters 25 (1986) L440

30. R. Enomoto et al., Nucl. Instr. and Meth. A269 (1988) 507

31. U.S. NIM Committee, December 1983, DOE/ER-0189

32. K. Fujii et al., Nucl. Instr. and Meth. A264 (1988) 297

33. W. Nelson, H. Hirayama and D. Rogers, SLAC-Report-265 (1985)

34. H. Fesefeldt, PITHA 85/02 (1985)

35. S. Kuroda, Doctorial thesis Dept. of Physics Nagoya univ. (1987)

36. W. Bartel *et al.*, *Phys. Lett.* **152B**(1985)385.

37. H. -J. Behrend *et al.*,*Z. Phys.* **35C**(1987)181.

38. W. Bartel *et al.*, *Z. Phys.* **C29**(1985)505.

39. W. Bartel *et al.*, *Phys. Lett.* **152B**(1985)392.

40. W. Bartel *et al.*, *Z. Phys.* **C33**(1986)23.

41. I. Adachi *et al.*, in preparation; H. Kichimi, a talk given at VIII-th Physics in Collison conference.

42. H. Baer *et al.*, *Phys. Rev.* **35**(1987)1598.

43. Conductive plastic tubes used in this calorimeter are commercially available at Tokyo Printed Ink Mfg, Co Ltd; 2-7-15, Tabata-Shinano-machi, Kita-ku, Tokyo, Japan

TABLE CAPTIONS

1. The superpartners required for the minimal SUSY model with the conventional particles.
2. Previous SUSY searches.
3. The detection efficiency of the chargino decay for each decay mode when $m_{\tilde{\gamma}} = 0$ with experimental conditions. The trigger I,II indicated that the condition of the TPC trigger described in the chapter 3.
4. The lower mass limit of the scalar quark at the 95 % confidence level as a function of photino mass.
5. Fundamental particles of the standard model.

Table 1.

Convensional particles	Supersymmetric particles	
	weak eigen state	mass eigen state
ν	$\tilde{\nu}_{L,R}$	$\tilde{\nu}_{1,2}$
l	$\tilde{\nu}_{L,R}$	$\tilde{\nu}_{1,2}$
q	$\tilde{q}_{L,R}$	$\tilde{q}_{1,2}$
g	$\tilde{g}_{L,R}$	$\tilde{g}_{1,2}$
$W^{\pm}$	$\tilde{W}^{\pm}$	
H_1^+	$\tilde{H}_1^+$	$\tilde{\chi}^{\pm}$
H_2^-	$\tilde{H}_2^-$	
γ	$\tilde{\gamma}$	
Z^0	$\tilde{Z}^0$	
H_1^0	$\tilde{H}_1^0$	$\tilde{\chi}_i$
H_2^0	$\tilde{H}_2^0$	
H_3^0		

Table 2.

Spartile	Lower mass limit (GeV)	condition	group
$\tilde{\gamma}$	20.5	$\tilde{\gamma} \rightarrow \gamma \tilde{H}^0$	MARKJ
$\tilde{e}$	57.0(90%CL)	$m_L = m_R,\ m_{\tilde{\gamma}} = 0$	ASP
$\tilde{\mu}$	20.5	$m_L = m_R,\ m_{\tilde{\gamma}} = 0$	CELLO
$\tilde{\tau}$	20.5	$m_L = m_R,\ m_{\tilde{\gamma}} = 0$	CELLO
$\tilde{\chi} \pm$	20.5	$m_L = m_R,\ m_{\tilde{\gamma}} = 0$	CELLO
		$Br_{lepton} = 1.0$	
	40.0(90%CL)	$\tilde{\chi} \rightarrow \tilde{\nu} W$	UA2
$\tilde{\chi}^0$	35	$m_{\tilde{e}} < 70GeV,\ m_{\tilde{\gamma}} < 10GeV$	CELLO
$\tilde{q}_{L,R}$	21.4	$\tilde{q}_L = \tilde{q}_R,\ m_{\tilde{\gamma}} < 10$ GeV	JADE
		$\tilde{q} \rightarrow q \tilde{\gamma}$	
	45.0(90%CL)	$\tilde{q}_L = \tilde{q}_R,\ m_{\tilde{\gamma}} = 0$	UA1
		$m_{\tilde{u}} = m_{\tilde{d}} = m_{\tilde{c}} = m_{\tilde{s}} = m_{\tilde{b}}$	
$\tilde{g}$	53.0(90%CL)	$m_{\tilde{\gamma}} < 10$ GeV	UA1

Table 3.

E_{beam} (GeV)	$\int Ldt$ (pb^{-1})	Trigger	channel	efficiency (%)
26.0	3.60 ± 0.14	I	$e\bar{e}$	35.2 ± 1.5
			$\mu\bar{\mu}$	12.9 ± 1.1
			$\tau\bar{\tau}$	10.1 ± 1.0
			$q\bar{q}$	24.5 ± 1.4
27.5	0.99 ± 0.04	I	$e\bar{e}$	38.4 ± 1.5
			$\mu\bar{\mu}$	13.6 ± 1.1
			$\tau\bar{\tau}$	8.9 ± 0.9
			$q\bar{q}$	24.0 ± 1.4
27.5	1.89 ± 0.08	II	$e\bar{e}$	38.4 ± 1.5
			$\mu\bar{\mu}$	23.6 ± 1.3
			$\tau\bar{\tau}$	9.5 ± 0.9
			$q\bar{q}$	24.0 ± 1.4
28.25	0.95 ± 0.04	II	$e\bar{e}$	36.3 ± 1.5
			$\mu\bar{\mu}$	21.5 ± 1.3
			$\tau\bar{\tau}$	11.2 ± 1.0
			$q\bar{q}$	22.1 ± 1.3
28.5	3.63 ± 0.14	II	$e\bar{e}$	33.6 ± 1.5
			$\mu\bar{\mu}$	22.2 ± 1.3
			$\tau\bar{\tau}$	10.6 ± 1.0
			$q\bar{q}$	21.1 ± 1.3

Table 4.

	Lower mass limit to $m_{\tilde{q}}$(GeV) for $Q = 2/3$	
$m_{\tilde{\gamma}}$(GeV)	$m_{\tilde{q}_L} = m_{\tilde{q}_R}$	$m_{\tilde{q}_L} \gg m_{\tilde{q}_R}$
0	26.3	24.4
5	26.3	24.3
10	26.2	24.2
15	26.1	24.0

Table 5.

$\binom{\nu_e}{e}_L$ $\nu_{e,R}, e_R$	$\binom{\nu_\mu}{\mu}_L$ $\nu_{\mu,R}, \mu_R$	$\binom{\nu_\tau}{\tau}_L$ $\nu_{\tau,R}, \tau_R$
$\binom{u_c}{d_c}_L$ u_{cR}, d_{cR} c: red,green,blue	$\binom{c_c}{s_c}_L$ c_{cR}, s_{cR} c: red,green,blue	$\binom{t_c}{b_c}_L$ t_{cR}, b_{cR} c: red,green,blue
$g_i, \gamma, Z^0, W^\pm$		
H^0		

FIGURE CAPTIONS

1. Proton decay diagram when the R parity is not conserved.
2. Feynman diagrams for the production of SUSY particles. The diagrams took into account in this analysis are indicated by shadow.
3. Typical production cross section of SUSY particles as a function of their mass at $\sqrt{s} = 55GeV$.
4. Feynman diagrams of chargino decay when the LSP is the photino and the NLSP is the chargino.
5. The layout of the TRISTAN.
6. Bird's eye and cross-sectional views of the TOPAZ detector.
7. Coordinate system of the TOPAZ detector.
8. The Time projection chamber.
9. Front view of the TPC sector.
10. Electric filed of the sector when gating grid is open (a) and closed (b).
11. Schematic view of the BCL.
12. Energy distribution of the BCL for Bhabha events at $\sqrt{s} = 52$ GeV.
13. Schematic view of the ECL.
14. Energy distribution of the ECL for Bhabha events at $\sqrt{s} = 52$ GeV.
15. Scheme of the trigger system.
16. Scheme of the energy trigger.
17. Principle of the track pre-trigger.
18. Timing sequence of the trigger.
19. Principle of the TPC trigger.
20. The TOPAZ data acquisition system.
21. Time sequence of the data acquisition.
22. Tasks on the online computer VAX11/780.
23. Scheme of the raw data processing.

24. Architecture of the TPC analysis.

25. Parametrization of charged tracks.

26. Curvature distribution of two measurements of a cosmic ray event by the TPC.

27. Momentum resolution of the TPC as a function of the momentum.

28. Flow of the analysis.

29. Event signatures of SUSY particle.

30. Feynman diagrams including initial photon radiative correction.

31. Scatter plot before the missing energy and the acoplanarity cuts (a) for electron pair candidates. Fig (b) and (c) show their projection to the horizontal and vertical axes (dots) with the Monte Calro simulation (solid line).

32. Scatter plot before the momentum and the acoplanarity cuts (a) for μ pair candidates. Fig (b) and (c) show their projection to the horizontal and vertical axes (dots) with the Monte Calro simulation (solid line).

33. Scatter plot before the missing momentum and the acoplanarity cut (a) for 1-1 mode of the tau decay. Fig (b) and (c) show their projection to the horizontal and vertical axis (dots) with the Monte Calro simulation (solid line).

34. Scatter plot for missing momentum versus acoplanarity angle before the acoplanarity cut (a) for 1-n mode for the tau decay. Fig (b) and (c) show their projection horizontal and vertical axis with the Monte Calro expectation.

35. Scatter plot for visible energy versus acoplanarity angle before the cuts (a) for the multi hadron candidates. Fig (b) and (c) show their projection horizontal and vertical axis with the Monte Calro expectation.

36. The 95% CL lower limit to chargino mass as a function of leptonic branching ratio, assuming (a) $m_\gamma = 0$ and (b) $m_\gamma = 10$ GeV, respectively. The solid, the CELLO, and the JADE lines assume equal branching ratio to each leptonic mode and the dotted line corresponds to the most pessimistic case described in the text.

37. The 95% CL limit to scalar electron mass as a function of photino mass, assuming (a) $m_{\tilde{e}_R} = m_{\tilde{e}_L}$ and (b) $m_{\tilde{e}_R} << m_{\tilde{e}_L}$, respectively. The ASP limits were obtained by single photon search and set at the 90% CL. In the case of

$m_{\tilde{\gamma}} < m_{\tilde{e}}$ the limits are from the acoplanar electron pair search and in the case of $m_{\tilde{\gamma}} > m_{\tilde{e}}$, the limits from the stable heavy particle search.

38. The 95% CL limit to scalar muon mass as a function of photino mass, assuming (a) $m_{\tilde{\mu}_R} = m_{\tilde{\mu}_L}$ and (b) $m_{\tilde{\mu}_R} << m_{\tilde{\mu}_L}$, respectively. The limits are obtained from the acoplanar muon pair search in the case of $m_{\tilde{\gamma}} < m_{\tilde{\mu}}$. The stable heavy particle search resulted in the limits for $m_{\tilde{\gamma}} > m_{\tilde{\mu}}$.

39. The 95% CL limit to scalar tau mass as a function of photino mass, assuming $m_{\tilde{\tau}_R} = m_{\tilde{\tau}_L}$. The limits are from the acoplanar tau pair search and the stable heavy particle search below and above the $m_{\tilde{\gamma}} = m_{\tilde{\mu}}$ line, respectively.

40. The 95% CL limit to the parameter μ as a function of v_1/v_2, for $m_{\tilde{\gamma}} = 0$ (a) and 10 GeV (b) respectively.

41. The 95% CL limit to Z^- mass as a function of v_1/v_2, for $m_{\tilde{\gamma}} = 0$ (a) and 10 GeV (b) respectively.

42. The 95% CL limit to Z^+ mass as a function of v_1/v_2, for $m_{\tilde{\gamma}} = 0$ (a) and 10 GeV (b) respectively.

43. The Feynman diagrams of one loop correction for the Higgs scalar mass without (a) and with (b) the SUSY partners.

44. The evolution of the scalar mass as the function of the renormalization scale.

45. Structure of the proportional tube and layers of the ECL.

46. Equivalent circuit of the cathode readout.

47. Pulse height variation of the ECL for the Bhabha events with the correction factor (a) and its pulse height distribution (b) before (dashed line) and after (solid line) the correction.

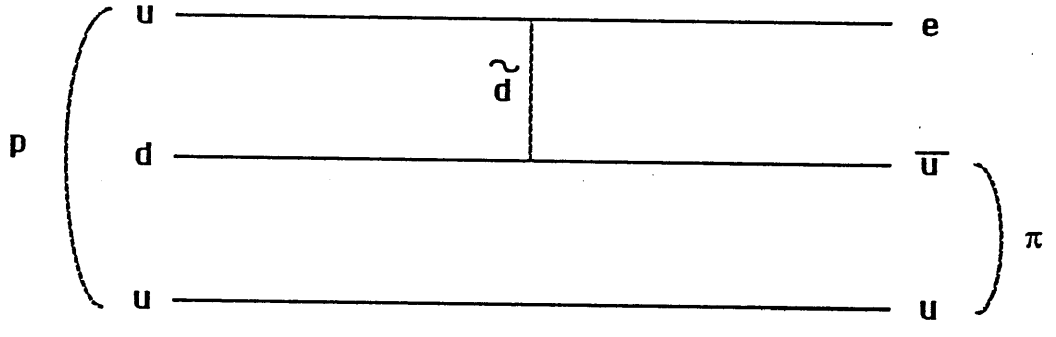

Fig.1

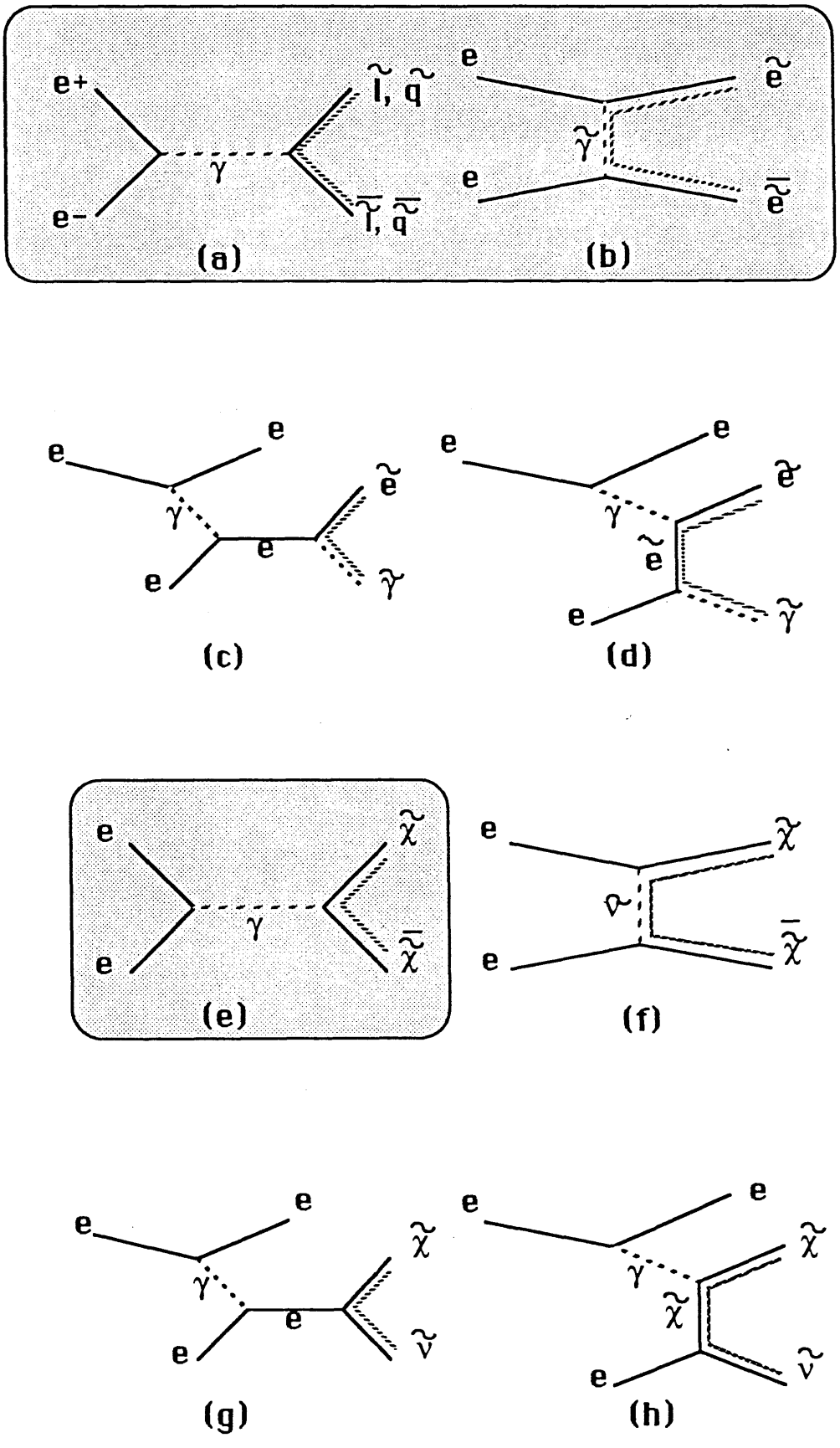
e+
e−
γ
l̃, q̃
l̃̄, q̃̄
(a)
e
e
γ̃
ẽ
ẽ̄
(b)
e
e
γ
e
ẽ
γ̃
(c)
e
e
γ
ẽ
ẽ
γ̃
(d)
e
e
γ
χ̃
χ̃̄
(e)
e
e
χ̃
χ̃̄
(f)
e
e
γ
e
χ̃
ν̃
(g)
e
e
γ
χ̃
χ̃
ν̃
(h)

Fig.2

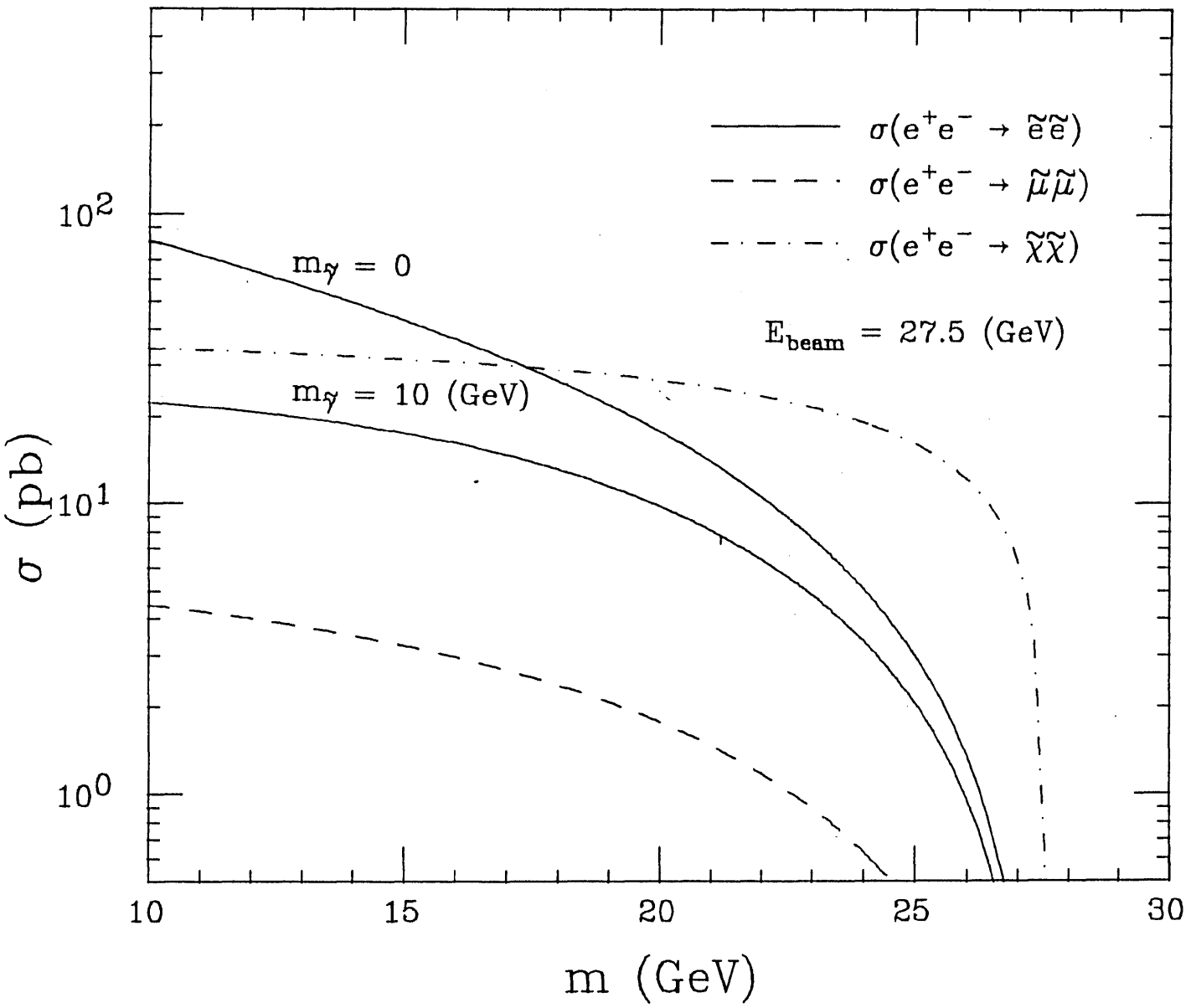
$\sigma(e^+e^- \to \tilde{e}\tilde{e})$
$\sigma(e^+e^- \to \tilde{\mu}\tilde{\mu})$
$\sigma(e^+e^- \to \tilde{\chi}\tilde{\chi})$
E_{beam} = 27.5 (GeV)
$m_{\tilde{\gamma}}$ = 0
$m_{\tilde{\gamma}}$ = 10 (GeV)
10^2
10^1
10^0
σ (pb)
10
15
20
25
30
m (GeV)

Fig.3

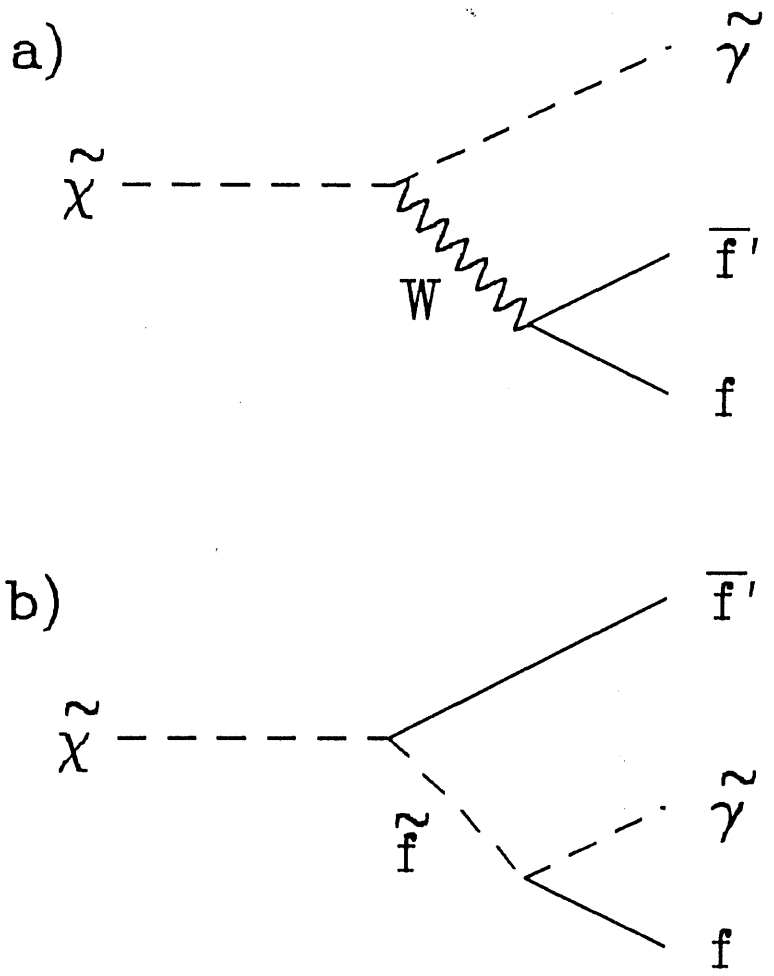
a)
$\tilde{\gamma}$
$\tilde{\chi}$
$\bar{f}'$
W
f
b)
$\bar{f}'$
$\tilde{\chi}$
$\tilde{f}$
$\tilde{\gamma}$
f

Fig.4

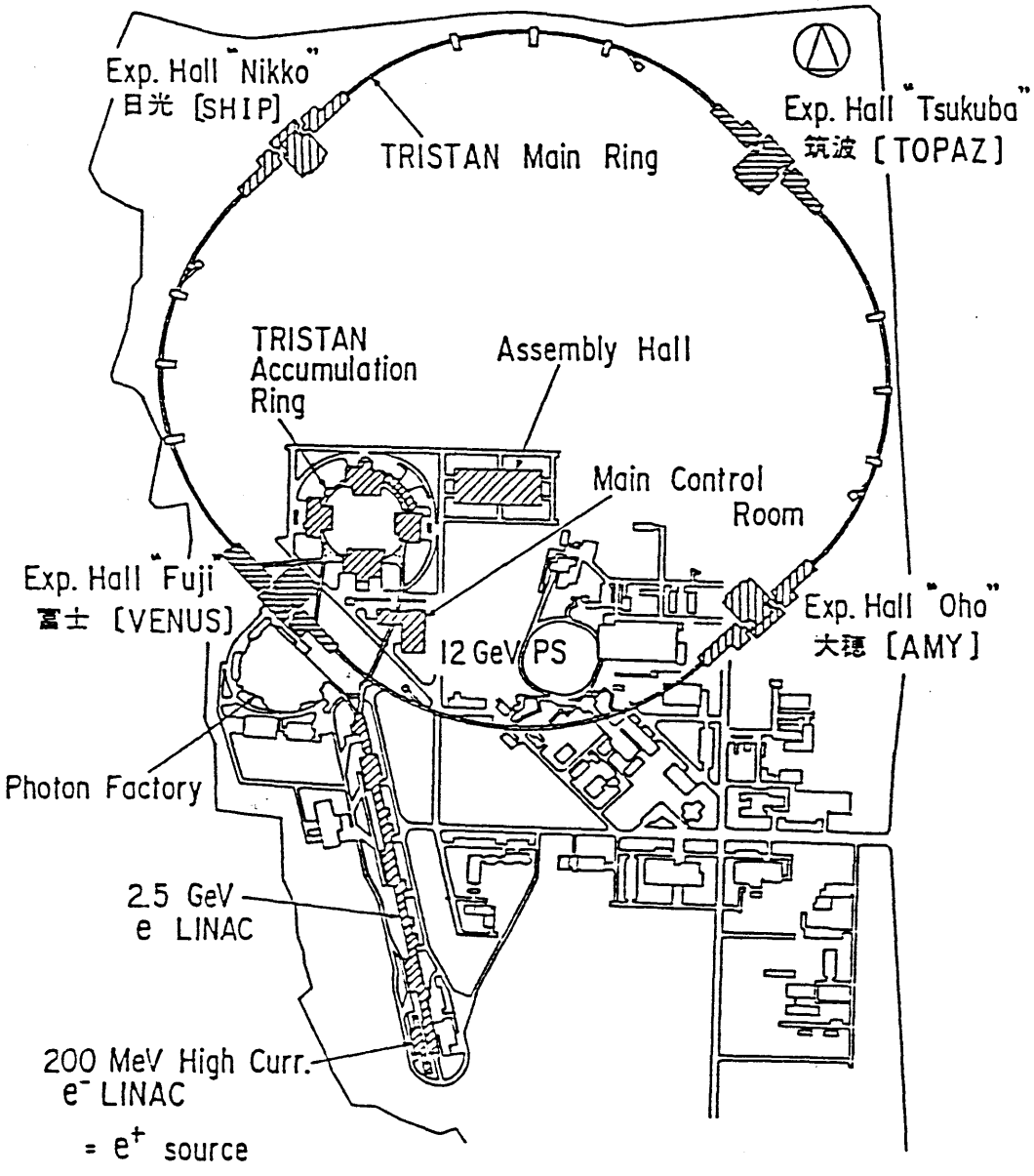
Exp. Hall "Nikko"
日光 [SHIP]
TRISTAN Main Ring
Exp. Hall "Tsukuba"
筑波 [TOPAZ]
TRISTAN
Accumulation
Ring
Assembly Hall
Main Control
Room
Exp. Hall "Fuji"
富士 [VENUS]
12 GeV PS
Exp. Hall "Oho"
大穂 [AMY]
Photon Factory
2.5 GeV
e LINAC
200 MeV High Curr.
e⁻ LINAC
= e⁺ source

Fig.5

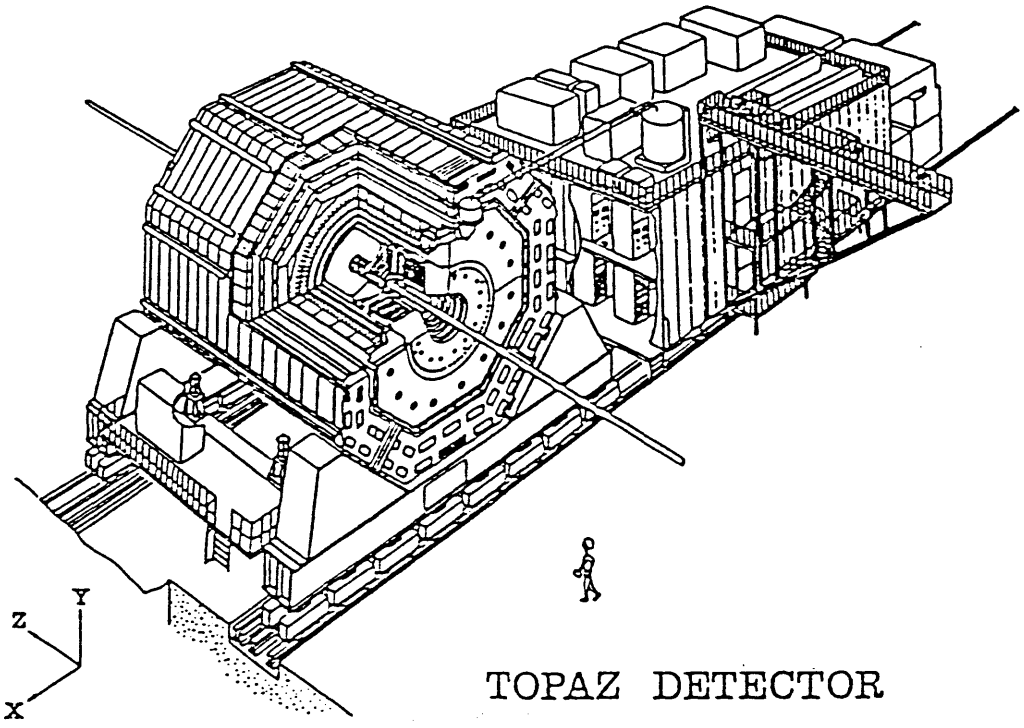
Z
Y
X
TOPAZ DETECTOR

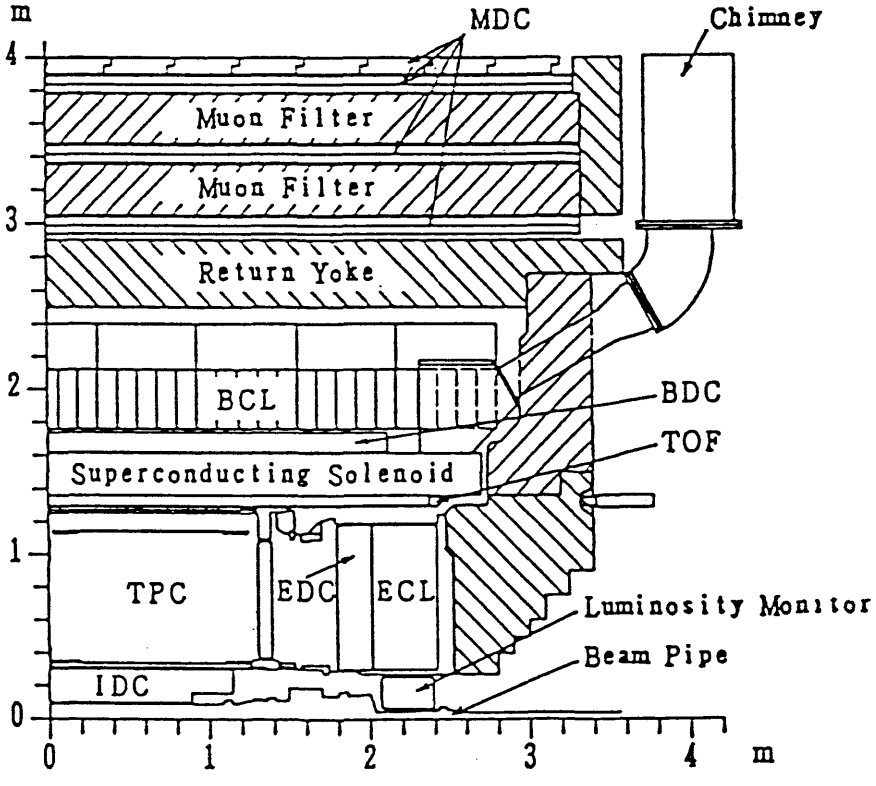
m
MDC
Chimney
Muon Filter
Muon Filter
Return Yoke
BCL
BDC
TOF
Superconducting Solenoid
TPC
EDC
ECL
Luminosity Monitor
Beam Pipe
IDC
0
1
2
3
4
m

Fig.6

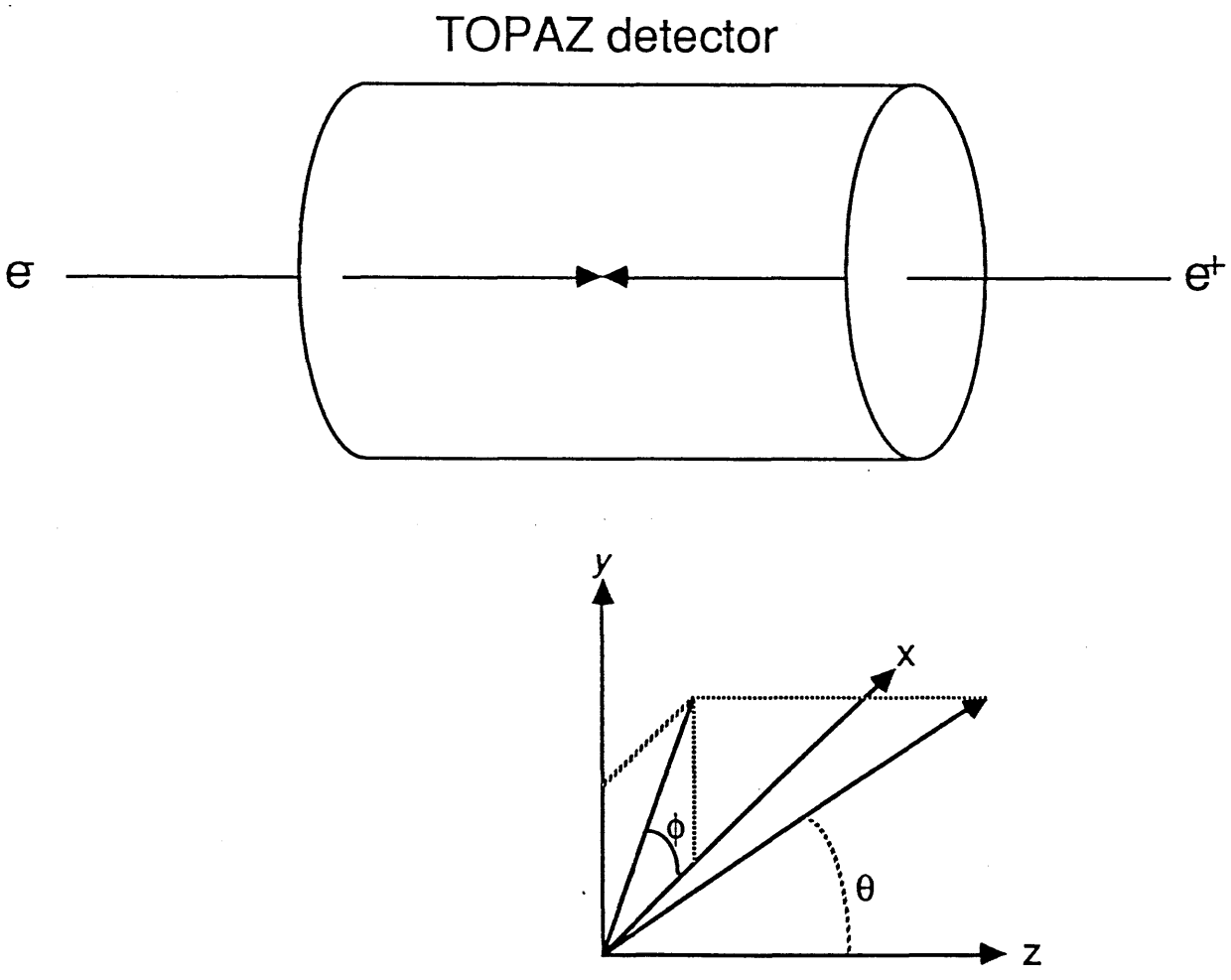

Fig.7

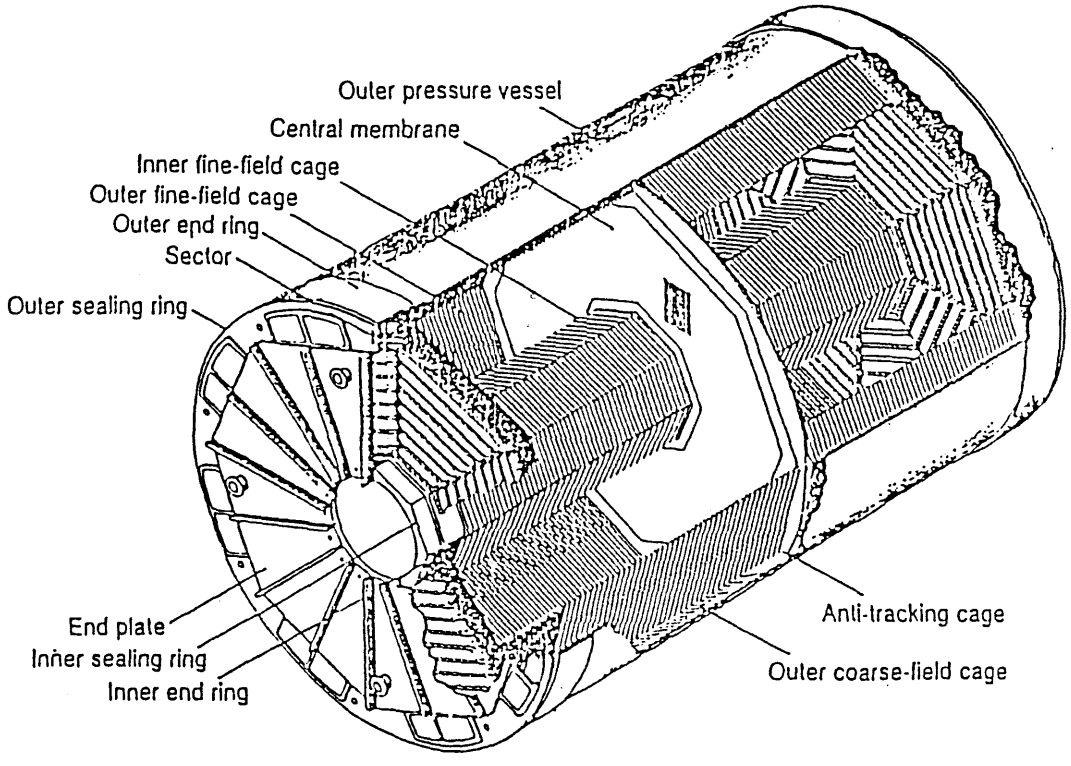
Outer pressure vessel
Central membrane
Inner fine-field cage
Outer fine-field cage
Outer end ring
Sector
Outer sealing ring
End plate
Inner sealing ring
Inner end ring
Anti-tracking cage
Outer coarse-field cage

Fig.8

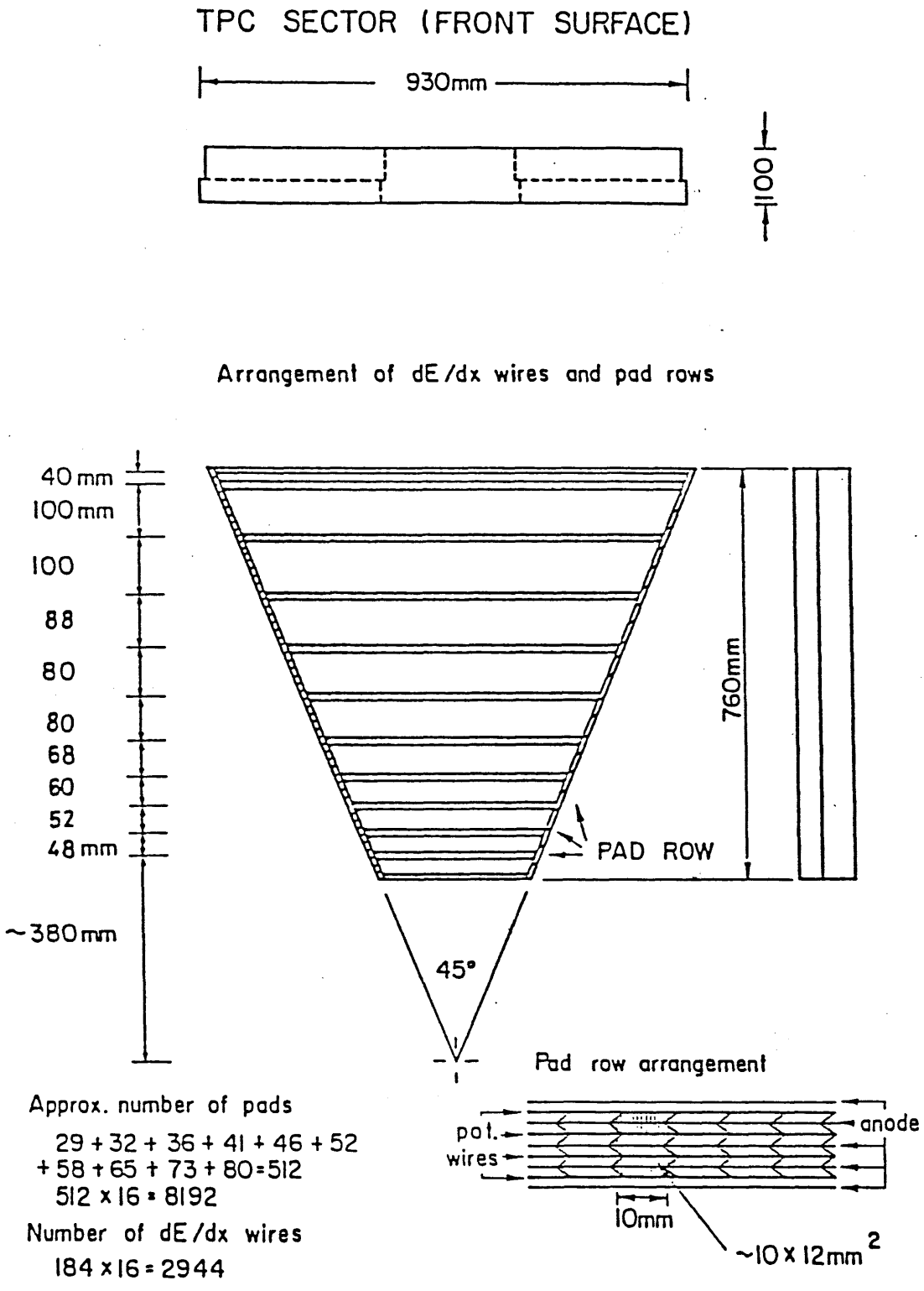
TPC SECTOR (FRONT SURFACE)
930mm
100
Arrangement of dE/dx wires and pad rows
40 mm
100 mm
100
88
80
80
68
60
52
48 mm
~380 mm
760mm
PAD ROW
45°
Pad row arrangement
pot. wires
anode
10mm
~10 x 12mm 2
Approx. number of pads
29 + 32 + 36 + 41 + 46 + 52
+ 58 + 65 + 73 + 80 = 512
512 x 16 = 8192
Number of dE/dx wires
184 x 16 = 2944

Fig.9

Sector Wire Geometry

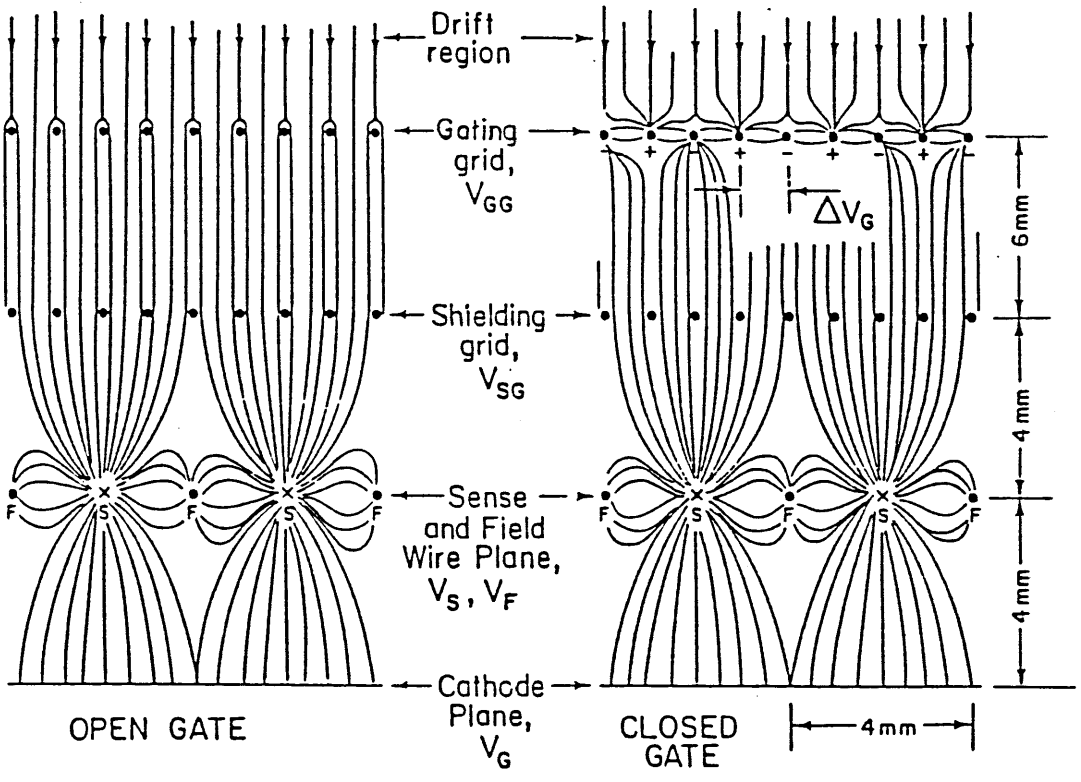

Fig.10

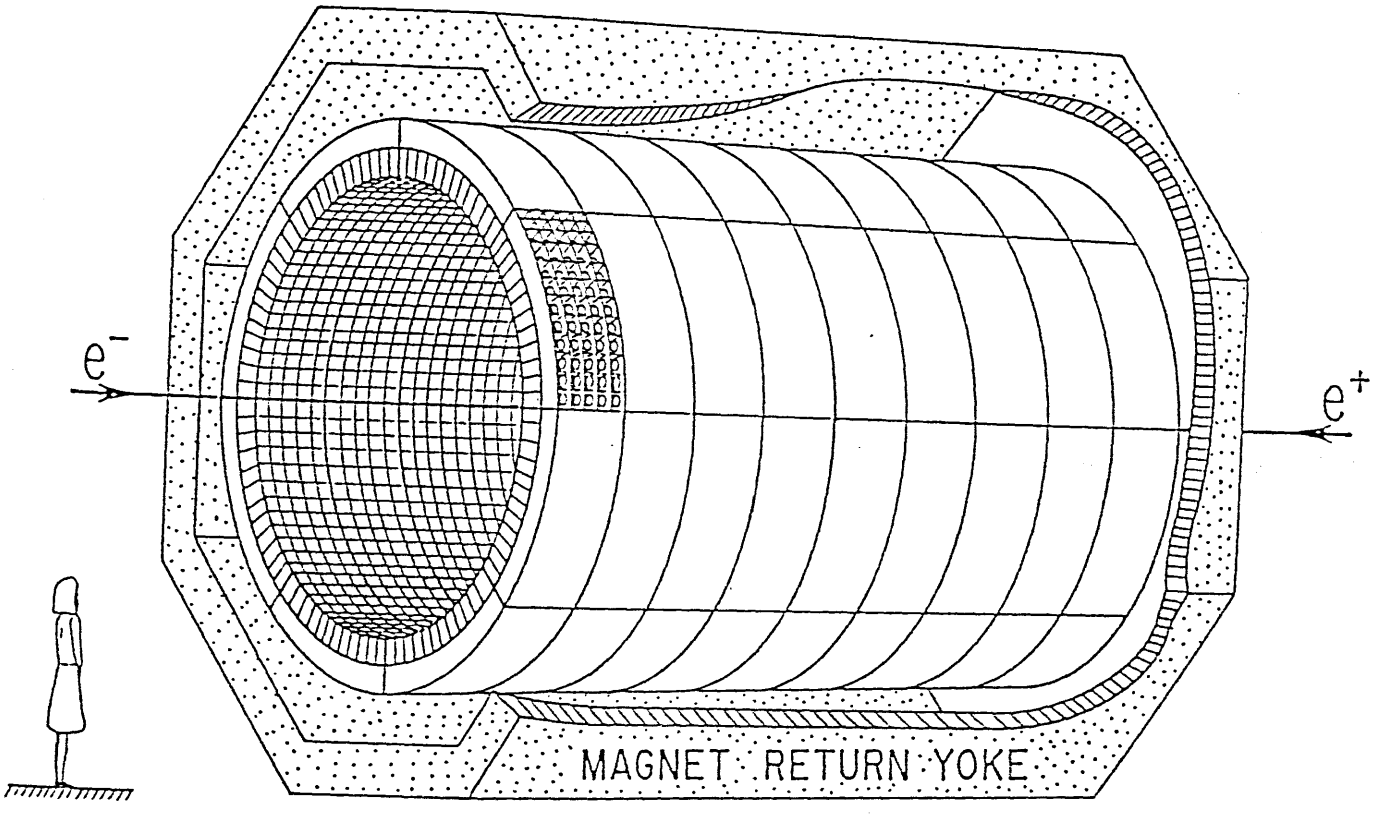

Fig.11

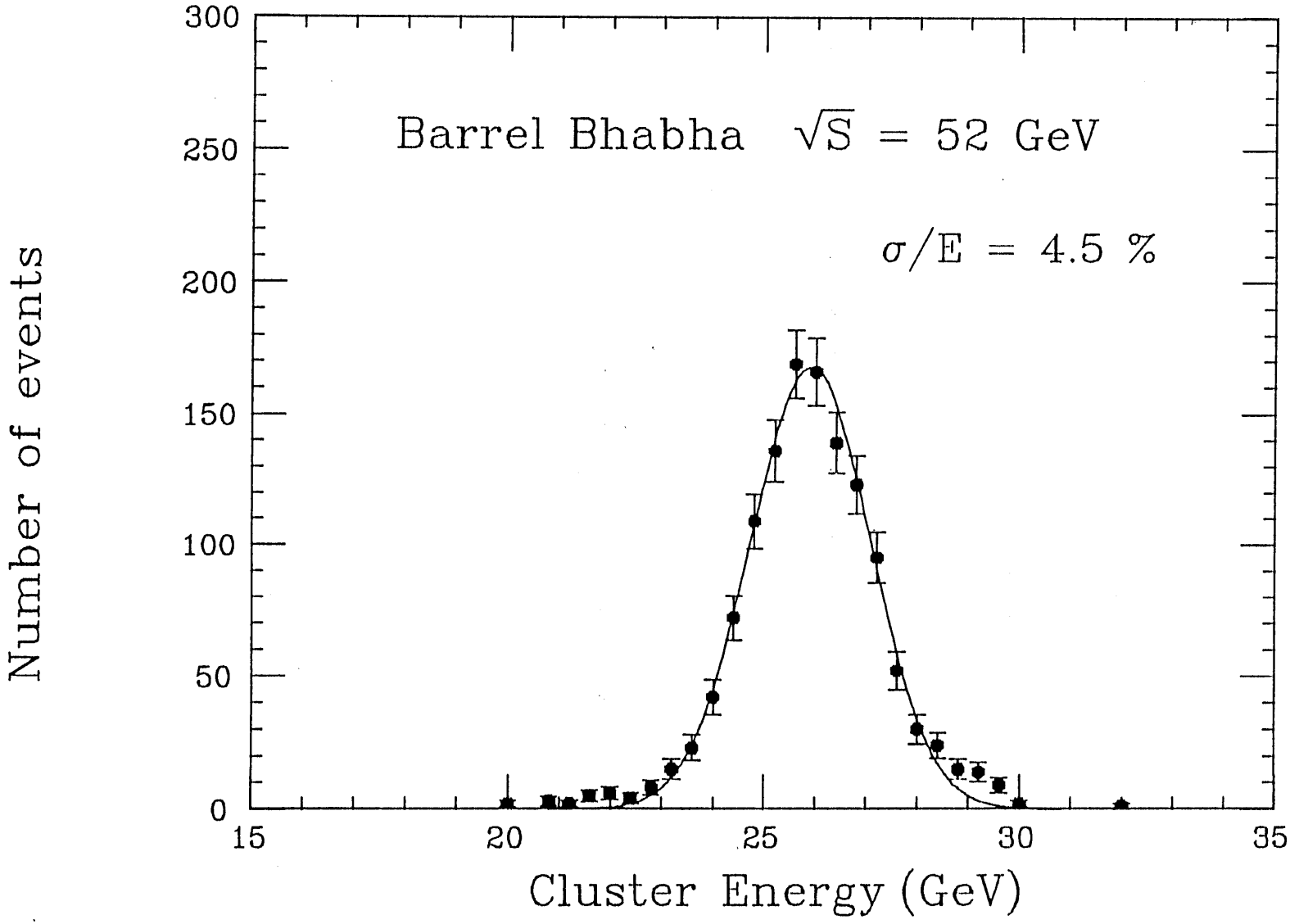
Barrel Bhabha $\sqrt{S}$ = 52 GeV
σ/E = 4.5 %
Number of events
Cluster Energy (GeV)
0
50
100
150
200
250
300
15
20
25
30
35

Fig.12

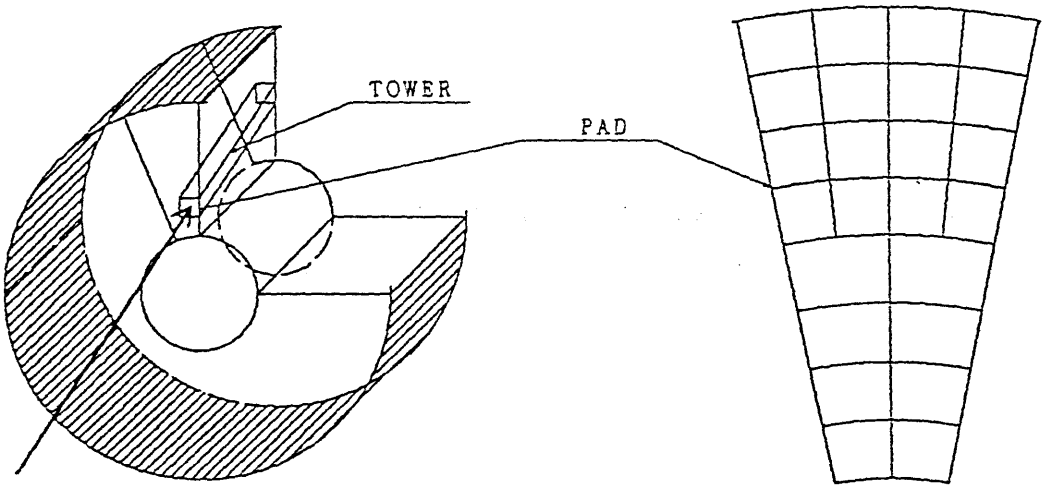

Fig.13

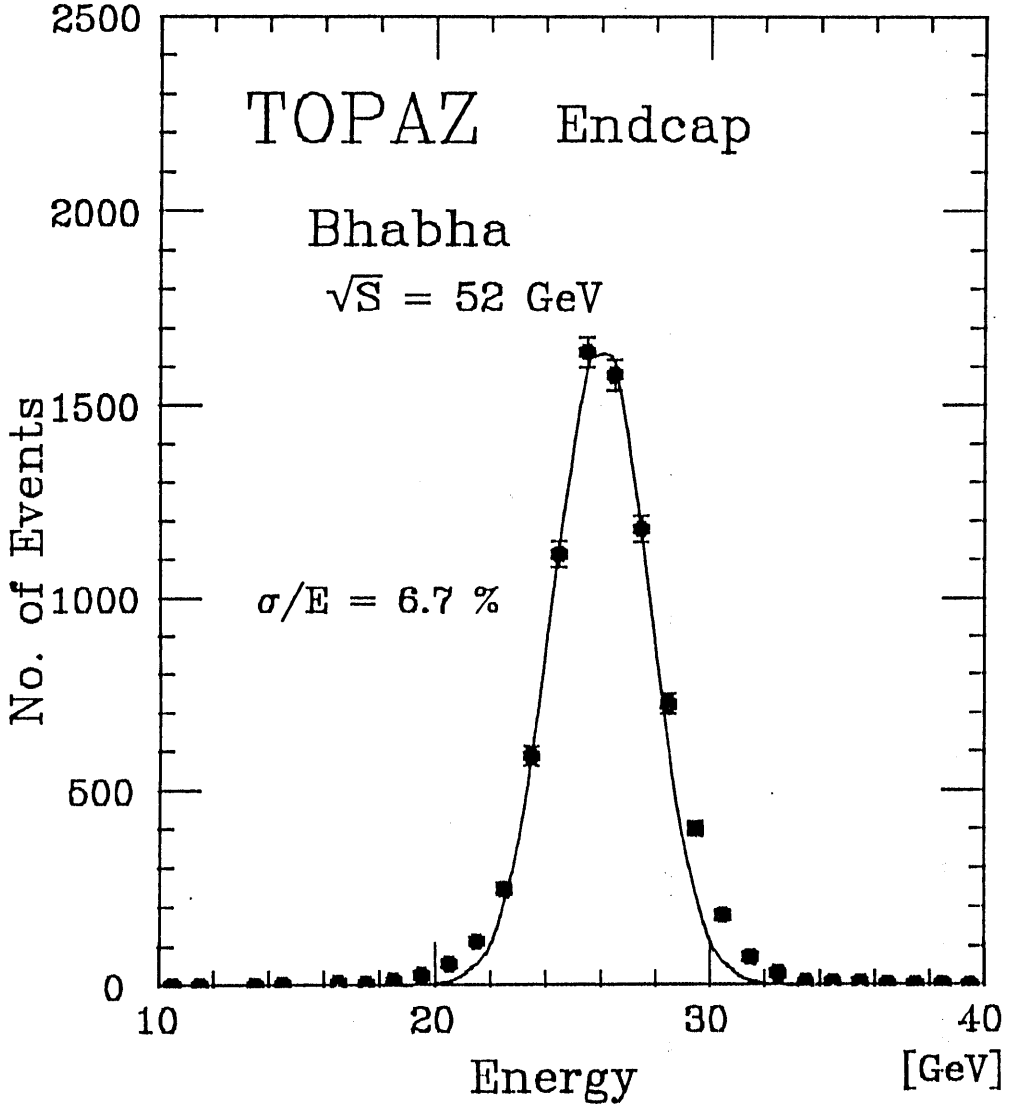
TOPAZ Endcap
Bhabha
√S = 52 GeV
σ/E = 6.7 %
No. of Events
2500
2000
1500
1000
500
0
10
20
30
40
Energy
[GeV]

Fig.14

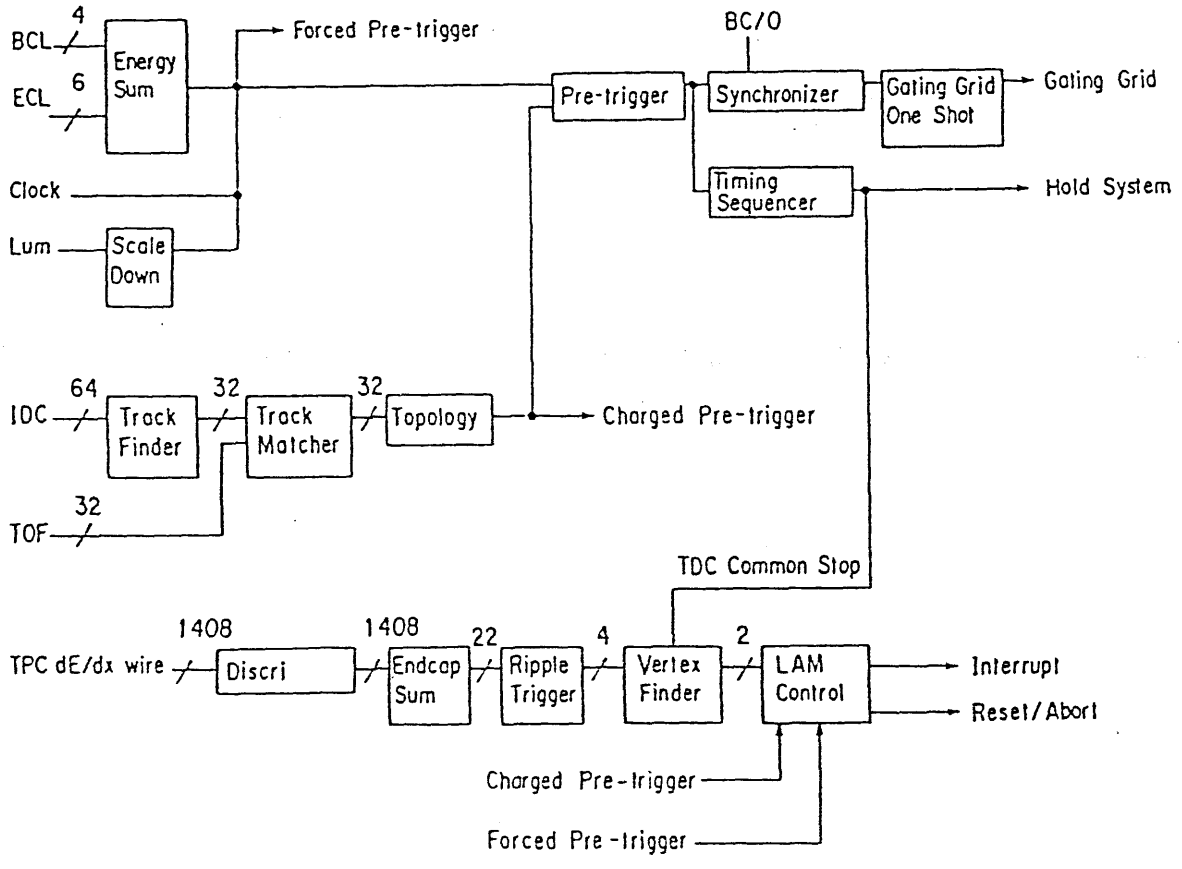
BCL
4
ECL
6
Energy Sum
Forced Pre-trigger
BC/O
Pre-trigger
Synchronizer
Gating Grid One Shot
Gating Grid
Clock
Timing Sequencer
Hold System
Lum
Scale Down
IDC
64
Track Finder
32
Track Matcher
32
Topology
Charged Pre-trigger
TOF
32
TDC Common Stop
TPC dE/dx wire
1408
Discri
1408
Endcap Sum
22
Ripple Trigger
4
Vertex Finder
2
LAM Control
Interrupt
Reset/Abort
Charged Pre-trigger
Forced Pre-trigger

Fig.15

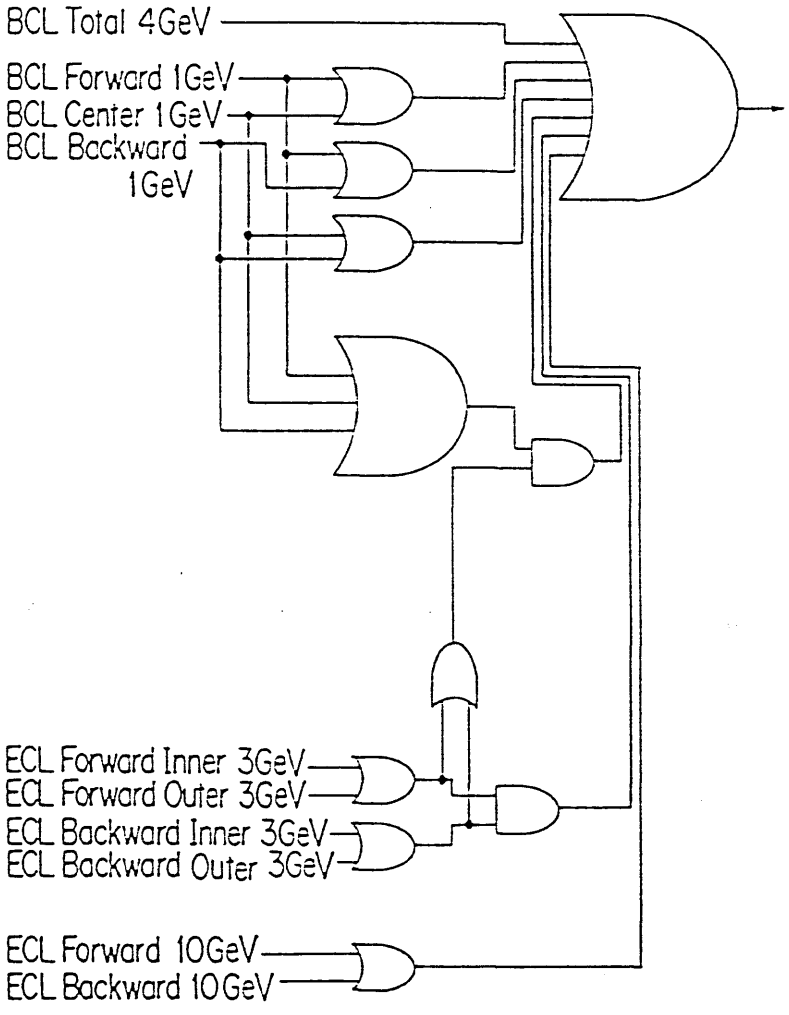
BCL Total 4GeV
BCL Forward 1GeV
BCL Center 1GeV
BCL Backward 1GeV
ECL Forward Inner 3GeV
ECL Forward Outer 3GeV
ECL Backward Inner 3GeV
ECL Backward Outer 3GeV
ECL Forward 10GeV
ECL Backward 10GeV

Fig.16

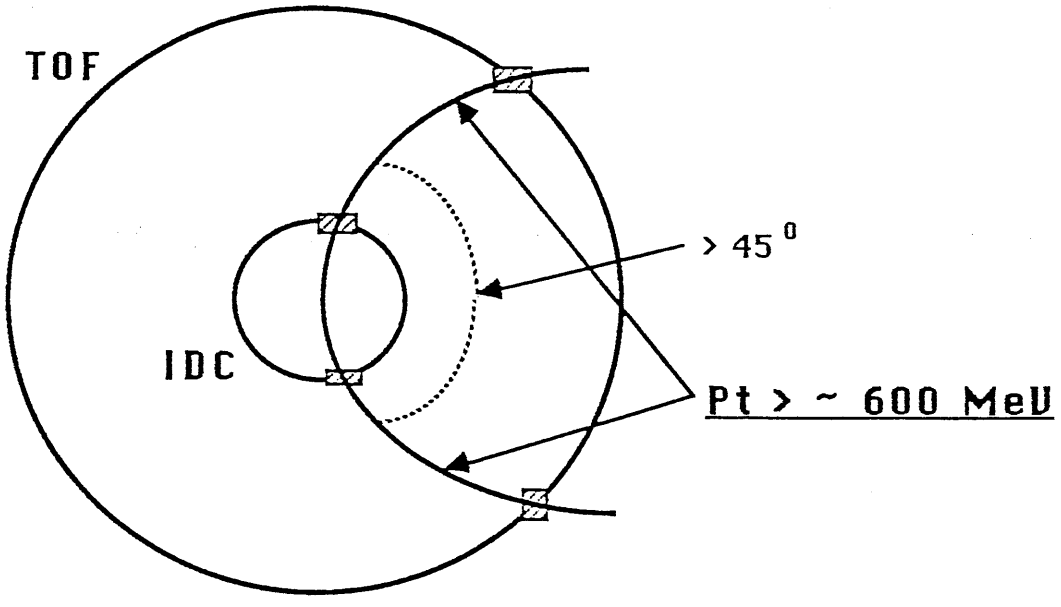

Fig.17

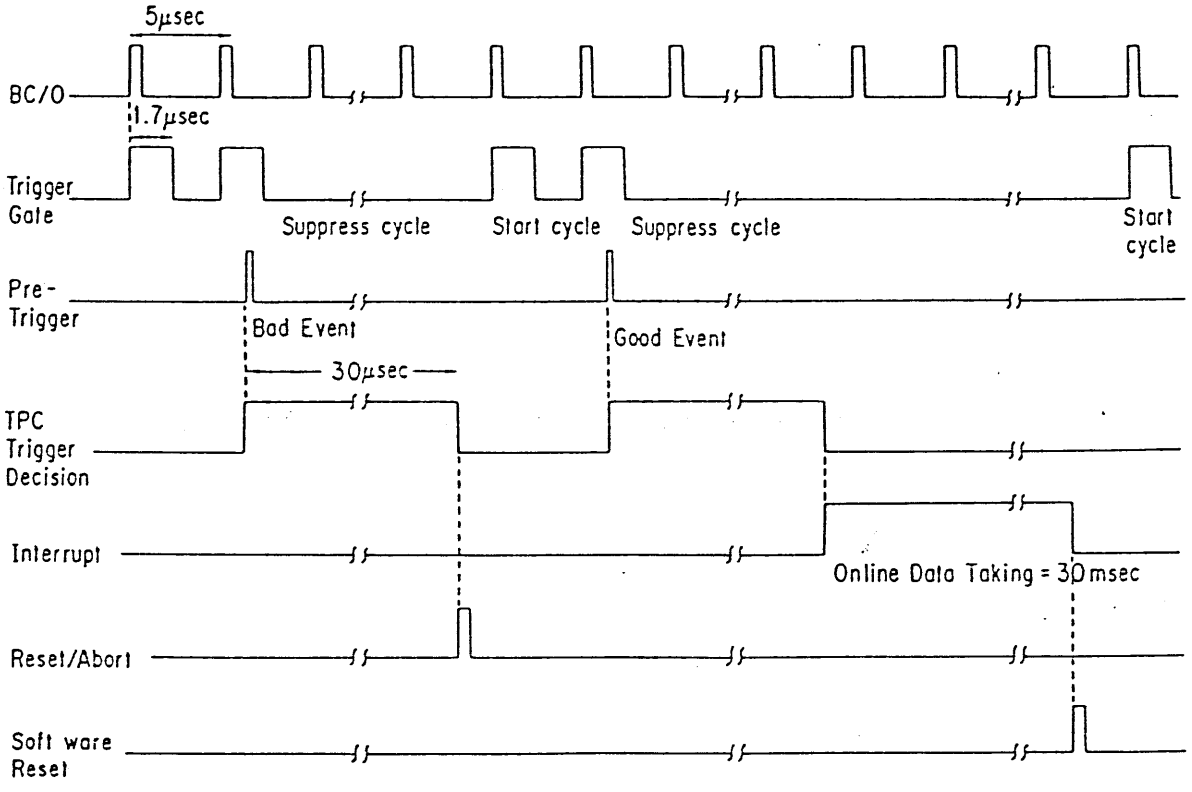
5μsec
BC/O
1.7μsec
Trigger Gate
Suppress cycle
Start cycle
Suppress cycle
Start cycle
Pre-Trigger
Bad Event
Good Event
30μsec
TPC Trigger Decision
Interrupt
Online Data Taking = 30msec
Reset/Abort
Soft ware Reset

Fig.18

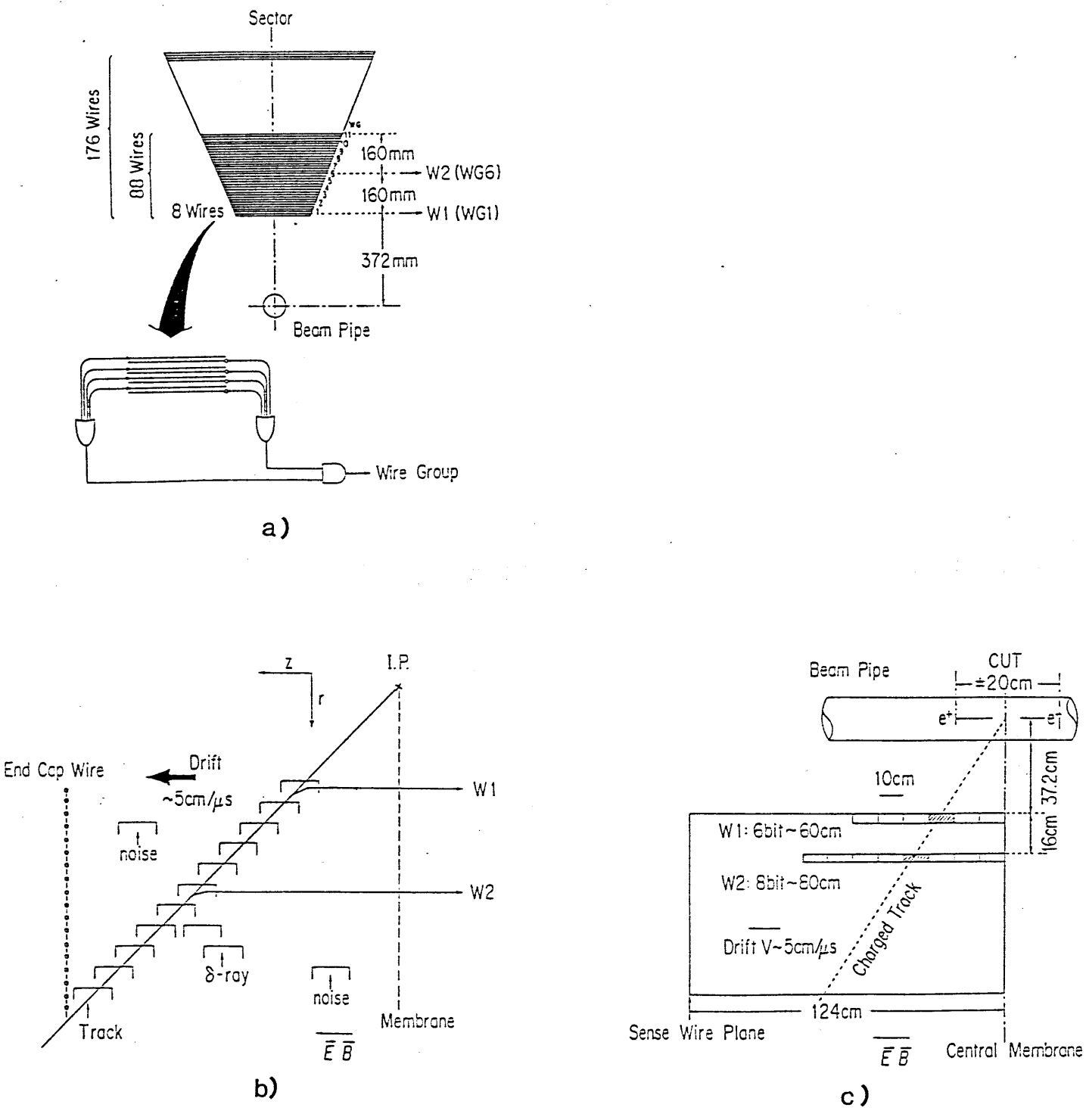
Sector
176 Wires
88 Wires
8 Wires
160mm
W2 (WG6)
160mm
W1 (WG1)
372mm
Beam Pipe
Wire Group
a)
z
r
I.P.
End Cap Wire
Drift
~5cm/μs
W1
noise
W2
δ-ray
noise
Track
Membrane
E B
b)
Beam Pipe
CUT
±20cm
e+
e-
10cm
37.2cm
16cm
W1: 6bit~60cm
W2: 8bit~80cm
Drift V~5cm/μs
Charged Track
124cm
Sense Wire Plane
E B
Central Membrane
c)

Fig.19

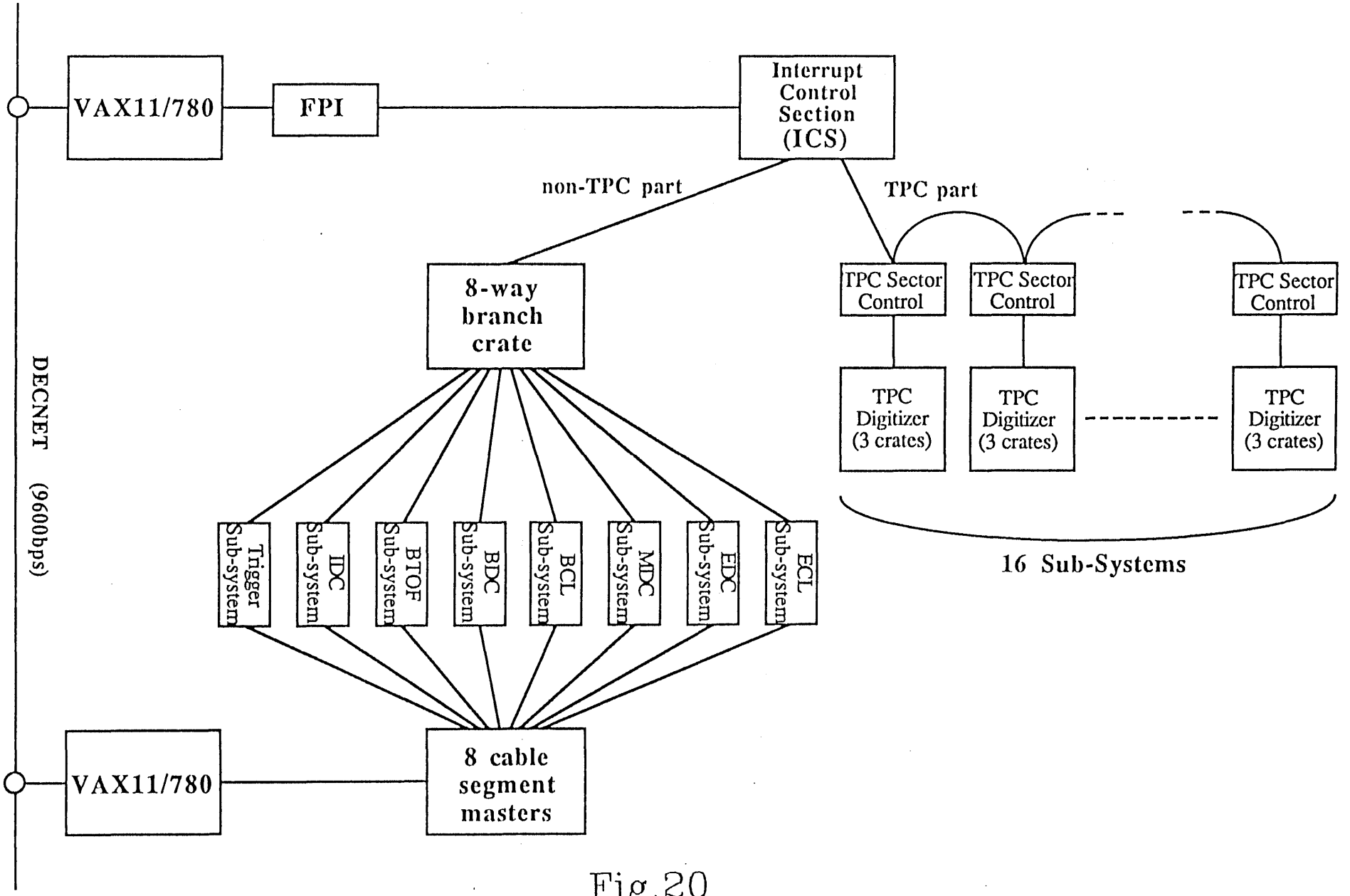
DECNET (9600bps)
VAX11/780
FPI
Interrupt Control Section (ICS)
non-TPC part
TPC part
8-way branch crate
TPC Sector Control
TPC Sector Control
TPC Sector Control
TPC Digitizer (3 crates)
TPC Digitizer (3 crates)
TPC Digitizer (3 crates)
Trigger Sub-system
IDC Sub-system
BTOF Sub-system
BDC Sub-system
BCL Sub-system
MDC Sub-system
EDC Sub-system
ECL Sub-system
16 Sub-Systems
VAX11/780
8 cable segment masters

Fig.20

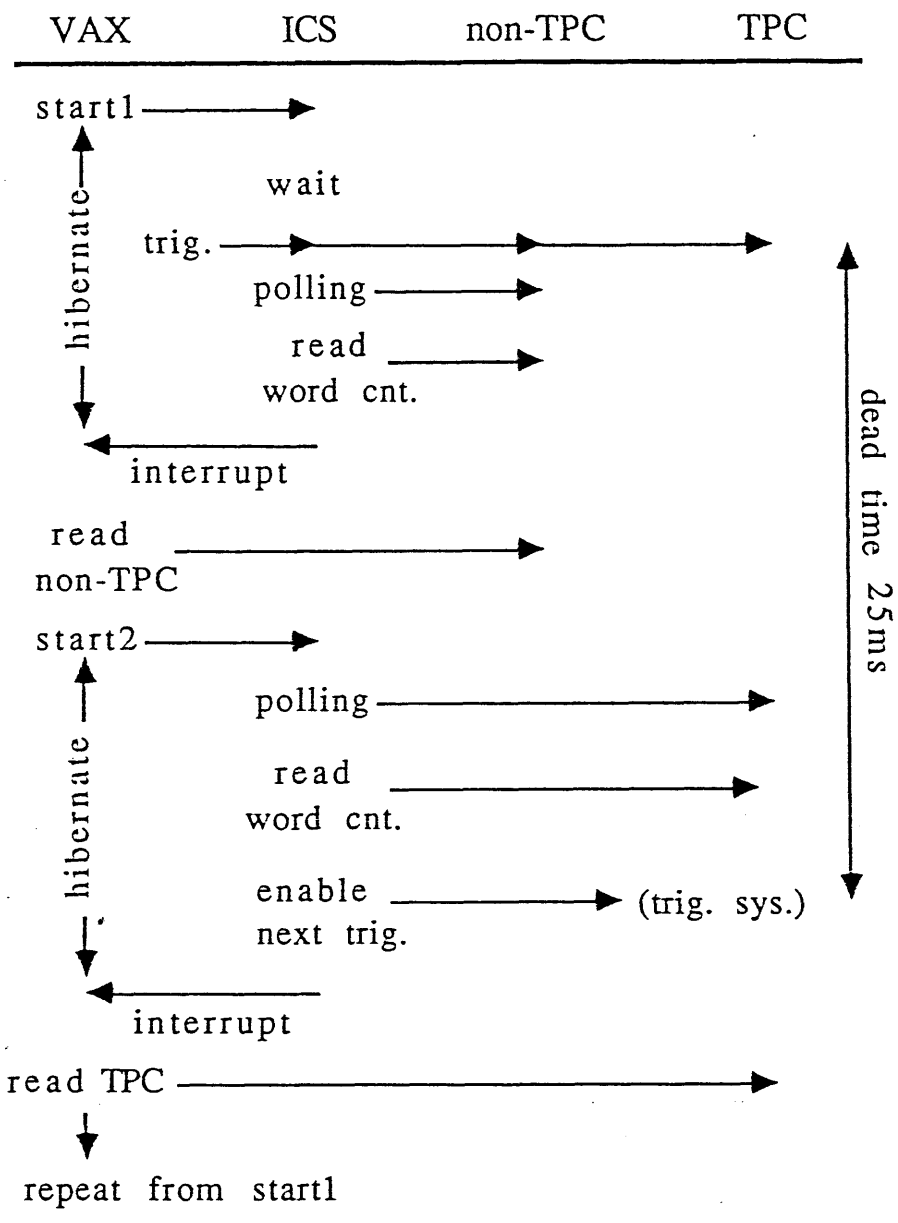
VAX
ICS
non-TPC
TPC
start1
hibernate
wait
trig.
polling
read
word cnt.
interrupt
read
non-TPC
start2
hibernate
polling
read
word cnt.
enable
next trig.
(trig. sys.)
interrupt
read TPC
repeat from start1
dead time 25ms

Fig.21

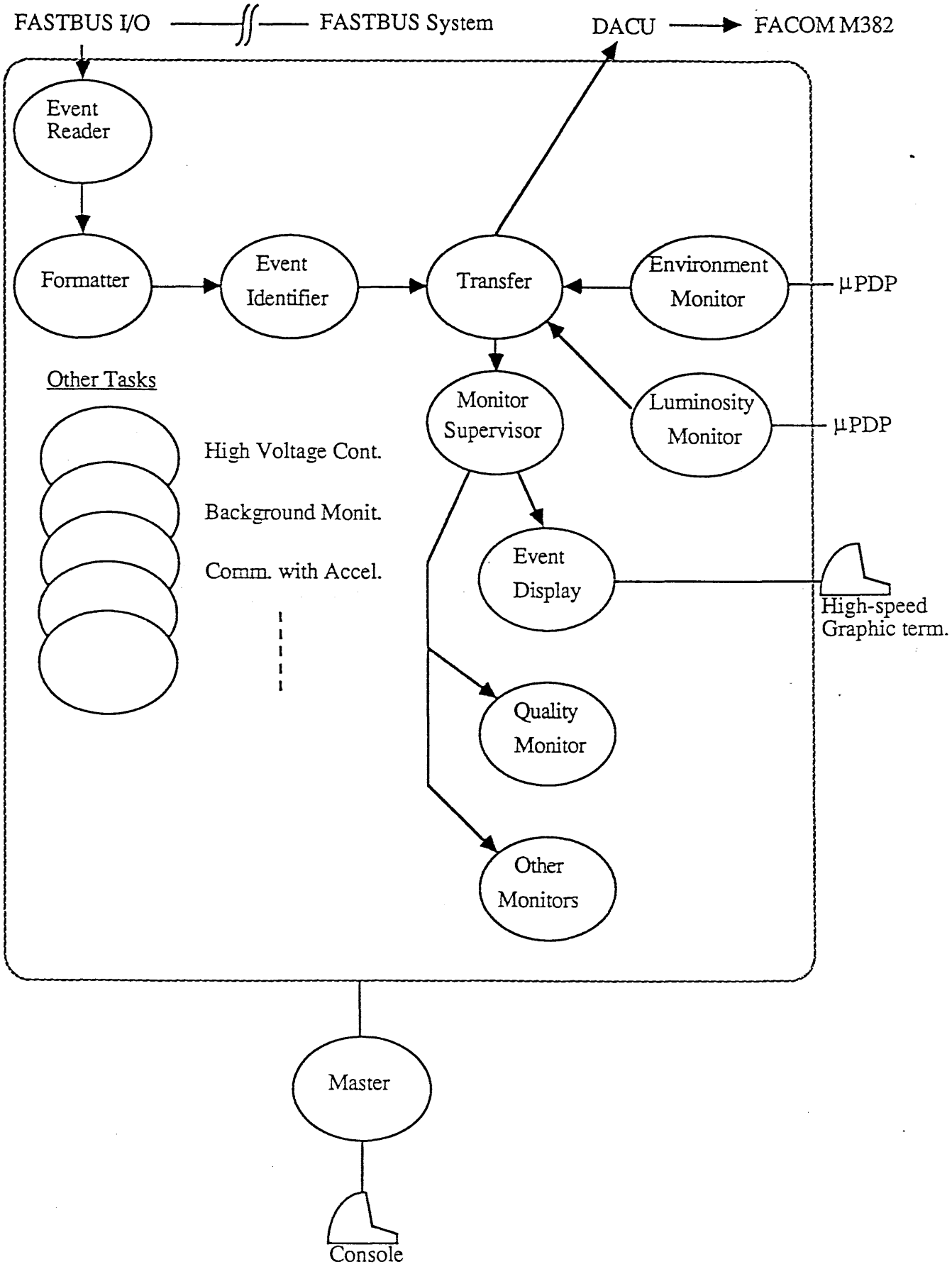
FASTBUS I/O
FASTBUS System
DACU
FACOM M382
Event Reader
Formatter
Event Identifier
Transfer
Environment Monitor
μPDP
Luminosity Monitor
μPDP
Monitor Supervisor
Other Tasks
High Voltage Cont.
Background Monit.
Comm. with Accel.
Event Display
High-speed Graphic term.
Quality Monitor
Other Monitors
Master
Console

Fig.22

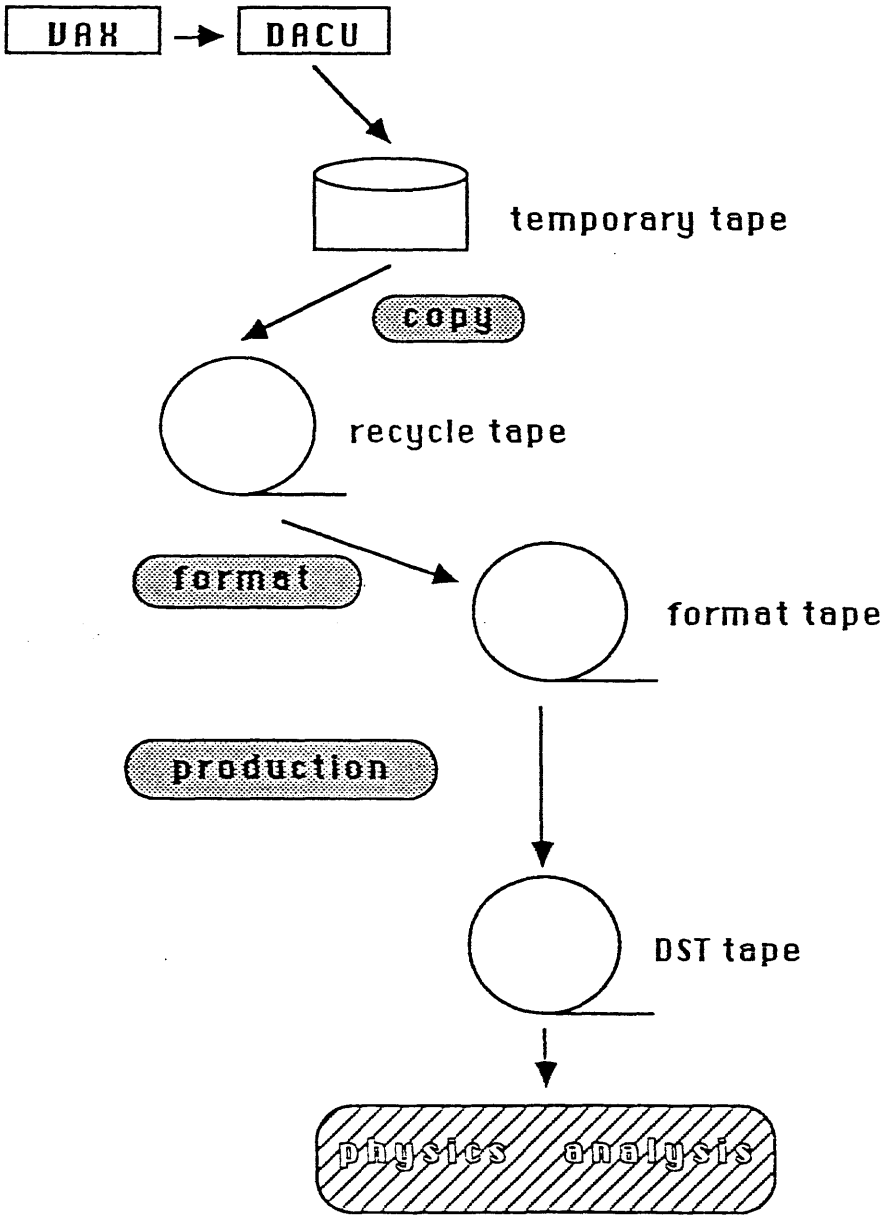
VAX
DACU
temporary tape
copy
recycle tape
format
format tape
production
DST tape
physics analysis

Fig.23

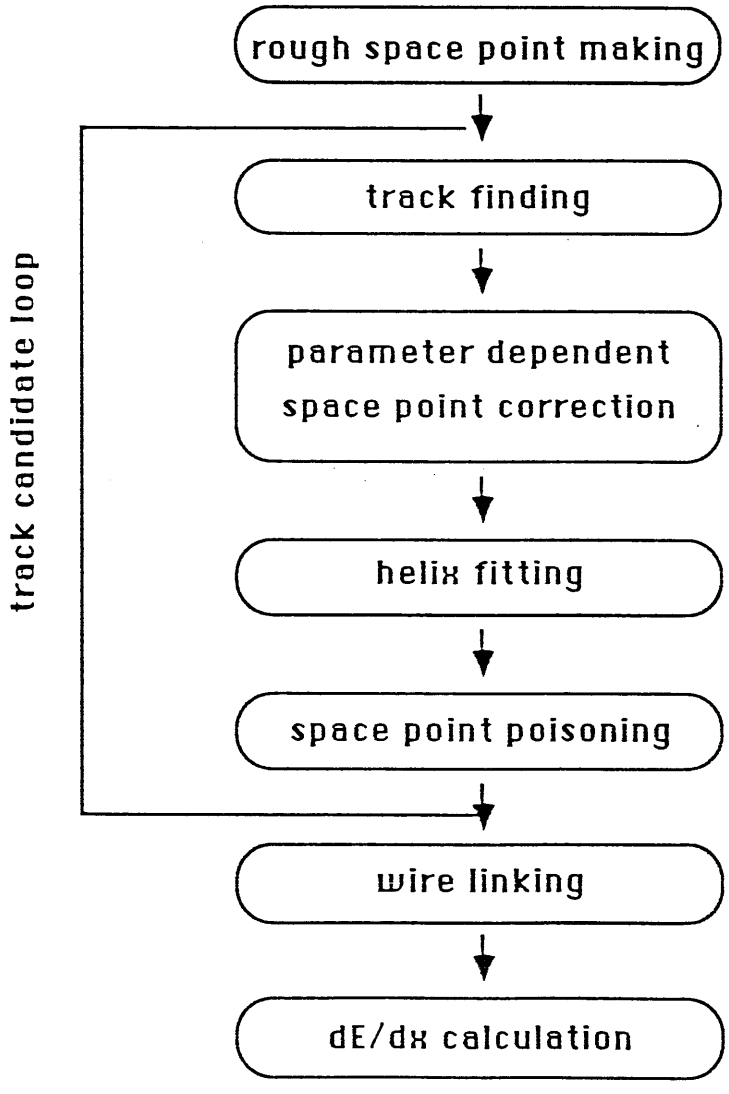
rough space point making
track finding
parameter dependent
space point correction
helix fitting
space point poisoning
wire linking
dE/dx calculation
track candidate loop

Fig.24

Positive Track

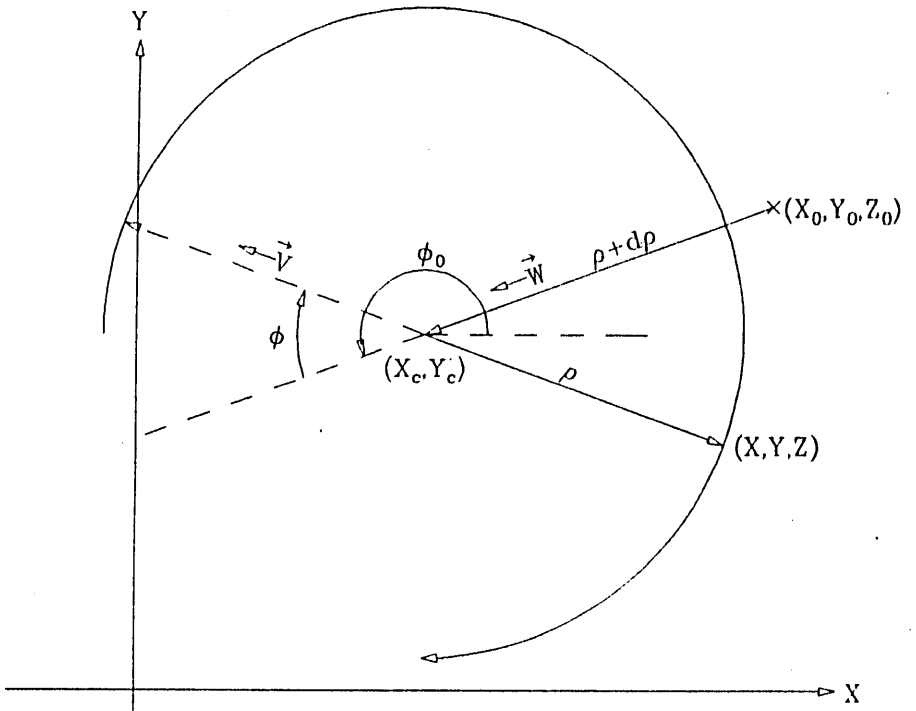

In X−Y Plane.

$$\vec{X} = \vec{X}_0 + (\rho+d\rho)*\vec{W} - \rho*\vec{V}$$

where

$$\vec{W} = (\ \mathrm{Cos}(\phi_0)\ ,\ \mathrm{Sin}(\phi_0)\ )$$

$$\vec{V} = (\ \mathrm{Cos}(\phi+\phi_0)\ ,\ \mathrm{Sin}(\phi+\phi_0)\ )$$

Neaglive Track

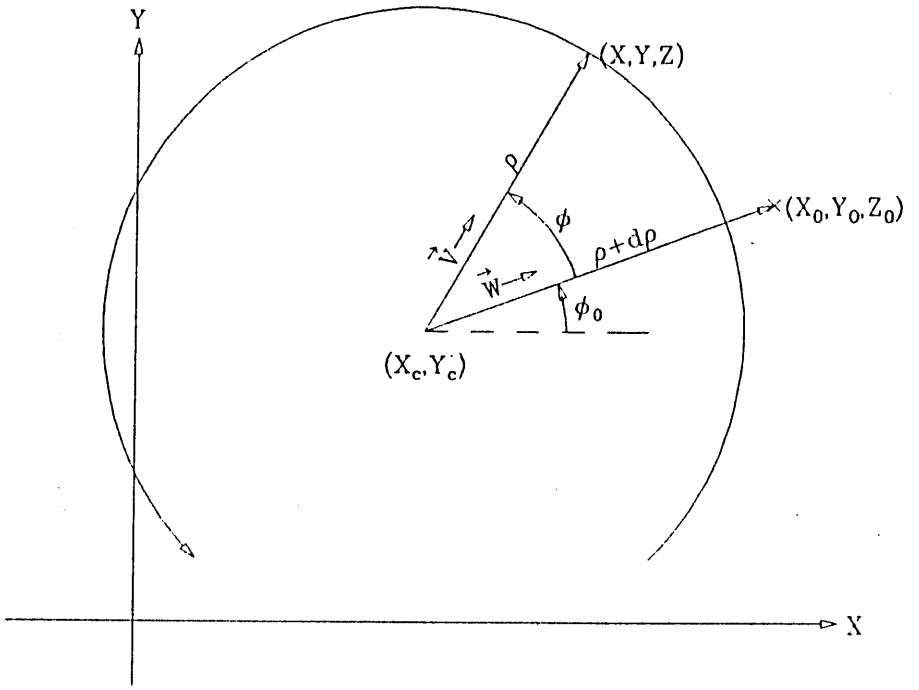

Fig.25

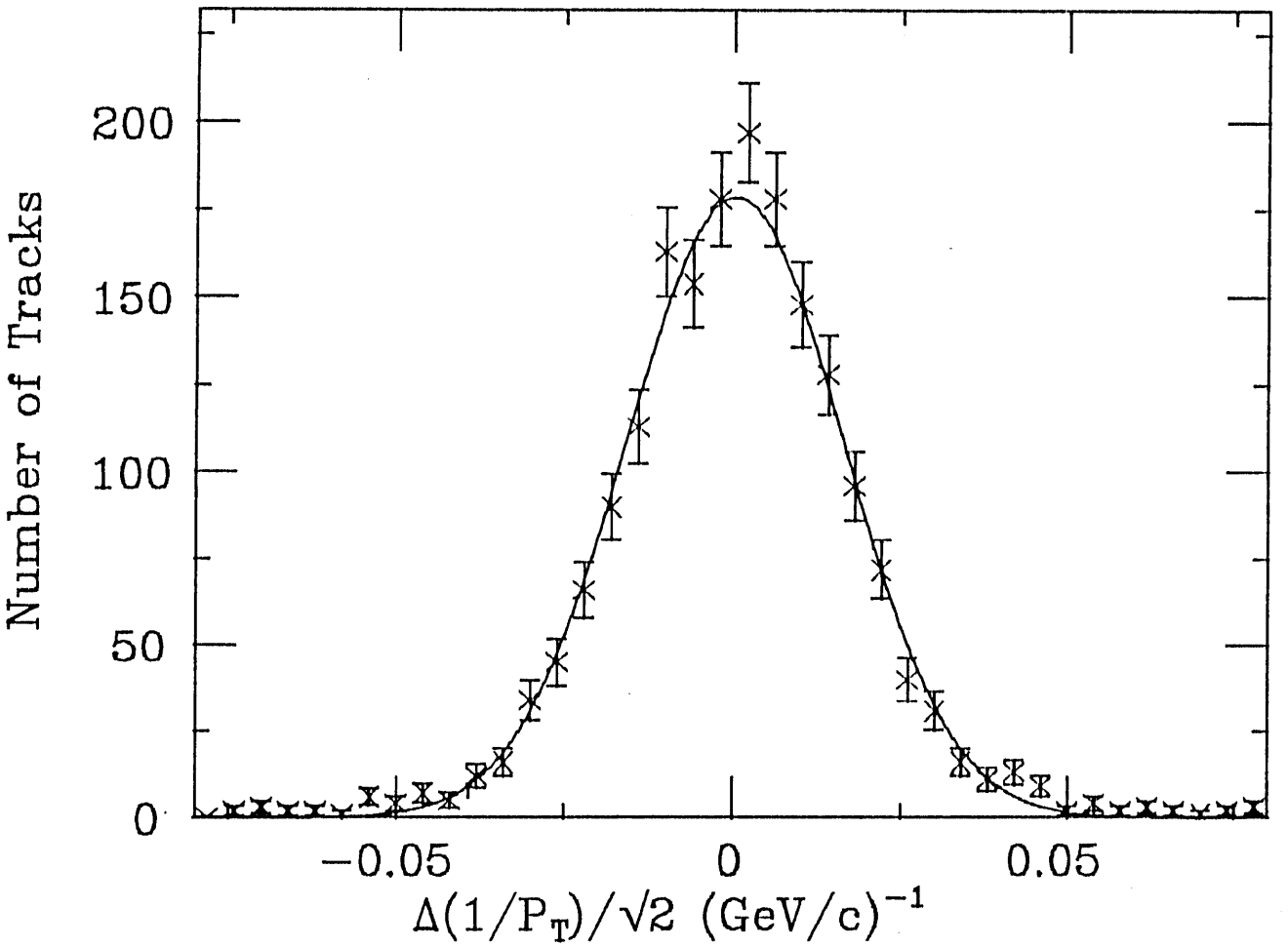

Fig.26

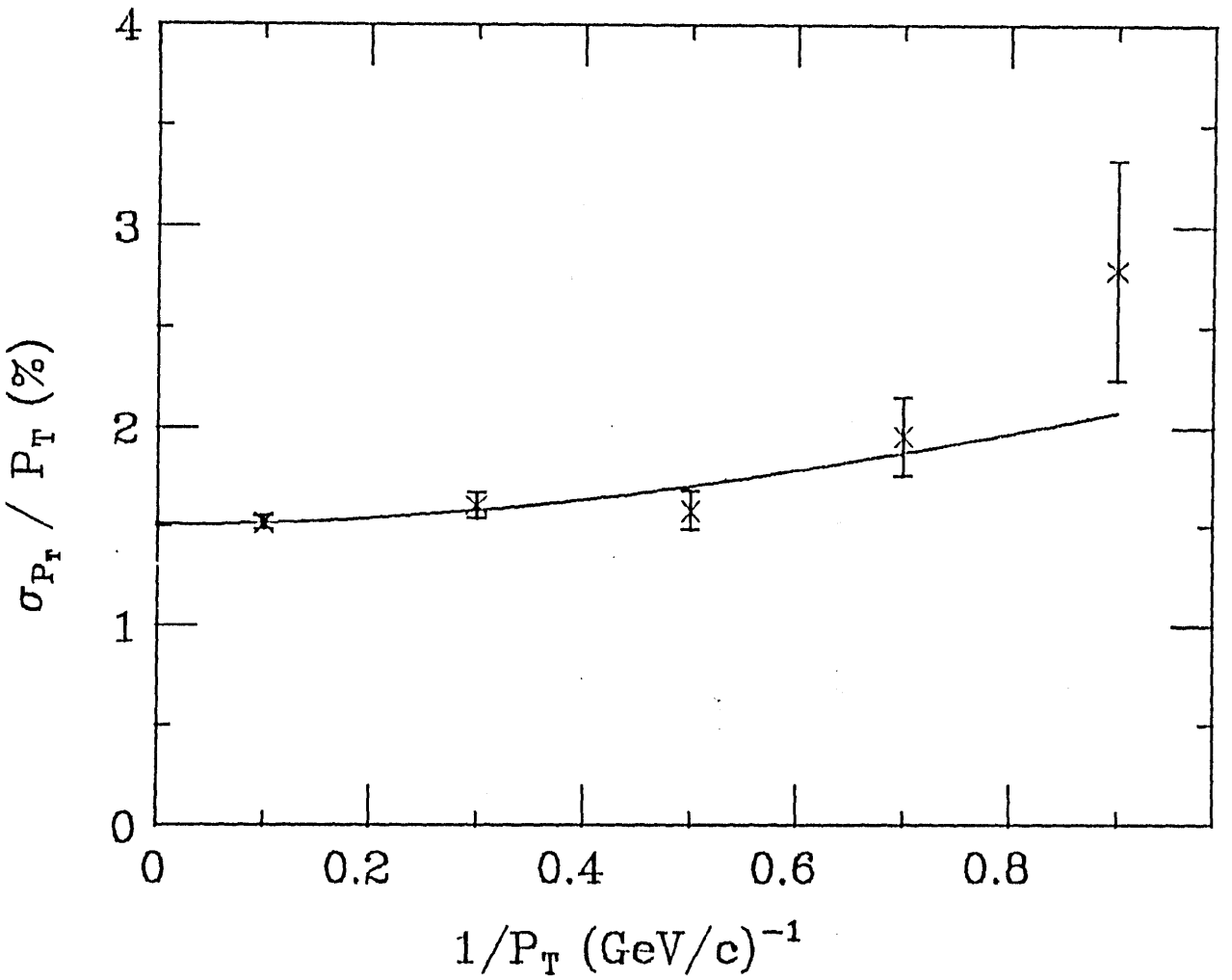

Fig.27

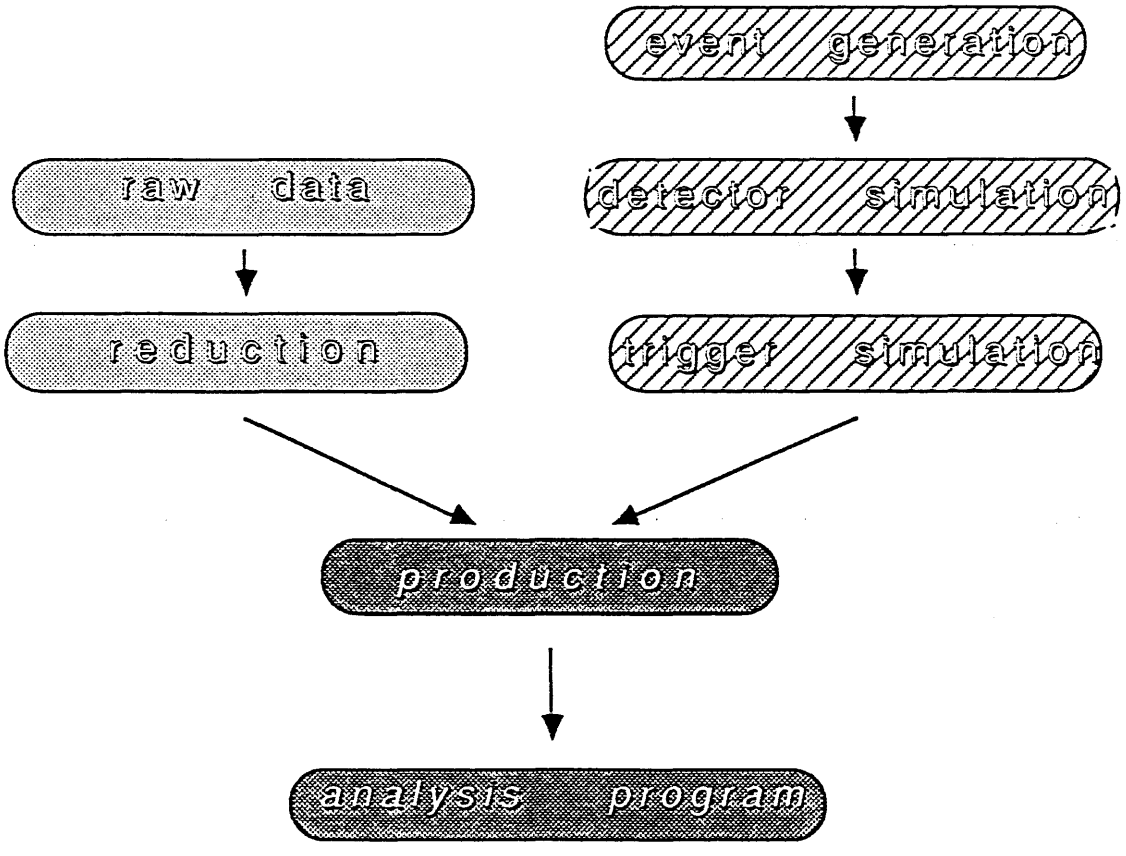
event generation
raw data
detector simulation
reduction
trigger simulation
production
analysis program

Fig.28

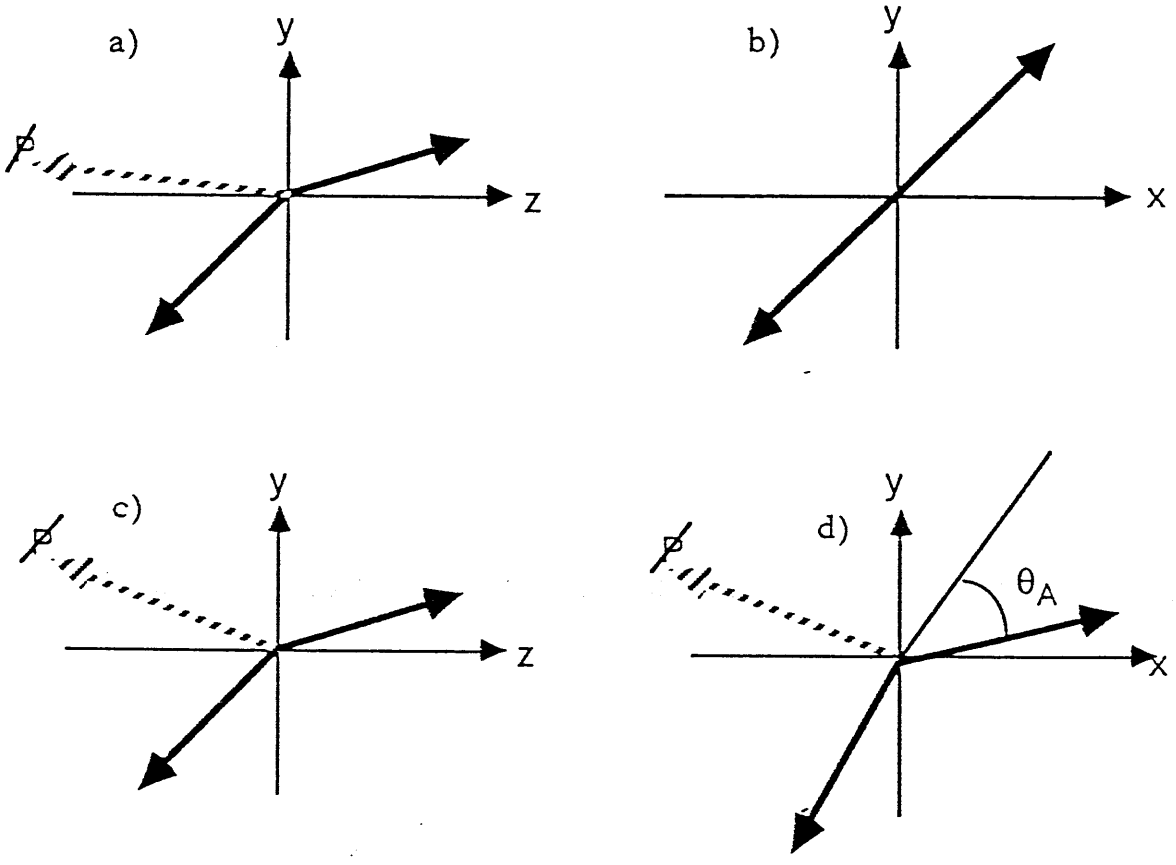

Fig.29

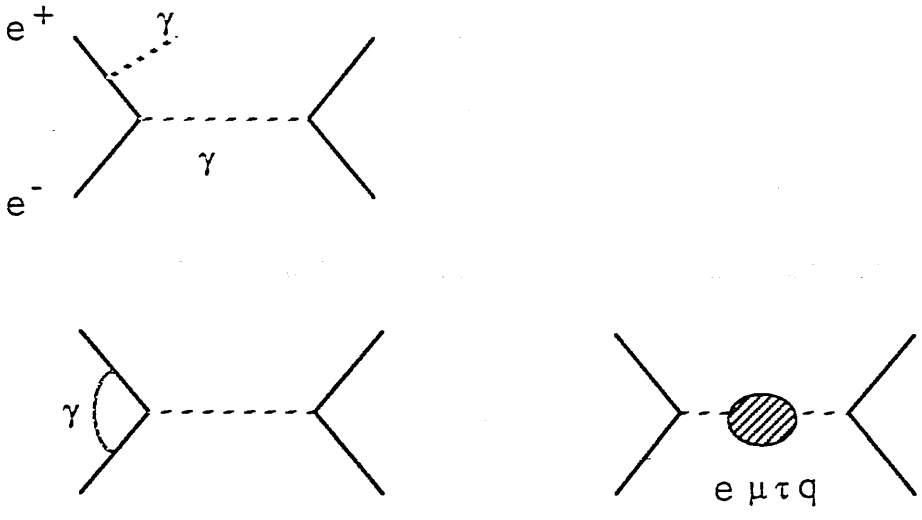

Fig.30

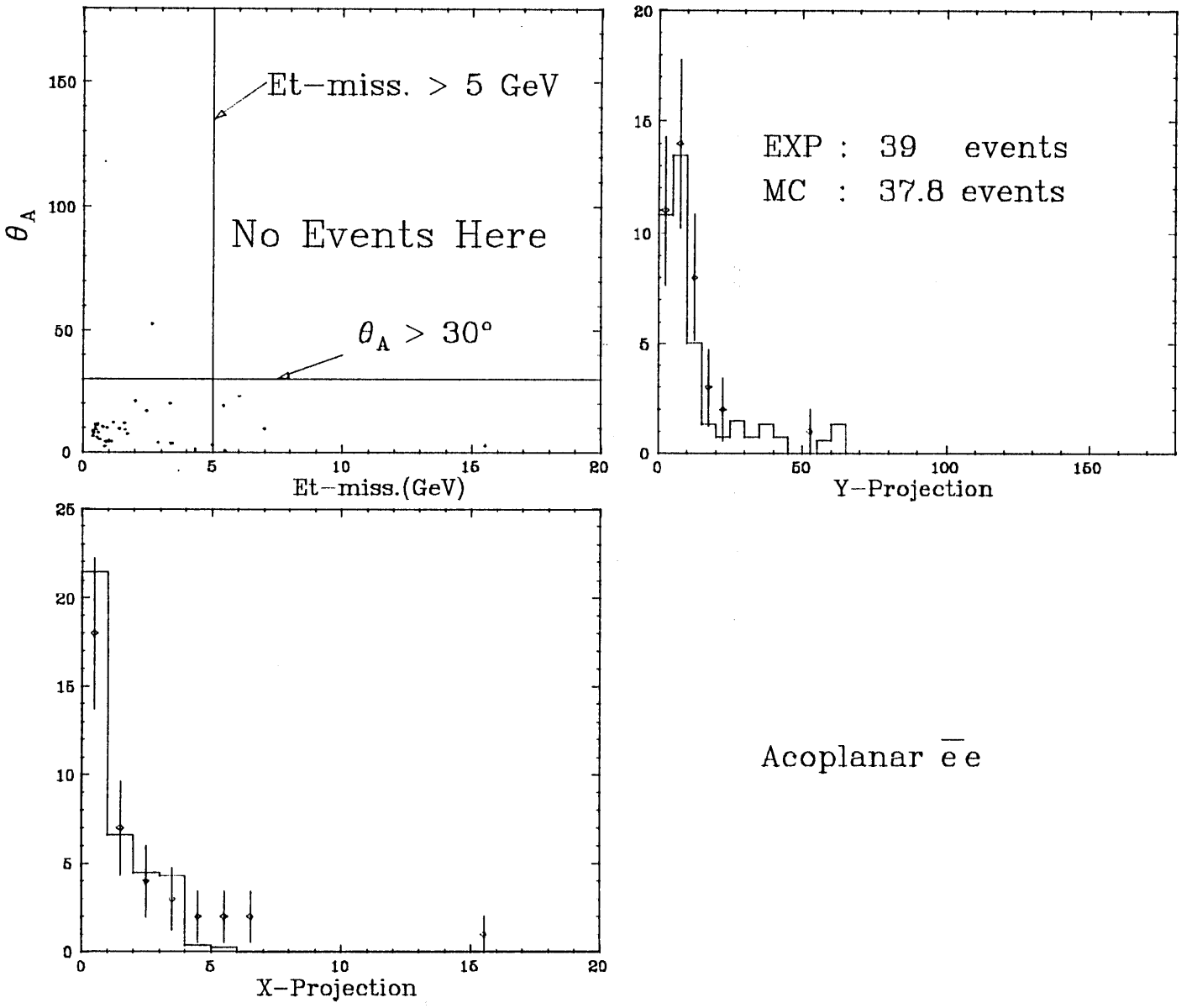
Et−miss. > 5 GeV
No Events Here
$\theta_A > 30°$
θ_A
Et−miss.(GeV)
EXP : 39 events
MC : 37.8 events
Y−Projection
X−Projection
Acoplanar $\bar{e}e$

Fig.31

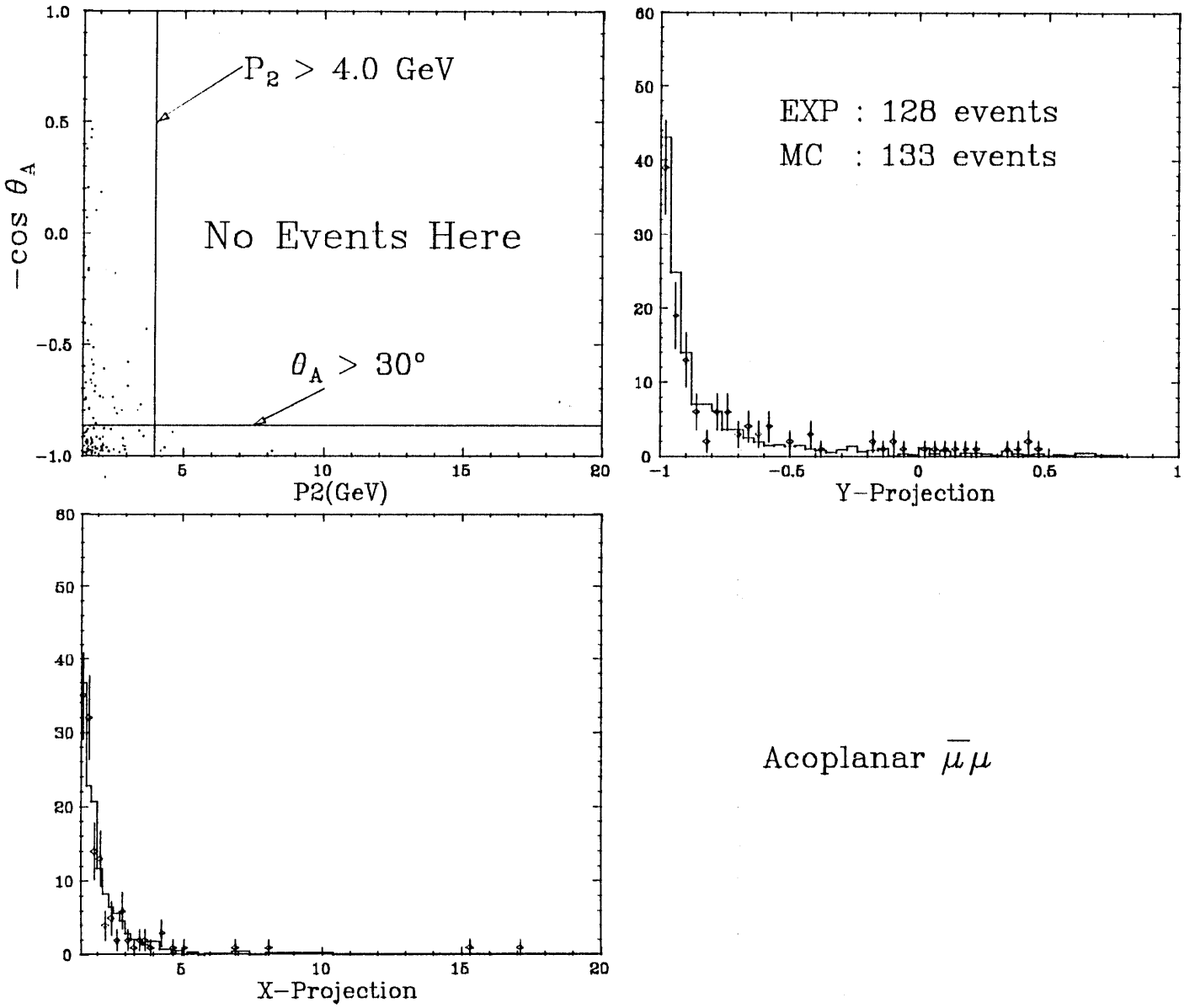

Acoplanar $\bar{\mu}\mu$

Fig.32

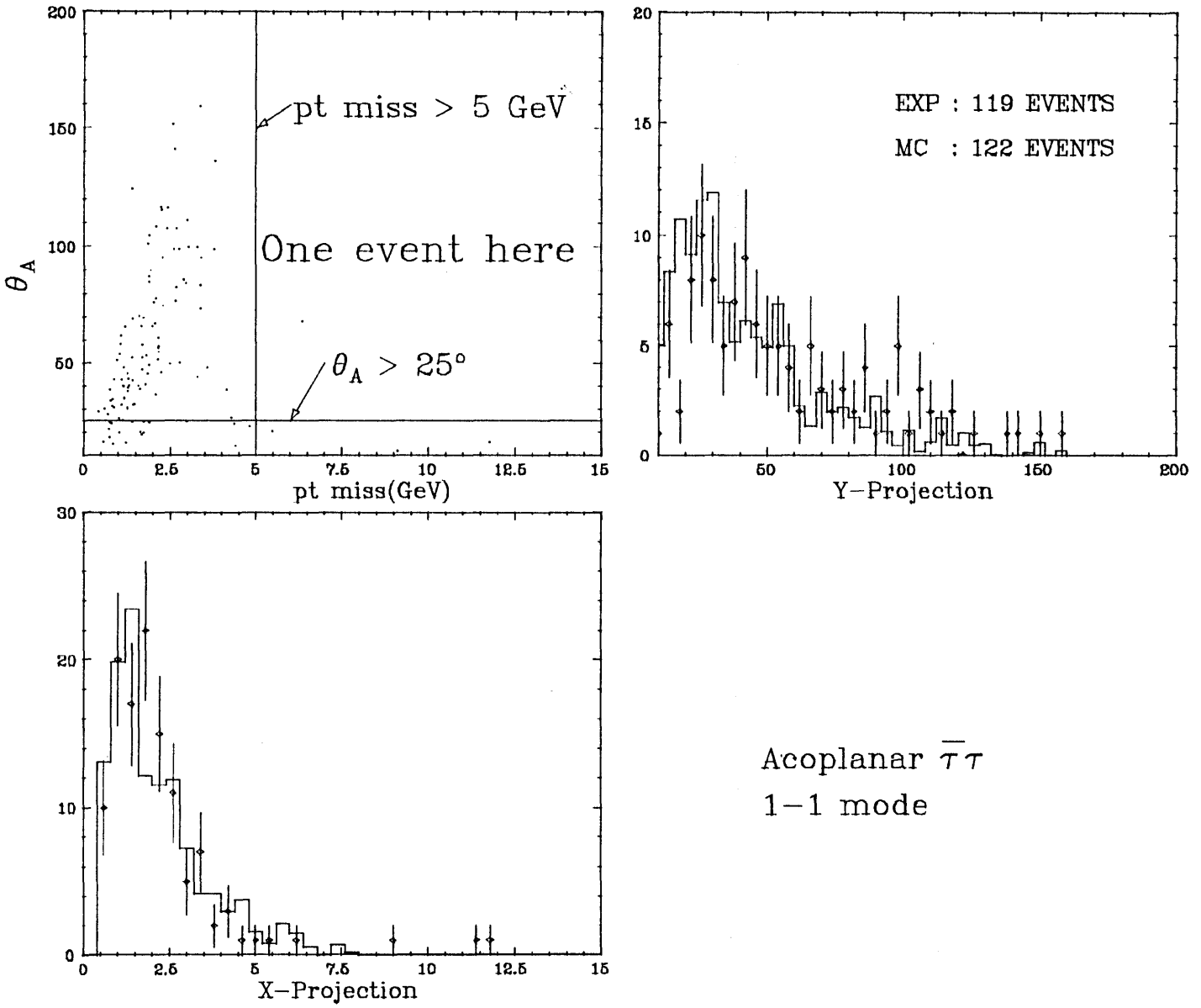

Acoplanar $\bar{\tau}\tau$
1−1 mode

Fig.33

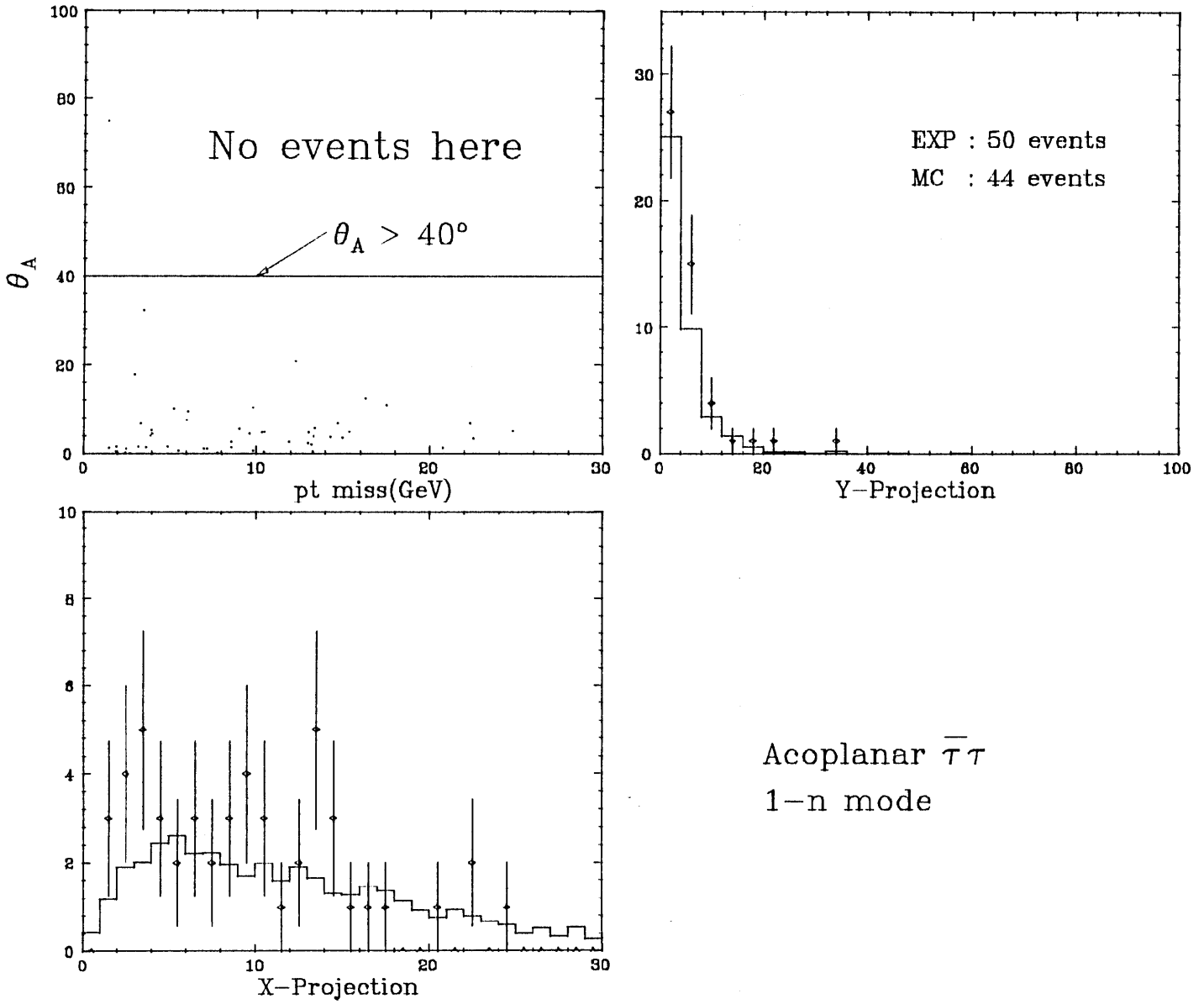

Acoplanar $\bar{\tau}\tau$
1−n mode

Fig.34

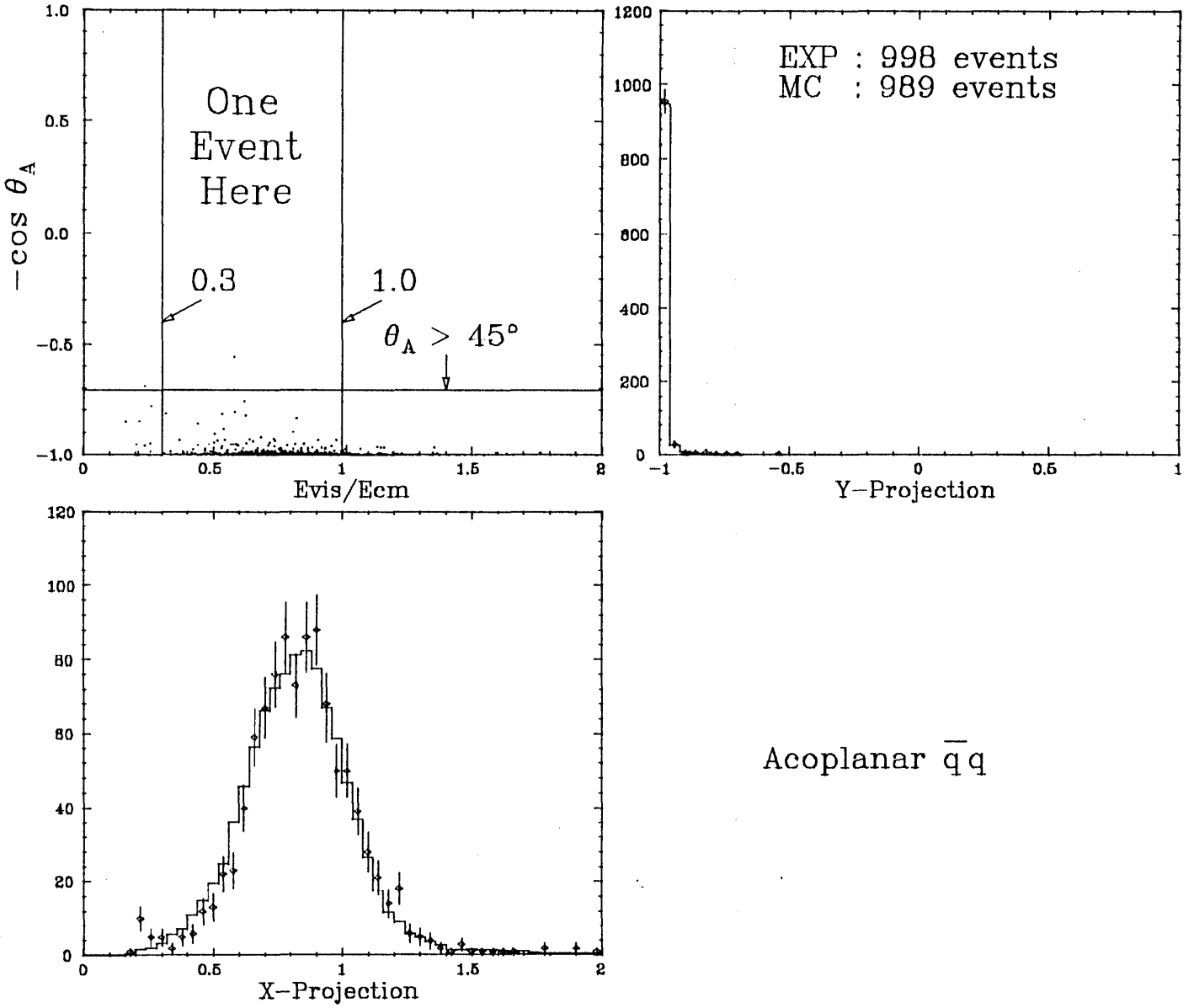

Acoplanar $\bar{q}q$

Fig.35

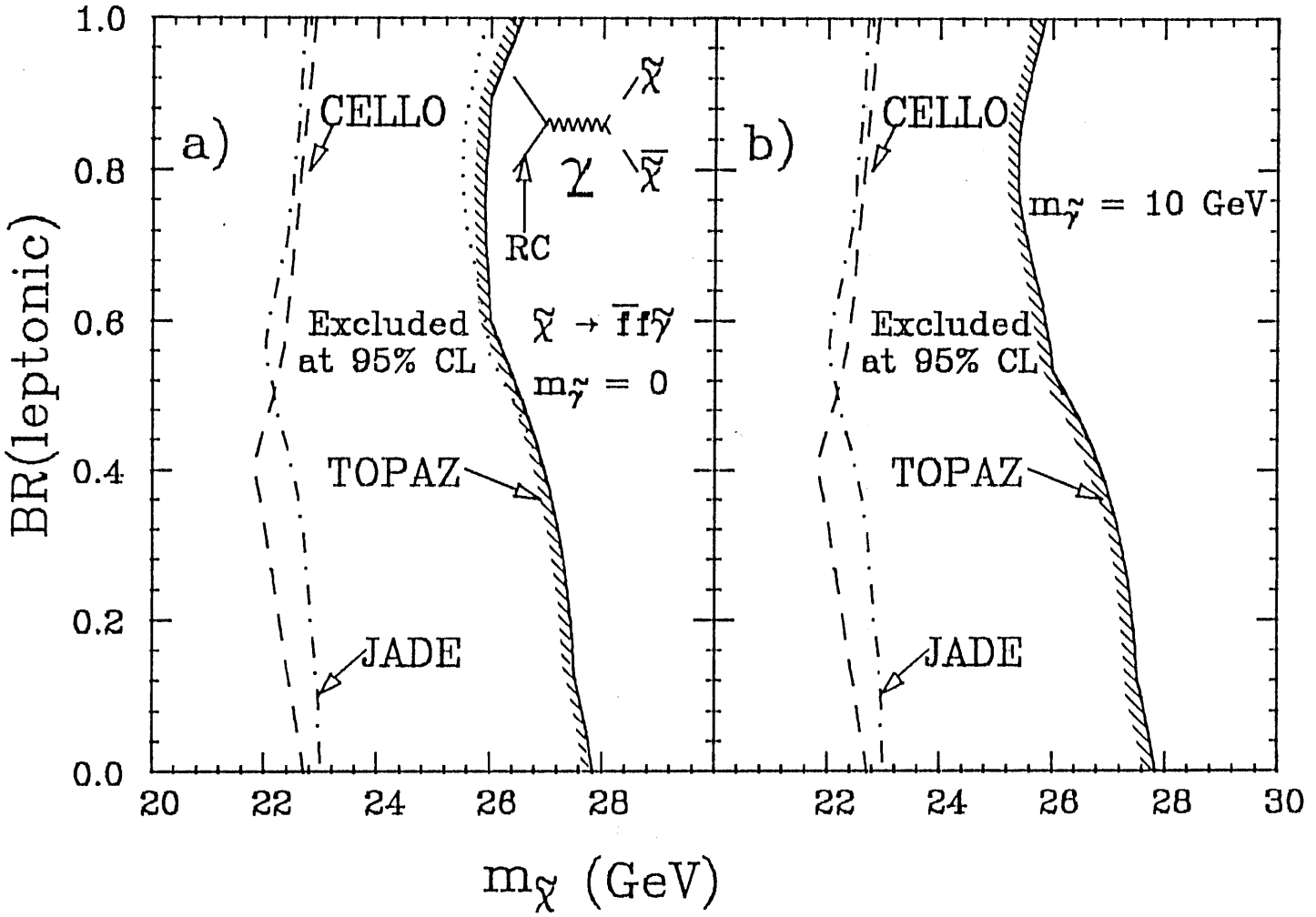
1.0
0.8
0.6
0.4
0.2
0.0
BR(leptonic)
a)
b)
CELLO
CELLO
RC
Excluded
at 95% CL
Excluded
at 95% CL
$\tilde{\chi} \to \bar{f} f \tilde{\gamma}$
$m_{\tilde{\gamma}} = 0$
$m_{\tilde{\gamma}} = 10$ GeV
TOPAZ
TOPAZ
JADE
JADE
20
22
24
26
28
22
24
26
28
30
$m_{\tilde{\chi}}$ (GeV)

Fig.36

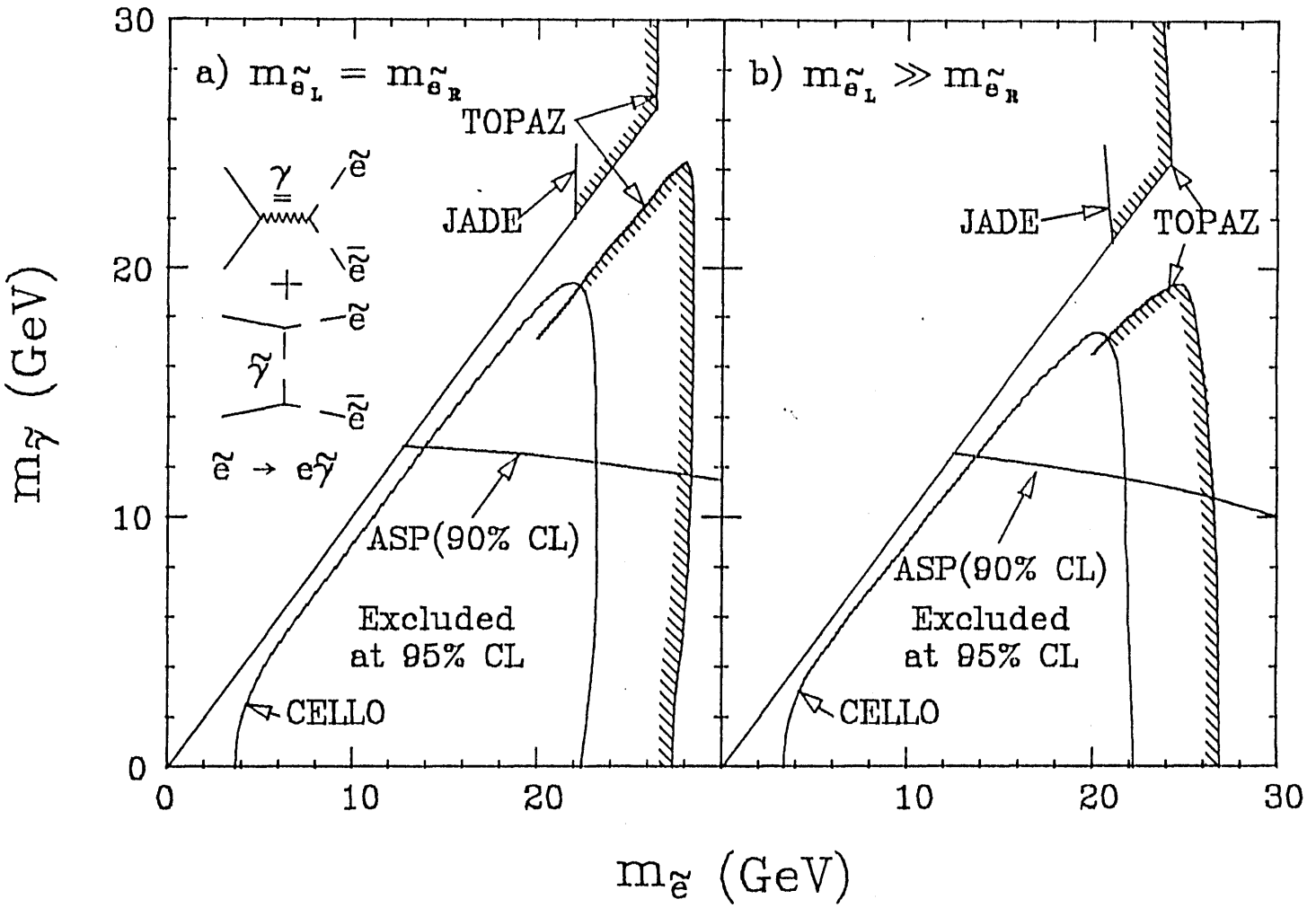
a) $m_{\tilde{e}_L} = m_{\tilde{e}_R}$
b) $m_{\tilde{e}_L} \gg m_{\tilde{e}_R}$
TOPAZ
JADE
ASP(90% CL)
Excluded
at 95% CL
CELLO
$\tilde{e} \to e\tilde{\gamma}$
$m_{\tilde{\gamma}}$ (GeV)
$m_{\tilde{e}}$ (GeV)
0
10
20
30

Fig.37

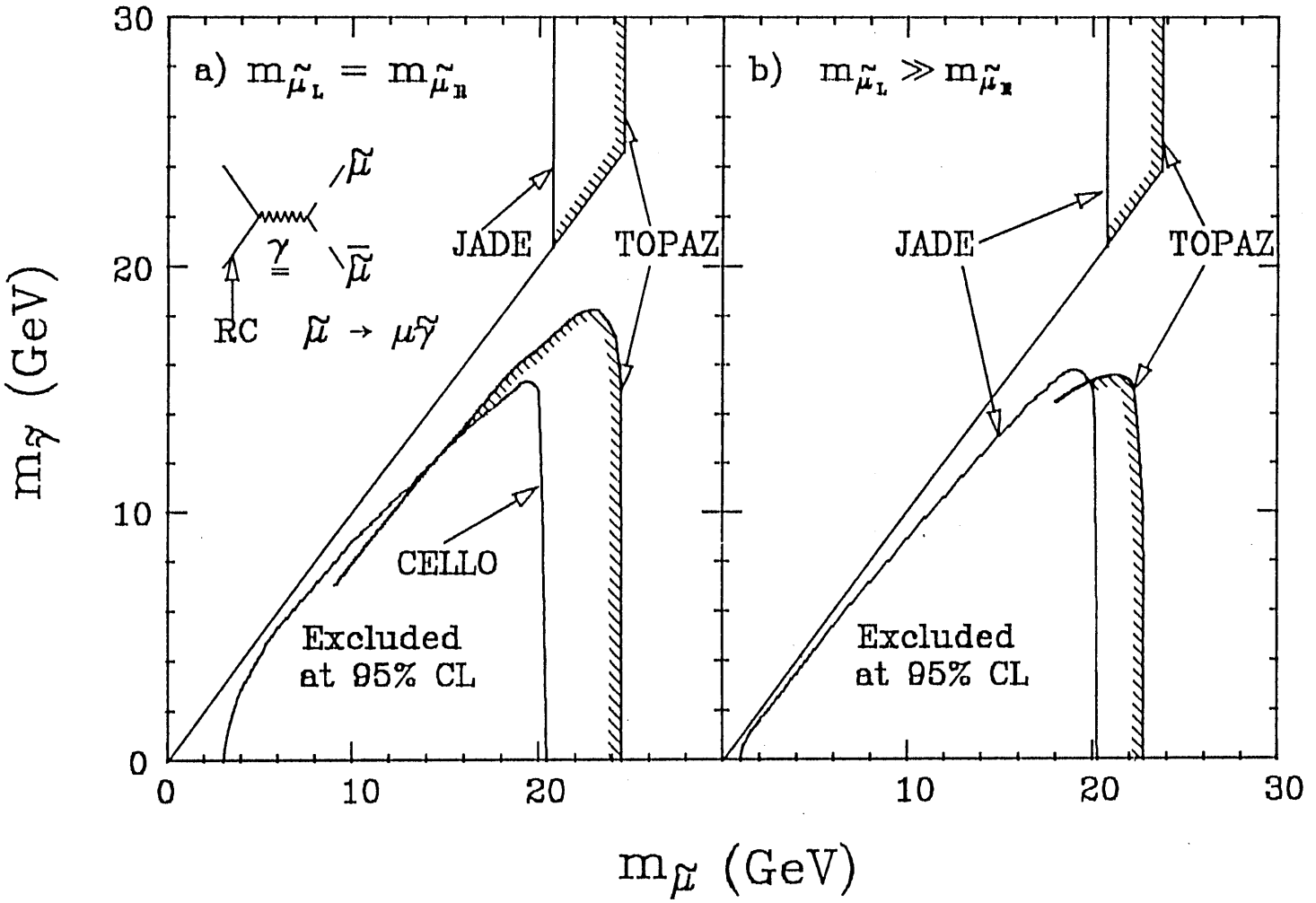
a) $m_{\tilde{\mu}_L} = m_{\tilde{\mu}_R}$
b) $m_{\tilde{\mu}_L} \gg m_{\tilde{\mu}_R}$
$\tilde{\mu}$
γ
$\bar{\tilde{\mu}}$
RC
$\tilde{\mu} \to \mu\tilde{\gamma}$
JADE
TOPAZ
CELLO
Excluded at 95% CL
$m_{\tilde{\gamma}}$ (GeV)
$m_{\tilde{\mu}}$ (GeV)
0
10
20
30

Fig.38

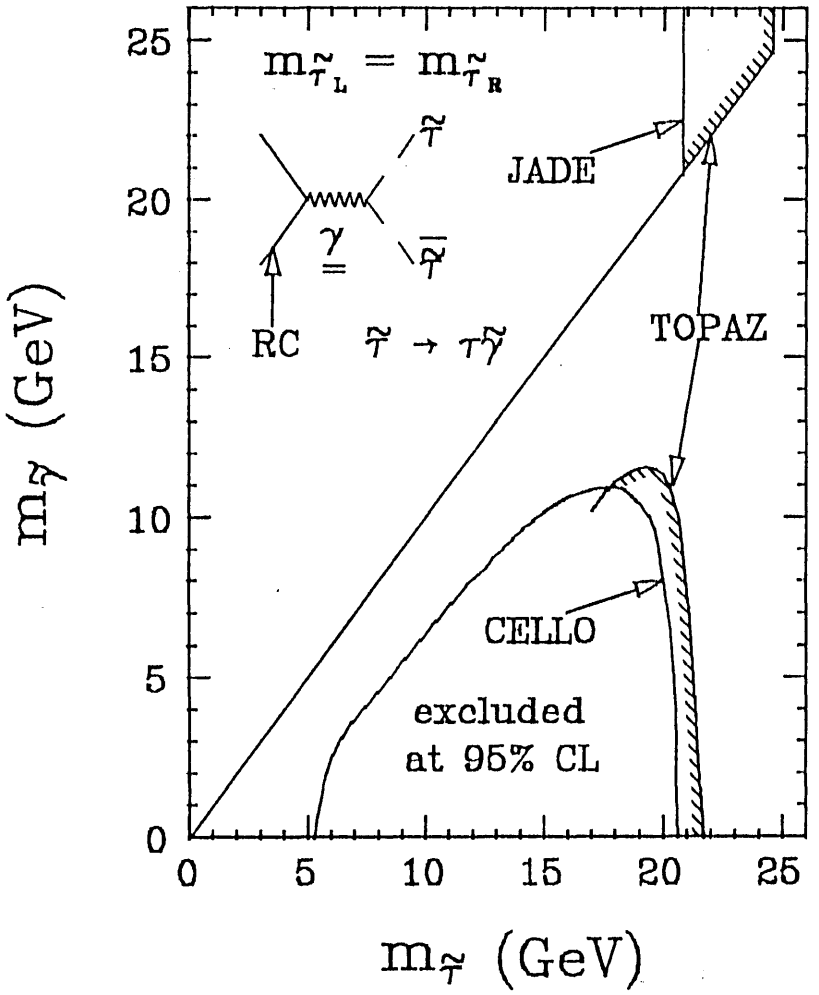
$m_{\tilde{\tau}_L} = m_{\tilde{\tau}_R}$
$\tilde{\tau}$
γ
$\bar{\tilde{\tau}}$
RC
$\tilde{\tau} \to \tau\tilde{\gamma}$
JADE
TOPAZ
CELLO
excluded
at 95% CL
$m_{\tilde{\gamma}}$ (GeV)
$m_{\tilde{\tau}}$ (GeV)
0
5
10
15
20
25

Fig.39

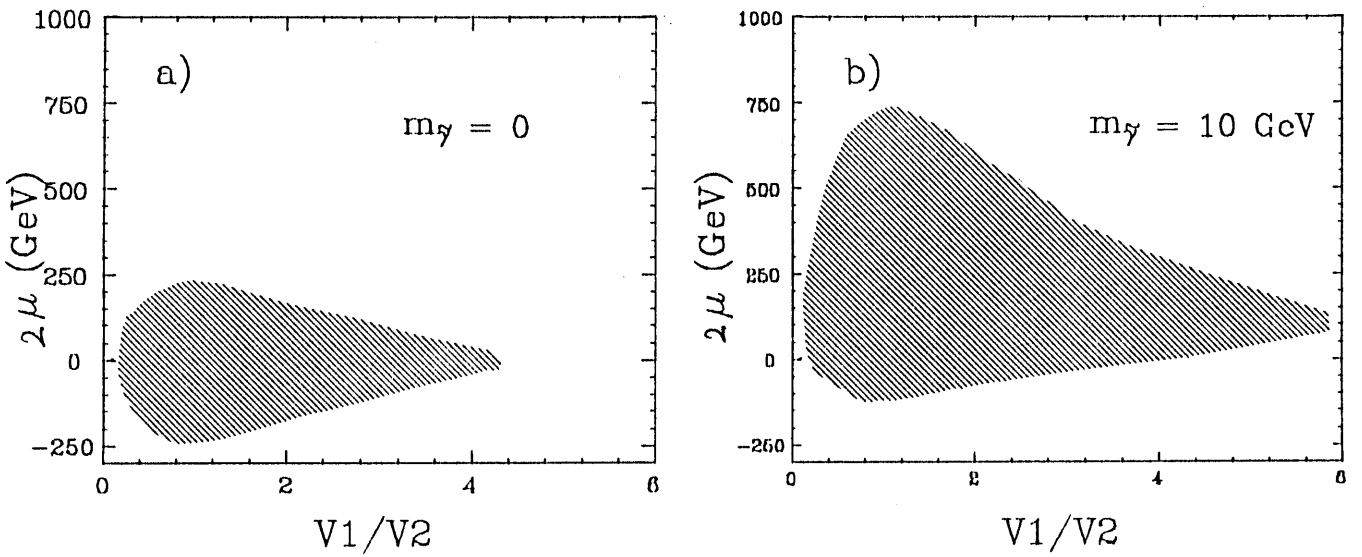
a)
$m_{\tilde{\gamma}} = 0$
b)
$m_{\tilde{\gamma}} = 10$ GeV
2μ (GeV)
V1/V2
1000
750
500
250
0
−250
0
2
4
6

Fig.40

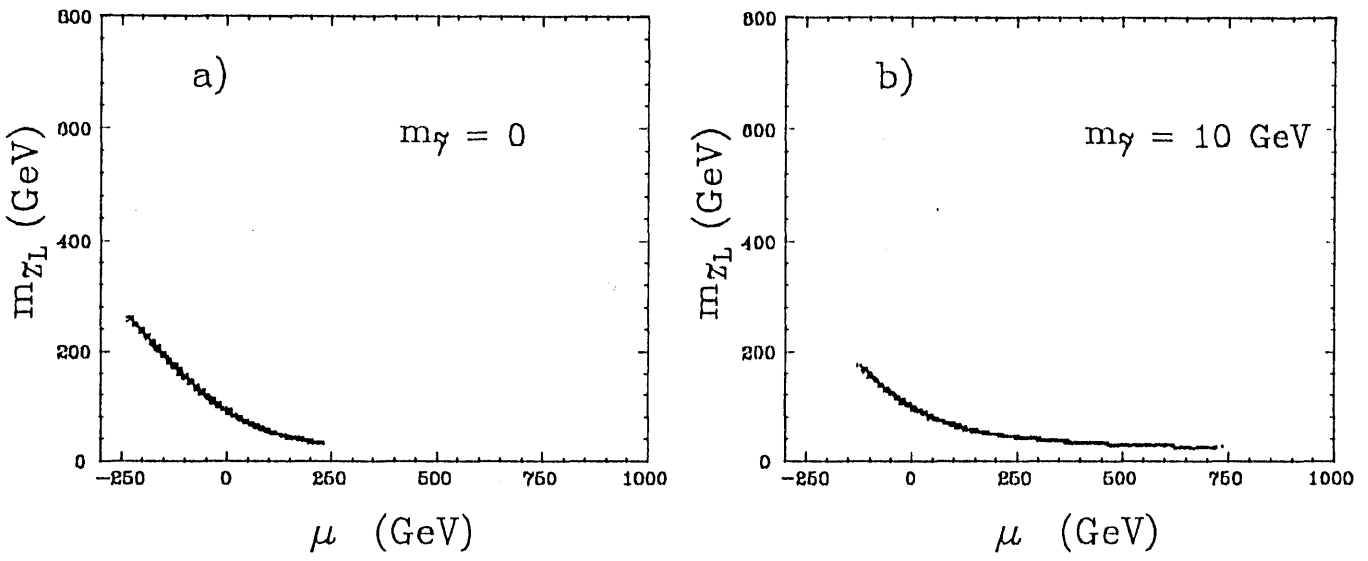
a)
$m_{\tilde{\gamma}} = 0$
$m_{\tilde{Z}_L}$ (GeV)
μ (GeV)
b)
$m_{\tilde{\gamma}} = 10$ GeV
$m_{\tilde{Z}_L}$ (GeV)
μ (GeV)

Fig.41

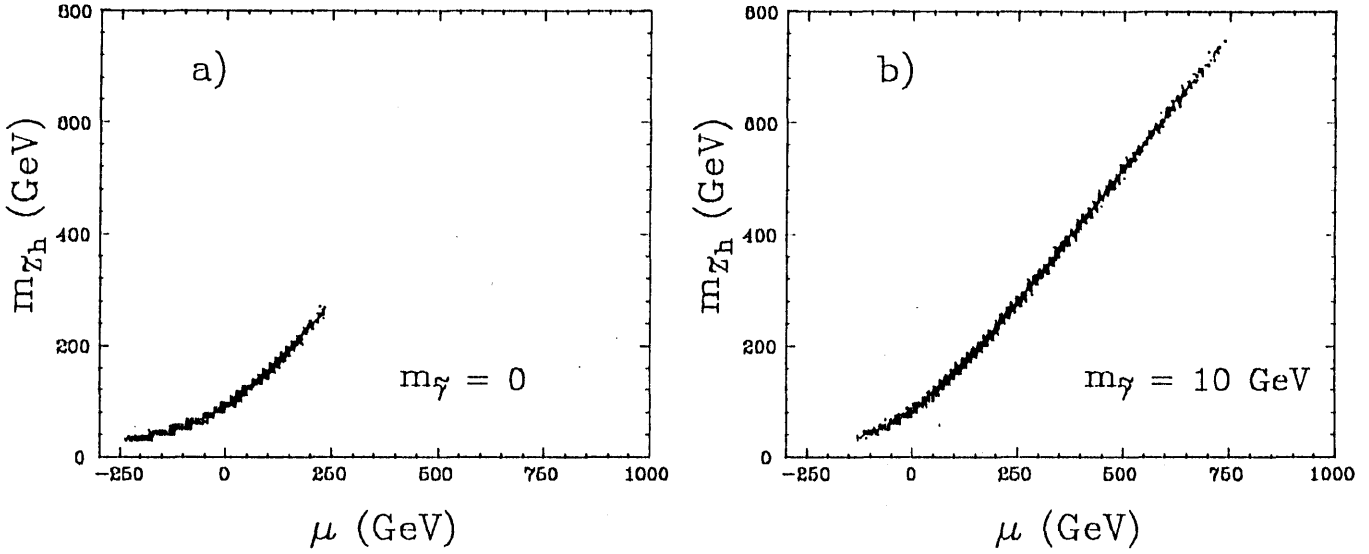
a)
b)
$m_{\tilde{\gamma}} = 0$
$m_{\tilde{\gamma}} = 10$ GeV
$m_{\tilde{\gamma}_h}$ (GeV)
μ (GeV)
0
200
400
600
800
−250
0
250
500
750
1000

Fig.42

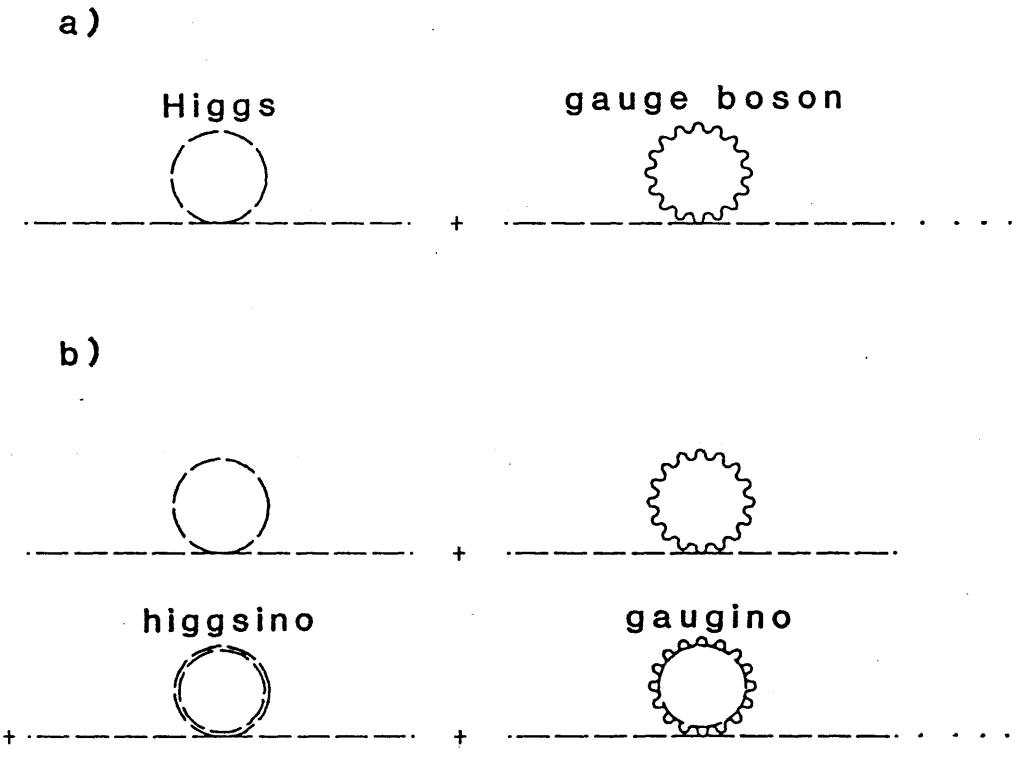

Fig.43

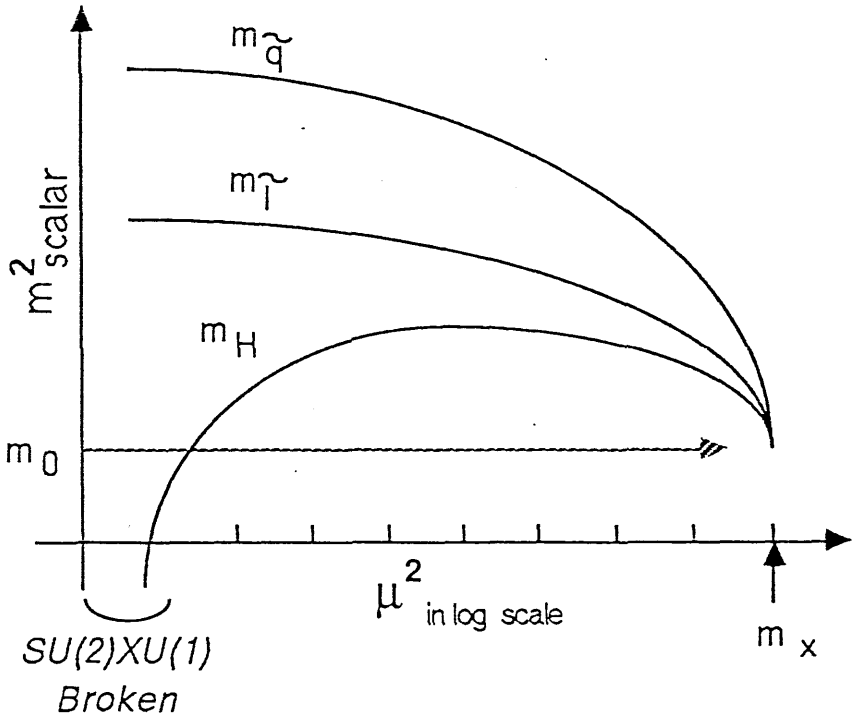
$m_{\tilde{q}}$
$m_{\tilde{l}}$
m^2_{scalar}
m_H
m_0
μ^2 in log scale
m_x
SU(2)XU(1)
Broken

Fig.44

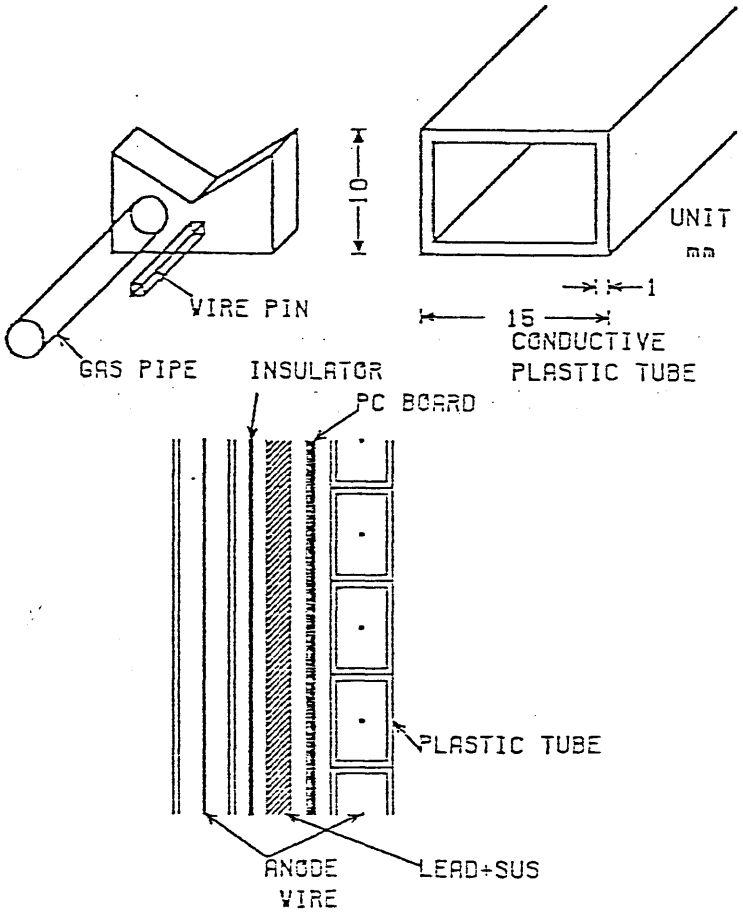
10
UNIT
mm
1
15
CONDUCTIVE
PLASTIC TUBE
VIRE PIN
GAS PIPE
INSULATOR
PC BOARD
PLASTIC TUBE
ANODE
VIRE
LEAD+SUS

Fig.45

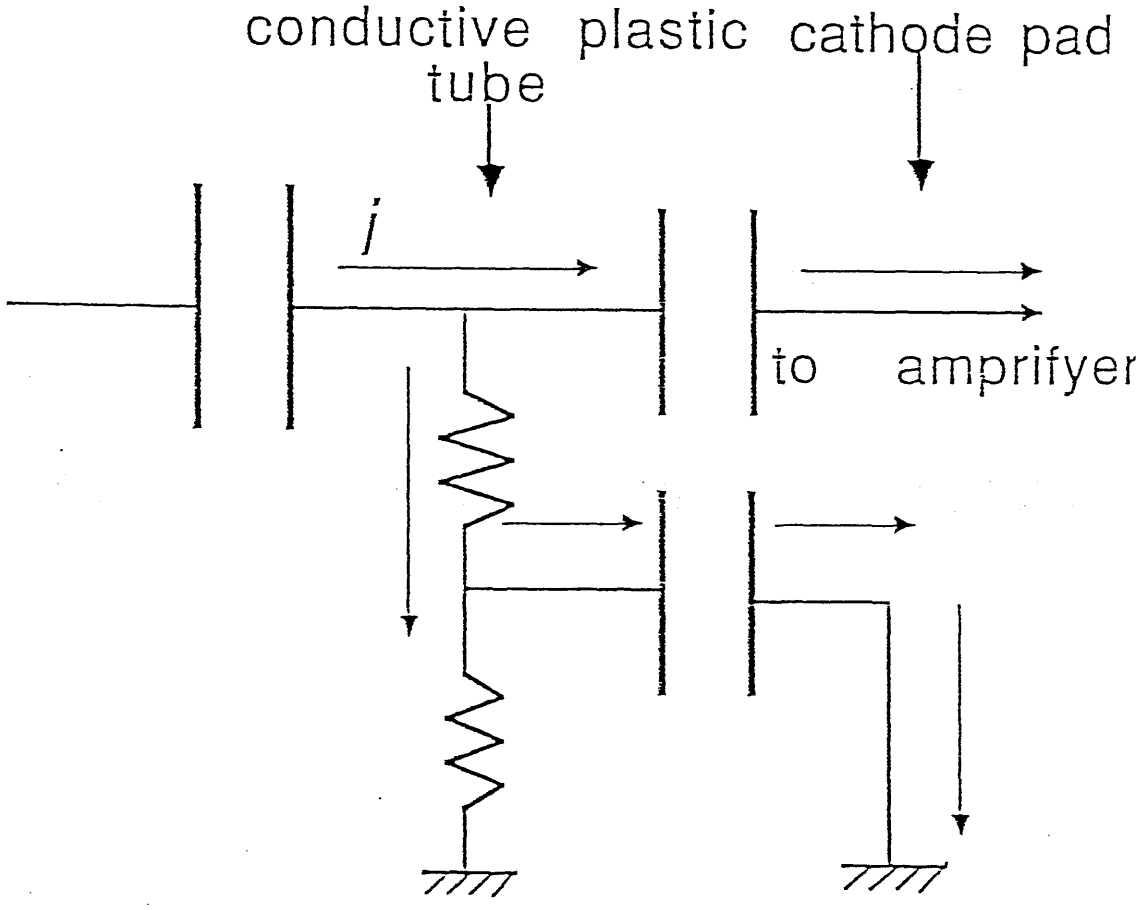

Fig.46

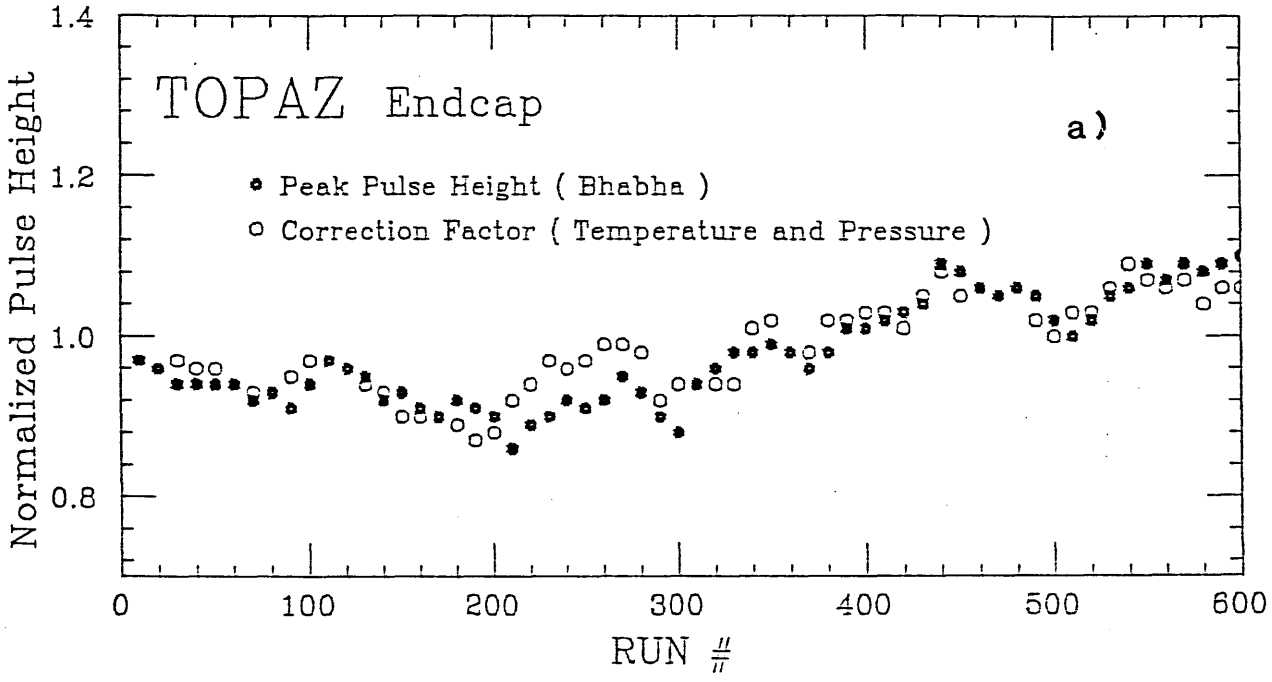
TOPAZ Endcap
a)
Peak Pulse Height (Bhabha)
Correction Factor (Temperature and Pressure)
Normalized Pulse Height
RUN #
1.4
1.2
1.0
0.8
0
100
200
300
400
500
600

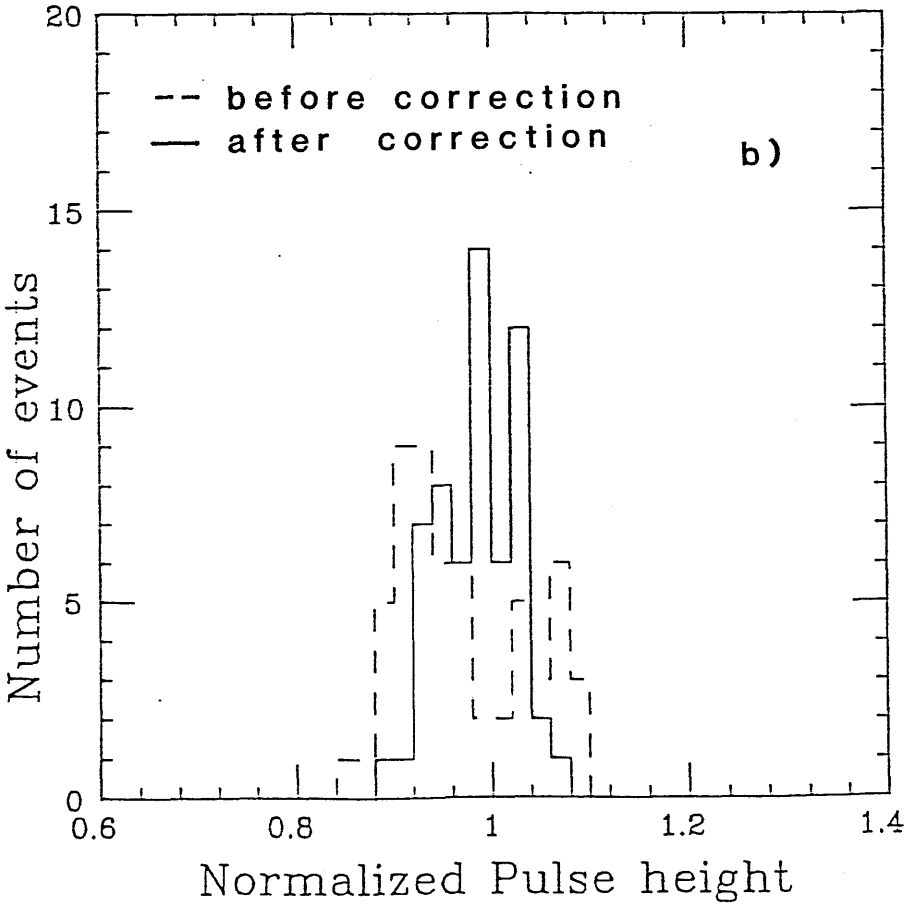
before correction
after correction
b)
Number of events
Normalized Pulse height
20
15
10
5
0
0.6
0.8
1
1.2
1.4

Fig.47